Characteristics of energetic motions in turbulent boundary layers

by

Dileep Chandran
ORCID ID : 0000-0003-1342-3785

Submitted in total fulfilment of the requirements
of the degree of Doctor of Philosophy

May 2019

Department of Mechanical Engineering

THE UNIVERSITY OF MELBOURNE

Declaration of Authorship

This is to certify that:

- the thesis comprises only my original work towards the PhD,
- due acknowledgement has been made in the text to all other material used,
- the thesis is fewer than 100,000 words in length, exclusive of tables, maps, bibliographies and appendices.

Signed:

Date: 08 May 2019

Abstract

In this dissertation, we present the first measurements of two-dimensional (2-D) energy spectra of the streamwise velocity component (u) in high Reynolds number turbulent boundary layers. The measurements in the logarithmic region of turbulent boundary layers give new evidence supporting the self-similarity arguments that are based on Townsend's (1976) attached eddy hypothesis. The 2-D spectrum is found to be able to isolate the range of self-similar scales from the broadband turbulence, which is not possible with the measurement of a 1-D energy spectrum alone.

High Reynolds number flows are characterized by large separation of scales. Therefore, to obtain converged 2-D statistics while resolving the broad spectrum of length and time scales, a novel experimental technique is required. To this end, we devise a technique employing multiple hot-wire probes to measure the 2-D energy spectra of u. Taylor's frozen turbulence hypothesis is used to convert temporal-spanwise information into a 2-D spatial spectrum which shows the contribution of streamwise (λ_x) and spanwise (λ_y) length scales to the streamwise variance at a given wall height (z). The validation of the measurement technique is performed at low Reynolds number by comparing against the direct numerical simulation (DNS) data of Sillero *et al.* (2014). Based on these comparisons, a correction is introduced to account for the spatial resolution associated with the initial separation of the hot-wires.

The proposed measurement technique is used to measure the 2-D spectra in the logarithmic region for friction Reynolds numbers ranging from 2400 to 26000. At low Reynolds numbers, the shape of the 2-D spectra at a constant energy level shows $\lambda_y/z \sim (\lambda_x/z)^{1/2}$ behaviour at large scales, which is in agreement with the existing literature. However, at high Reynolds numbers, it is observed that the square-root relationship tends towards a linear relationship ($\lambda_y \sim \lambda_x$) as required for self-similarity and predicted by the attached eddy hypothesis.

Finally, we present a model for the logarithmic region of turbulent boundary layers, which is based on the attached eddy framework and driven by the scaling of experimental 2-D spectra of u. The conventional attached eddy model (AEM), which comprises self-similar wall-attached eddies (*Type A*) alone, represent the large scale motions at high Reynolds numbers reasonably well. However, the scales that are not represented by the conventional AEM are observed to carry a significant proportion of the total kinetic energy. Therefore, in the present study we propose an extended AEM, where in addition to $Type\,A$ eddies, we also incorporate $Type\,C_A$ and $Type\,SS$ eddies. These represent the self-similar but wall-detached low-Reynolds number features and the non-self-similar wall-attached superstructures, respectively. The extended AEM is observed to predict a greater range of energetic length scales and capture the low- and high-Reynolds number scaling trends in the 2-D spectra of all three velocity components.

Acknowledgements

As with most PhDs, mine too was not a lone undertaking. Here, I would like to thank everyone who was by my side along the way.

I would like to extend my sincerest gratitude to Prof. Ivan Marusic and Prof. Jason Monty whose constant guidance and support charted the course for my PhD. Their expertise and enthusiasm towards fluid mechanics has helped build my perspective of this field. I would also like to thank my committee chair Prof. Nicholas Hutchins and my committee member Dr. Jimmy Philip for their valuable remarks and suggestions during my progress review meetings.

A special thanks goes towards Dr. Rio Baidya, who was a mentor during the initial years of my PhD, and a friend throughout. Discussions with Dr. Charitha deSilva, Dr. Woutijn Baars, Dr. Kevin and Dr. Milad Samie were both invaluable and a pleasure during my time here. And to all my friends in the fluids lab who made this journey just that little bit easier, I extend my warmest gratitude.

I would like to acknowledge the technical support from Mr William George Ross and Mr. Geoff Duke. I am indebted to Ms. Kim Robinson and Ms. Emma Mitchell for patiently proof-reading my work several times.

To celebrate the good times of my PhD and to mitigate the harsh ones, I am grateful that my friends were always by my side. I would like to thank my family for their constant belief in me, and especially my parents Mr. Venugopal Thalachallur and Mrs. Shailaja Venugopal, without whose unwavering support and encouragement this PhD would not have begun. To them I dedicate this thesis.

Finally, I would like to thank my PhD for introducing to me my partner, Anagha, and her, for supporting me through the PhD.

Contents

List of Figures

List of Tables

Nomenclature

Roman symbols

A	additive universal constant in the logarithmic law of the wall
A_1	universal constant in the logarithmic law for the streamwise turbulence intensity from the attached eddy hypothesis or the plateau in the 1-D energy spectra of u
A_{1x}, A_{1y}	A_1 from the streamwise and spanwise spectra of u
A_2	universal constant in the logarithmic law for the spanwise turbulence intensity from the attached eddy hypothesis
B_i	characteristic additive constant for the streamwise, spanwise and wall-normal turbulence intensities from the attached eddy hypothesis; $i = 1, 2, 3$
C_p	coefficient of pressure
d	diameter of a hot-wire sensor
$dy_{initial}$	initial spacing between the closest hot-wires
f_c	cut-off frequency
f_{max}	maximum frequency of the energetic scales in the boundary layer
f_s	sampling frequency
$\mathcal{F}$	Fourier transformation
G_{1x}, G_{2x}	small-scale and large-scale bounds of k_x^{-1} region
G_{1y}, G_{2y}	small-scale and large-scale bounds of k_y^{-1} region
h_o	separation of the eddy from the wall
$\mathcal{H}$	characteristic height of an eddy in the AEM
$\mathcal{H}_S$	height of the smallest eddy in the AEM
$\mathcal{H}_L$	height of the largest eddy in the AEM

j	unit imaginary number
k	wavenumber
K_0	universal Kolmogorov constant
k_x, k_y	streamwise and spanwise wavenumbers
l	length of a hot-wire sensor
$\mathcal{L}$	length of the representative eddy
L_x, L_y	streamwise and spanwise lengths of the domain
m	slope of the *large eddy region* in the 2-D spectrum or the ratio of the plateau in 1-D streamwise spetcrum to the plateau in 1-D spanwise spectrum
$\mathcal{N}$	number of hairpins in the representative eddy
n_x, n_y	number of streamwise and spanwise grid points
$\mathcal{P}$	probability density function
R_{uu}	two-point correlation function of u
Re	Reynolds number
Re_τ	Reynolds number based on friction velocity or Kármán number, $Re_\tau = U_\tau \delta/\nu$
T	sampling time
U	mean streamwise velocity
U_∞	freestream velocity
U_τ	mean friction velocity
u, v, w	streamwise, spanwise and wall-normal velocity fluctuations
v_η	Kolmogorov velocity scale
$\mathcal{W}$	width of the representative eddy
W_A, W_{CA}, W_{SS}	weightings of $Type\,A$, $Type\,C_A$ and $Type\,SS$ eddies
x, y, z	streamwise, spanwise and wall-normal directions
z_R	reference wall-normal location

Greek symbols

$\gamma_{L,2D}$	2-D linear coherence spectrum
δ	boundary layer thickness
δ_{99}	boundary layer thickness based on 99% of U_∞

δ_E	height of the largest eddy in the AEM
$\Delta x, \Delta y, \Delta z$	streamwise, spanwise and wall-normal spacings
Δx_p	spacing between the hairpins in a representative eddy
Δy_{max}	maximum spanwise spacing between the hot-wires
ϵ	turbulent energy dissipation
η	Kolmogorov length scale
κ	von Kármán constant in the logarithmic law of the wall
λ	wavelength
λ_x, λ_y	streamwise and spanwise wavelengths
ν	kinematic viscosity
ρ	density of fluid
τ_w	mean shear stress at the wall
Φ_{ij}	basis funciton in the AEM
$\phi_{uu}, \phi_{vv}, \phi_{ww}$	energy spectrum of u, v and w

Prefixes

$\mathcal{O}(\ldots)$	order of

Superscript

$*$	complex conjugate
$+$	indicates viscous scaling. Viscous length, time and velocity scales are given by $l^+ = (lU_\tau)/\nu$, $t^+ = (tU_\tau^2)/\nu$ and $u^+ = u/U_\tau$, respectively

Other symbols

$\overline{u}$	overbars denote time-averaged quantities
$\hat{u}$	coefficient of Fourier transformation of u

Abbreviations

1-D	one-dimensional
2-D	two-dimensional
AEM	attached eddy model
COMP	composite
DNS	direct numerical simulation
HRNBLWT	High Reynolds Number Boundary Layer Wind Tunnel

HW	hot-wire
LSM	large-scale motion
LCS	linear coherence spectrum
MUCTA	Melbourne University constant temperature anemometer
PIV	particle image velocimetry
VLSM	very-large-scale motion

Chapter 1

Introduction

Turbulent boundary layers are characterized by energy-containing motions or 'eddies' of varying length and time scales. A characteristic dimensionless parameter that is indicative of the extent of such separation of scales is the friction Reynolds number, defined as $Re_\tau = \delta/(\nu/U_\tau)$. Here, δ denotes the thickness of the boundary layer and ν/U_τ is the viscous length scale, where U_τ and ν are the friction velocity and kinematic viscosity, respectively. Therefore, Re_τ can be interpreted as the ratio of the largest to the smallest turbulent length scale in the flow. Consequently, high Reynolds number flows, that are often encountered in nature and many engineering applications, are characterized by a large separation of the energetic scales.

An important tool that is frequently used in turbulence research, to characterize the coexisting range of scales based on their energy content, is the power spectral density of velocity fluctuations, often known as the energy spectrum, ϕ_{uu}. The energy spectrum statistically describes the contribution to the total kinetic energy by the range of scales, from the viscosity- to the inertia-dominated subrange. In wall bounded flows, the spectrum is representative of the contributions from the dissipative scales, where the assumption of local isotropy is valid, to the large anisotropic structures, which includes the large organized or 'coherent' motions. In literature, almost all of the energy spectra discussed in high Reynolds number wall-bounded flow studies ($Re_\tau \sim \mathcal{O}(10^4)$) are one-dimensional, where the energy decomposition is based on streamwise wavenumbers (k_x) alone. However, in the present study, we measure the two-dimensional (2-D) energy spectra of u, as a function of both streamwise and spanwise (k_y) wavenumbers. The integration of the energy bounded by the 2-D spectrum of u, across the streamwise and spanwise length scales, is equal to the streamwise turbulence intensity ($\overline{u^2}$), i.e.,

$$\int\int \phi_{uu}(k_x, k_y)\mathrm{d}k_x\mathrm{d}k_y = \int \phi_{uu}(k_x)\mathrm{d}k_x = \int \phi_{uu}(k_y)\mathrm{d}k_y = \overline{u^2}.$$

1.1 Motivation

A number of models for the inertial (logarithmic) region of wall-turbulence rely on the assumption that the coherent and energy-containing motions (or eddies) are self-similar. This self-similarity requires that the geometric length and velocity of the turbulent structures scale with wall height (z) and friction velocity (U_τ) respectively. Townsend's (1976) attached eddy hypothesis is arguably the best known of these models and further assumes a random arrangement of the self-similar eddies that are attached to the wall and have a population density that is inversely proportional to their size. Townsend's conceptual model was extended by Perry & Chong (1982), who specified shapes for the eddies to make more detailed predictions. Further, on the basis of dimensional analysis, Perry & Chong (1982) predicted a k_x^{-1} scaling of the one-dimensional (1-D) streamwise spectra of u. The k_x^{-1} scaling, which later gained support through spectral overlap arguments of Perry *et al.* (1986) and is commonly assumed in atmospheric boundary layer research, suggests the existence of a range of length scales that contribute equally to the turbulent kinetic energy. However, an observation of this k_x^{-1} scaling of the 1-D streamwise spectra has remained elusive even in high Reynolds number experiments. While the lack of empirical support questions the existence of such a scaling, Davidson *et al.* (2006) suggests that the 1-D energy spectra are not the ideal tools to observe self-similarity. Their work showed that aliasing contaminates the 1-D streamwise spectra by artificially shifting the energy to lower wavenumbers, thereby distorting the spectrum and hiding the extent of the k_x^{-1} spectral scaling.

The aliasing problem arises because a 1-D spectrum is measured along a straight line and the wave number vectors inclined to the line of measurement could be misinterpreted as low wave number disturbances (Tennekes & Lumley, 1972). That is, a streamwise 1-D spectrum lacks directional information along the spanwise direction and is only the average energy contribution over the entire range of spanwise wavelengths, λ_y $(= 2\pi/k_y)$, for a particular streamwise wavelength, λ_x $(= 2\pi/k_x)$. Direct measurement of the 2-D spectrum, which is a function of both k_x and k_y, avoids the aliasing problem (in the homogeneous directions). However, analysis of the 2-D spectrum of wall-turbulence is rare. A dimensional consideration of the 2-D spectrum in the inertial region was made by Chung *et al.* (2015), who argued that in order to have a k_x^{-1} behaviour in the 1-D spectrum, a region of constant energy in the 2-D spectrum should be bounded by $\lambda_y/z \sim f_1(\lambda_x/z)$ and $\lambda_y/z \sim f_2(\lambda_x/z)$ where f_1 and f_2 are identical power laws. Further, del Álamo *et al.* (2004) examined the 2-D spectra from direct numerical simulations (DNS) of a channel flow at $Re_\tau \leq 1900$ and showed empirically that such a region of constant energy is bounded at larger scales by a square-root relationship of the form $\lambda_y/z \sim (\lambda_x/z)^{1/2}$. This square-root relation between the lengths and widths of the structures indicates a failure of self-similarity. According to the attached eddy hypothesis of Townsend (1976), the geometrically self-similar scales should follow a linear relationship $\lambda_y \sim \lambda_x$. However, it is noted that Townsend's arguments are only expected to strictly hold at high Reynolds number (Marusic & Monty, 2019). Therefore, to validate the assumption of self-similar eddies in the attached eddy model, measurements of 2-D spectra at high Reynolds numbers are required.

1.2 Objectives and outline of thesis

The objectives of the present study are:

(*i*) To develop an experimental technique to measure the 2-D energy spectra of u at high Reynolds numbers and to validate the measurement scheme with the available high fidelity DNS data at low Reynolds numbers.

(*ii*) To measure the 2-D energy spectra of u in the logarithmic region of turbulent boundary layers at high Reynolds numbers and examine any evidence for, or against, the self-similarity arguments that is the basis for the attached eddy hypothesis of Townsend (1976). Additionally, to investigate the scaling of the 2-D energy spectra and hence characterize the Reynolds number trends of different scales.

(*iii*) To investigate whether the attached eddy model of Perry & Chong (1982), which is based on Townsend's (1976) attached eddy hypothesis, can be formulated to compute the 2-D energy spectra of all three velocity components and predict their empirically observed trends in the logarithmic region. Further, based on the 2-D energy spectra, we examine if the attached eddy model can be extended to include a greater range of length scales, and consequently, to improve its accuracy at low Reynolds numbers.

The outline of the thesis is as follows: Chapter 2 provides a brief review of the studies relevant to the goals of the thesis, with an emphasis on Townsend's (1976) attached eddy hypothesis and the associated scaling arguments. Chapter 3 describes the experimental facilities and the measurement technique involving hot-wire anemometry. Chapter 4 addresses objective (*i*), where, the calculation of 2-D energy spectra from the time series of u acquired synchronously with multiple hot-wire probes is detailed. This Chapter also discusses a correction scheme based on DNS, in order to improve the small-scale resolution of the 2-D energy spectra. Chapter 5 addresses objective (*ii*) and presents the first measurements of the 2-D energy spectra in high Reynolds number turbulent boundary layers. Chapter 6 addresses objective (*iii*) and focuses on the modelling of the logarithmic region in turbulent boundary layers based on the attached eddy framework. The development of the model is driven by the observed scaling of the experimental 2-D spectra of u. The thesis concludes with a summary of the key contributions from the present study along with suggestions for possible extensions to the current work.

It is noted that throughout this thesis, superscript '+' indicates the normalization using viscous length and velocity scales, which are ν/U_τ and U_τ, respectively. The streamwise, spanwise and wall-normal directions are denoted by x, y and z respectively, and u, v and w denote the streamwise, spanwise and wall-normal fluctuating velocity components, respectively.

Chapter 2

Literature review

This literature review provides a brief overview of the studies relevant to the goals of the thesis (§1.2), with an emphasis on Townsend's (1976) attached eddy hypothesis and the associated scaling arguments. This review is not intended to be exhaustive but to provide sufficient foundation for the discussions in the thesis.

2.1 Logarithmic region in turbulent boundary layers

In wall-bounded flows, based on classical scaling arguments, the turbulent boundary layer anatomy comprises various layers (or regions) that are characterized by their distance from the wall. An overview of these layers is provided in figure 2.1. Based on the appropriate length scales, the boundary layer is thus classified into the 'inner layer' and the 'outer layer' (von Kármán, 1930, Prandtl, 1904, 1925). In the inner layer, dimensional analysis revealed that the turbulence statistics scale with the friction velocity ($U_\tau = \sqrt{\tau_w/\rho}$) and the viscous length scale (ν/U_τ). Here, τ_w is the mean shear stress at the wall, ρ is the density of the fluid and ν is the kinematic viscosity of the fluid. In the outer layer far from the wall, the characteristic length scale is the thickness of the boundary layer (δ) while the characteristic velocity scale remains the same (U_τ). In pipe and channel flows, the characteristic

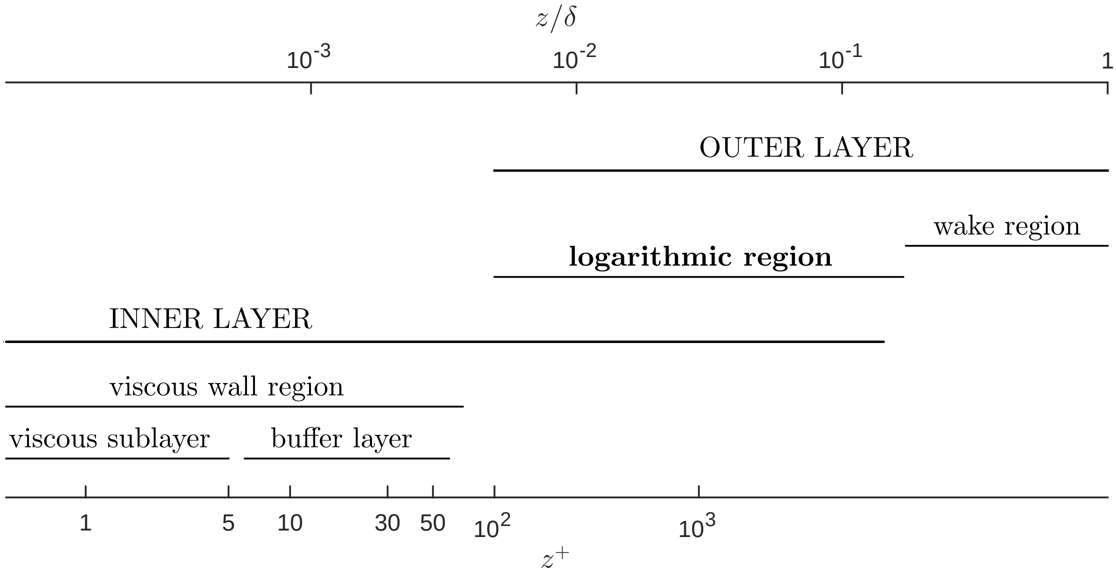

FIGURE 2.1: Depiction of the various wall layers within the turbulent boundary layer. Adapted from Pope (2000).

outer layer length scales are the pipe radius and the channel half-height, respectively. The friction Reynolds number is the ratio of these characteristic length scales in the outer and inner layers respectively, i.e., $Re_\tau = \delta^+ = \delta/(\nu/U_\tau)$. Millikan (1938) proposed the existence of an overlap region between the inner and outer layers, where the profile of the mean velocity (U) can be scaled by either the inner ($U^+ = f(z^+)$) or the outer ($U^+_\infty - U^+ = F(z/\delta)$) variables. Here, U_∞ is the freestream velocity. From this, it was deduced that the mean velocity follows a logarithmic variation (and hence the name 'logarithmic region' for the overlap region, also known as the inertial region) with the distance from the wall as

$$U^+ = \frac{1}{\kappa}\log(z^+) + A. \tag{2.1}$$

Here, κ is the von Kármán constant and A is a parameter dependent on the details of the wall and is a constant for smooth-walled flows. Apart from Millikan's overlap arguments, the logarithmic law has been derived using alternative approaches, which includes the mixing length hypothesis of Prandtl (1925) and formulations based on first principle consideration of the mean momentum equation (Fife *et al.*, 2005, Klewicki *et al.*, 2009, Oberlack, 2001).

At high Reynolds numbers, the logarithmic region is arguably the most important region within the boundary layer, containing a multitude of energetic scales. Although the local production of turbulence is highest close to the wall at $z^+ \approx 12$, at high Reynolds numbers, the bulk production of turbulent kinetic energy takes place within the logarithmic region (Marusic *et al.*, 2010*a*) In the asymptotic limit, the whole of the turbulence production and all of the velocity drop within the boundary layer, is inside the logarithmic region (Jiménez, 2012).

The much contested idea of the universality of the logarithmic region (see reviews by Jiménez, 2012, Klewicki, 2010, Marusic *et al.*, 2010*c*, Smits *et al.*, 2011), is supported by Marusic *et al.* (2013), using high Reynolds number data at $2 \times 10^4 < Re_\tau < 6 \times 10^5$. Many of the controversies associated with the universality of the logarithmic region originate from the inability to measure the wall shear stress accurately. Additionally, the difficulty in discerning the exact bounds of the logarithmic region leads to inconsistencies in estimating the value of κ. While it is agreed that the outer bound of the logarithmic region is a fixed fraction of boundary layer thickness ($0.15\,\delta$ was chosen by Marusic *et al.*, 2013 for the purposes of curve fitting), the beginning of the logarithmic region is disputed owing to the gradual deviation of U^+ from equation 2.1. Even though classical descriptions require the logarithmic region to start at a constant z^+, so far studies have not converged on a constant value, with the estimates from literature varying from $z^+ = 30$ (Tennekes & Lumley, 1972) to $z^+ = 600$ (Zagarola & Smits, 1998). Refer to Örlü *et al.* (2010) for a summary of the bounds of the logarithmic region as reported by various studies. More recently, based on Townsend's (1976) attached eddy hypothesis, Marusic *et al.* (2013) argued that the inertial region should be identified based on the logarithmic law in the profiles of both the mean velocity U^+ and the streamwise turbulence intensity $\overline{u^2}^+$. Using this argument, the authors showed that the estimate of $z^+ = 2.6 Re_\tau^{1/2}$ for the beginning of the logarithmic region, as proposed by Klewicki *et al.* (2009), is reasonable for the high Reynolds number range that they considered.

2.1.1 Structures in the logarithmic region

Similarity arguments based on the flow statistics reflect the physical structure of turbulence. Over the past years, numerous flow visualization and numerical studies have revealed the existence of organized or 'coherent' motions that play a crucial role in wall-bounded flows. Robinson (1991) defines a coherent motion as "a three-dimensional region of the flow over which at least one fundamental flow variable (velocity component, density, temperature, etc.) exhibits significant correlation with itself or with another variable over a range of space and/or time that is significantly larger than the smallest local scales of the flow." One of the earliest documented coherent structures is the near-wall cycle with an approximate spanwise spacing of a 100 viscous units (Kline *et al.*, 1967). Considering the logarithmic region of the flow, Smits *et al.* (2011), in their review of high Reynolds number wall turbulence, broadly classify the coherent motions in this region into (i) hairpins or horseshoe vortices, (ii) large-scale motions (LSMs) and (iii) very-large-scale motions (VLSMs), otherwise also called 'superstructures' in external flows.

The first of these structures, the hairpin vortices, were proposed by Theodorsen in 1952. The flow visualization studies of Head & Bandyopadhyay (1981) established their importance in wall-bounded flows, which lead to an extensive investigation of these structures (Acarlar & Smith, 1987*a*,*b*, Perry & Chong, 1982). More recently, Wu & Moin (2009) in their DNS study showed that a multitude of these hairpins reside within boundary layer.

More recent work has shown that the spatial organization (or alignment) of many of these hairpins form the LSMs, that are associated with approximate streamwise lengths of $2-3\delta$ (much larger than the characteristic lengths of hairpins) (Adrian *et al.*, 2000, Dennis & Nickels, 2011, Jiménez, 2012, Kim & Adrian, 1999, Zhou *et al.*, 1999). Such 'vortex packets' convecting at the same velocity give rise to elongated regions of low streamwise momentum between their legs, that are flanked on both sides in the spanwise direction by regions of high momentum (Adrian *et al.*, 2000, Brown & Thomas, 1977, Ganapathisubramani *et al.*, 2003, Hutchins *et al.*, 2005, Tomkins & Adrian, 2005). The heads of the individual hairpins within the packet align along a line inclined at $15 - 20°$, which was found to be consistent with the ramp-like features observed by Head & Bandyopadhyay (1981). Adrian (2007) provides a detailed review on hairpins and their organization into packets.

Further, there are very long regions of low momentum called VLSMs (in internal flows) or superstructures (in boundary layer flows), with a meander in the streamwise direction that becomes increasingly prominent away from the wall (Adrian *et al.*, 2000, Balakumar & Adrian, 2007, Guala *et al.*, 2006, Hutchins & Marusic, 2007*b*, Kevin *et al.*, 2019, Kim & Adrian, 1999, Monty *et al.*, 2007, Smits *et al.*, 2011, Tomkins & Adrian, 2005, Vallikivi *et al.*, 2015*a*, Wang & Zheng, 2016). They have been reported to have length scales as long as 30 times the channel half-height in internal flows Monty *et al.* (2007), while in boundary layer flows they have been observed to extend to as much as $10 - 15$ times the boundary layer thickness Hutchins & Marusic (2007*b*). Hutchins & Marusic (2007*a*) noted that the meander makes their detection hard when using 1-D spectral analysis. Although Kim & Adrian (1999) and Adrian *et al.* (2000) speculate that LSMs form the building blocks of VLSMs, this idea is contested in Smits *et al.* (2011) based on the differences in the wall-coherence and the length-scales of the LSMs and the VLSMs in different regions of the flow. The formation of these structures is still a subject of investigation (Smits *et al.*, 2011).

The LSMs and VLSMs are of particular interest in the logarithmic region at high Reynolds numbers, as they contribute to the bulk of the turbulent kinetic energy and the Reynolds shear stress, in comparison to the isotropic small-scales (Balakumar & Adrian, 2007, Guala *et al.*, 2006, Smits *et al.*, 2011, Tomkins & Adrian, 2005) Apart from that, they also have a significant influence on the inner-layer of the flow (Abe *et al.*, 2004, Guala *et al.*, 2011, Hoyas & Jiménez, 2006, Hutchins & Marusic, 2007*a*,*b*, Liu *et al.*, 2019). Hutchins & Marusic (2007*b*) explains that, although these structures do not have a significant wall-normal velocity close to the wall, hence being inactive in the way Townsend describes inactive motions, they superimpose on, as well as modulate the near-wall structures, hence contributing to the Reynolds shear stress in the near-wall region. Based on this, Mathis *et al.*

(2009) and Marusic *et al.* (2010*b*) propose a predictive model of the inner-layer of the flow based on measurements from the outer-layers of the flow, which was later extended by Baars *et al.* (2016) using the concept of spectral linear stochastic estimation. For some of the critical views on whether hairpin vortices are indeed the dominant structures at high Reynolds numbers and on whether they spatially organize to form larger structures, refer to Jiménez (2013, 2018), Schlatter *et al.* (2014).

2.2 Attached eddy model of the logarithmic region

Townsend (1976) proposed the 'attached eddy hypothesis', which conceptualized the boundary layer at very high Reynolds numbers as an assemblage of inviscid inertia-dominated 'eddies'. These eddies are randomly distributed in space and possess the following property: "the velocity fields of main eddies, regarded as persistent, organized flow patterns, extend to the wall and, in a sense, they are *attached* to the wall" (page 152, Townsend, 1976). Marusic & Monty (2019) suggested that the phrase "in a sense" could imply that the velocity fields are influenced by the wall, and are not necessarily physically connected to the wall. The attached eddy hypothesis predicts the logarithmic laws of the streamwise and spanwise turbulence intensities and a constant Reynolds shear stress ($-\overline{uw}^+ \approx 1$) within the logarithmic region, based on the following considerations: (i) the attached eddies are self-similar and their heights are proportional to the distance of their 'centres' from the wall, (ii) the probability density of the eddies within the boundary layer vary inversely with their size (or distance from the wall) and (iii) the eddies possess a constant characteristic velocity scale (U_τ).

Townsend's conceptual framework was extended by Perry & Chong (1982) to a kinematic attached eddy model (AEM) of the logarithmic region by specifying geometric shapes for the eddies. They further showed that the attached eddy hypothesis lead to a logarithmic profile for the mean flow. Following the flow visualization studies of Head & Bandyopadhyay (1981), who observed the boundary layer at low Reynolds numbers to consist of a 'forest' of hairpin vortices, Perry & Chong (1982) chose self-similar 'hierarchies' of Λ-hairpins, with a shear-induced downstream inclination of 45°, to represent the boundary layer. A hierarchy consisted of hairpins with similar heights (and possibly at different stages of 'stretching') and different discrete hierarchies existed due to the 'vortex-pairing' mechanism. Across hierarchies, the size and the probability density of the hairpins varied as directly and inversely proportional to their distance from the wall, respectively. However, the characteristic velocity scale remains the same for all hierarchies and is equal to the friction velocity. Perry & Chong (1982), with such an arrangement of hairpins, derived statistics that were consistent with the attached eddy hypothesis of Townsend (1976). More importantly, the authors obtained, for the first time using a mechanistic model, a link between the mean flow, the Reynolds shear stress, the turbulence intensities and the energy spectra. Another significant outcome of their model was the prediction of a k_x^{-1} scaling in the 1-D streamwise energy spectra (consistent with the similarity arguments of Perry & Abell, 1977).

2.2.1 Similarity from spectral overlap arguments

Further to the work of Perry & Abell (1977) and Perry & Chong (1982), the k_x^{-1} scaling gained support through the spectral overlap arguments of Perry *et al.* (1986). Unlike in Perry & Chong (1982), Perry *et al.* (1986) adopted a continuous distribution for hierarchies, with the size of the smallest and the largest eddies being 100 viscous units and δ_E, respectively, where δ_E is of the order of boundary layer thickness. At $z << \delta_E$ (typical of the logarithmic region), the authors identified the energy spectra to be characterized by three spectral regimes: (i) the low-wavenumber range with contributions from the *inactive* motions due to eddies of scale $\mathcal{O}(\delta_E)$, (ii) the moderate- to high-wavenumber range with contributions from the *active* motions due to eddies of scale $\mathcal{O}(z)$ and (iii) the very-high-wavenumber range where the contributions are from viscosity dependent motions. Using dimensional analysis with U_τ, k_x, z and δ_E as the only variables, Perry *et al.* (1986)

put forth scaling arguments for the spectra of the streamwise velocity component. As per those arguments, at $z << \delta_E$, in the low-wavenumber range, an 'outer-flow' scaling was expected, of the form,

$$\frac{\phi_{uu}(k_x\delta)}{U_\tau^2} = \frac{\phi_{uu}(k_x)}{\delta U_\tau^2} = g_1(k_x\delta). \tag{2.2}$$

Similarly, in the moderate- to high-wavenumber range, an 'inner-flow' scaling was expected, of the form,

$$\frac{\phi_{uu}(k_x z)}{U_\tau^2} = \frac{\phi_{uu}(k_x)}{z U_\tau^2} = g_2(k_x\delta). \tag{2.3}$$

In the viscosity-dependent very-high-wavenumber range, the motions were considered to be locally isotropic (Kolmogorov, 1941) with the important scales being the Kolmogorov length ($\eta = (\nu^3/\epsilon)^{1/4}$) and velocity ($v_\eta = (\nu\epsilon)^{]1/4}$) scales. Here, ϵ is the average turbulent energy dissipation. Therefore, the following classical Kolmogorov (1941) scaling law was expected in the very-high-wavenumber range,

$$\frac{\phi_{uu}(k_x\eta)}{v_\eta^2} = \frac{\phi_{uu}(k_x)}{\eta v_\eta^2} = g_3(k_x\eta). \tag{2.4}$$

Following Townsend's *equilibrium layer* criterion (Townsend, 1961, 1976), Perry *et al.* (1986) assumed the average turbulent energy production (P) equals the average turbulent energy dissipation in the logarithmic region, i.e.,

$$P = -\overline{uw}\frac{\partial U}{\partial z} = \epsilon. \tag{2.5}$$

This, together with the relations, $-\overline{uw} \approx U_\tau^2$ (from the 'constant stress' layer of Townsend, 1976) and $\partial U/\partial z = U_\tau/(\kappa z)$ (alternatively from equation 2.1), can be used to represent the Kolmogorov length and velocity scales as,

$$\eta = \left(\frac{\nu^3\kappa z}{U_\tau^3}\right)^{1/4} \text{ and } v_\eta = \left(\frac{\nu U_\tau^3}{\kappa z}\right)^{1/4}. \tag{2.6}$$

Similar to the overlap arguments of Millikan (1938) for the mean flow, Perry *et al.*

(1986) identified two spectral overlap regions for the three spectral ranges discussed here, and as represented in figure 2.2. In the 'Overlap region I', the inner-flow and outer-flow scalings (equations 2.2 and 2.3 respectively) are simultaneously valid, leading to,

$$g_1(k_x\delta) = \frac{A_1}{k_x\delta} \quad \text{and} \quad g_2(k_xz) = \frac{A_1}{k_xz}. \tag{2.7}$$

Consequently, the pre-multiplied energy spectra should follow the much debated k_x^{-1} scaling,

$$\frac{k_x\phi_{uu}(k_x)}{U_\tau^2} = A_1, \tag{2.8}$$

where A_1 is a universal constant, also known as the Townsend-Perry constant (Marusic *et al.*, 2013). The expected k_x^{-1} scaling, as sketched by Perry *et al.* (1986), in the 1-D streamwise energy spectra is shown in figure 2.3.

Similarly, in the 'Overlap region II' (figure 2.2), the inner-flow scaling and Kolmogorov scaling (equations 2.2 and 2.4 respectively) are simultaneously valid. Together with equation 2.6, the overlap argument yields,

$$g_2(k_xz) = \frac{\phi_{uu}(k_xz)}{U_\tau^2} = \frac{1}{\kappa^{2/3}}\frac{K_0}{(k_xz)^{5/3}}, \tag{2.9a}$$

$$g_3(k_x\eta) = \frac{\phi_{uu}(k_x\eta)}{v_\eta^2} = \frac{K_0}{(k_x\eta)^{5/3}}, \tag{2.9b}$$

where K_0 is the universal Kolmogorov constant. Equation 2.9 is commonly referred to as the Kolmogorov $k^{-5/3}$ scaling and the 'Overlap region II' is often called the 'inertial subrange'.

At $z << \delta$, the spectra of the spanwise velocity component, ϕ_{vv}, follows scaling arguments similar to ϕ_{uu}, with the constant A_1 in equation 2.8 replaced with a different universal constant, A_2. In the case of the spectra of the wall-normal velocity component, ϕ_{ww}, the overlap arguments are different. The contributions to w approach zero due to the non-penetration boundary condition of the wall and the (*inactive*) motions get restricted to the wall-parallel plane. Therefore, at a particular wall-height z, only those eddies with heights $\mathcal{O}(z)$ contribute to

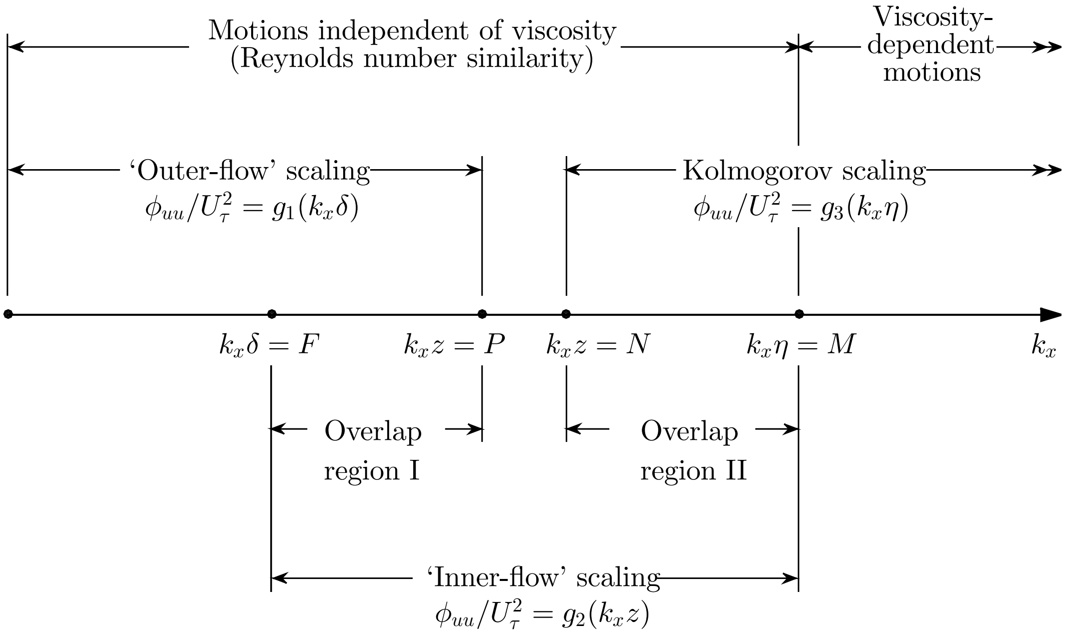

FIGURE 2.2: An overview of various spectral regions in the 1-D streamwise spectra of u and v in the logarithmic region. Adapted from Perry *et al.* (1986).

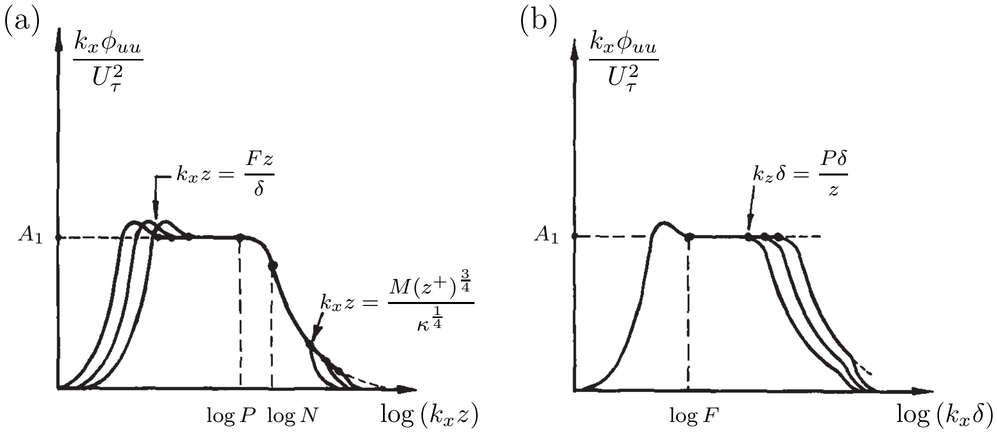

FIGURE 2.3: Sketches of the expected distributions of the pre-multiplied spectra of u with (a) inner-flow scaling and (b) outer-flow scaling. Adapted from Perry *et al.* (1986).

ϕ_{ww} (unlike in the case of ϕ_{uu} and ϕ_{vv}, where all eddies with sizes $\mathcal{O}(z)$ to $\mathcal{O}(\delta)$ contribute). Therefore, ϕ_{ww} does not follow an outer-flow scaling, resulting in a single region of overlap (as shown in figure 2.4) where,

$$\frac{\phi_{ww}(k_xz)}{U_\tau^2} = h_2(k_xz) \quad \text{and} \quad \frac{\phi_{ww}(k_x\eta)}{v_\eta^2} = h_3(k_x\eta) \tag{2.10}$$

are simultaneously valid. The sketches of the expected scaling of ϕ_{ww}, adapted from Perry *et al.* (1986), are shown in figure 2.5.

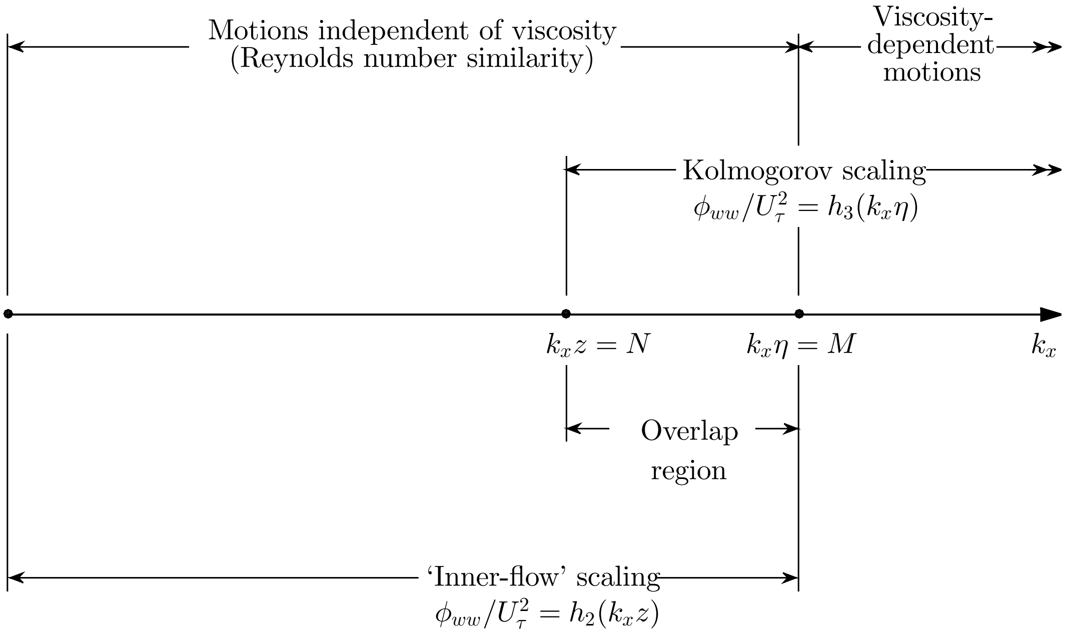

FIGURE 2.4: An overview of various spectral regions in the 1-D streamwise spectra of w in the logarithmic region. Adapted from Perry *et al.* (1986).

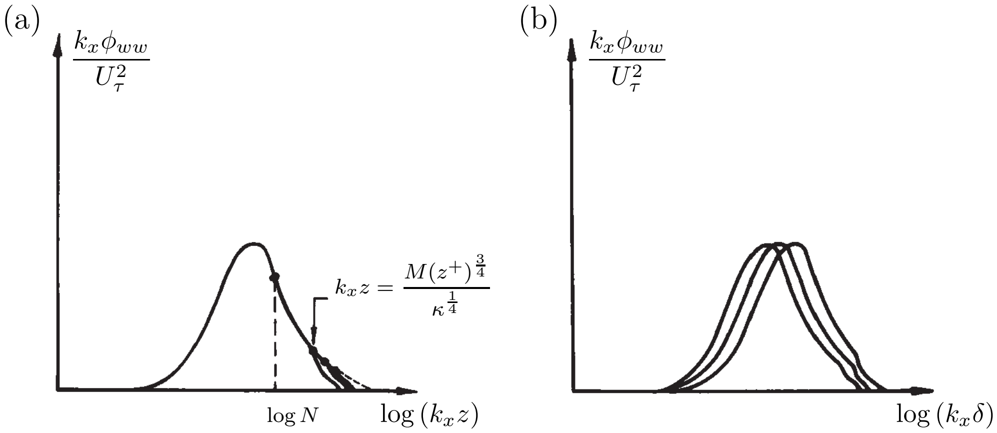

FIGURE 2.5: Sketches of the expected distributions of the pre-multiplied spectra of w with (a) inner-flow scaling and (b) outer-flow scaling. Adapted from Perry *et al.* (1986).

Integration of ϕ_{uu}, ϕ_{vv} and ϕ_{ww} across the energetic-wavenumber range yields the profile of $\overline{u^2}^+$, $\overline{v^2}^+$ and $\overline{w^2}^+$, respectively, as given by,

$$\overline{u^2}^+ = -A_1 \log(z/\delta) + B_1, \tag{2.11a}$$

$$\overline{v^2}^+ = -A_2 \log(z/\delta) + B_2, \tag{2.11b}$$

$$\overline{w^2}^+ = B_3, \tag{2.11c}$$

where, A_1 and A_2 are the universal constants defined above.

There has been a lot of effort put towards refining the AEM of Perry (1982) and Perry *et al.* (1986) based on experimental observations, with the objective of using the AEM to better predict the Reynolds stresses, energy spectra, structure functions and higher-order moments (eg. Baidya *et al.*, 2017, Marusic, 2001, Marusic & Perry, 1995, de Silva *et al.*, 2016, Woodcock & Marusic, 2015, Yang *et al.*, 2017). Many of these studies prescribed new shapes to the representative eddies, as opposed to the basic Λ-type hairpins of Perry & Chong (1982). However, all of these studies reinforced the underlying self-similarity assumptions of Townsend (1976). A detailed review of the AEM, and the many empirical studies that tested its self-similarity assumptions, is provided by Marusic & Monty (2019).

2.2.2 Spectral similarity from high-*Re* data

The similarity arguments discussed above are expected to hold only at high Reynolds numbers, as they require sufficient separation of scales. The logarithmic law in the mean velocity (as discussed in §2.1) and the trends of the Reynolds stresses as shown in equation 2.11, have received much support from high Reynolds number experiments (Baidya *et al.*, 2017, Hultmark *et al.*, 2012, Kunkel & Marusic, 2006, Nickels *et al.*, 2007, Talluru *et al.*, 2014*a*) and recent DNS studies (Lee & Moser, 2015, Pirozzoli & Bernardini, 2013, Sillero *et al.*, 2013). However, discerning the similarity trends from the energy spectra has been challenging. While there has been convincing experimental evidence for the Kolmogorov $k_x^{-5/3}$ scaling in the inertial subrange (Saddoughi & Veeravalli, 1994, Samie *et al.*, 2018, Sreenivasan, 1995), thereby validating the assumption of 'local isotropy' in the very-small-scales, the existence of the k_x^{-1} scaling is still debated.

The k_x^{-1} scaling of the 1-D spectra of u is of specific interest in wall-bounded flows, as it indicates the presence of geometrically self-similar structures whose sizes scale with the distance from the wall (Perry & Chong, 1982). One of the first studies to support k_x^{-1} scaling, from high Reynolds number measurements in a controlled laboratory setting, was reported by Nickels *et al.* (2005). At $Re_\tau \approx 14000$, they observed a k_x^{-1} scaling for $z^+ > 100$ and $z/\delta < 0.019$ in the wavelength range of $\lambda_x/z > 15.7$ and $\lambda_x/\delta < 0.3$. However, Baars & Marusic (2018*a*) argued that the k_x^{-1} plateau observed by Nickels *et al.* (2005) could be the 'saddle-type topology' formed when the inner-spectral peak transitions to the outer-spectral peak. Moreover, the value of the constant A_1 obtained from the k_x^{-1} scaling observed by Nickels *et al.* (2005) was not consistent with the slope of the profile of $\overline{u^2}^+$ within the logarithmic region. No clear evidence of the k_x^{-1} scaling was discernible even from the measurements at higher Reynolds numbers (up to $Re_\tau \sim 10^5$) that followed (Baidya *et al.*, 2017, Rosenberg *et al.*, 2013, Vallikivi *et al.*, 2015*a*), although theory suggests that this scaling becomes more conspicuous with increasing Re_τ.

Nevertheless, k_x^{-1} scaling is commonly assumed in atmospheric boundary layer research (Calaf *et al.*, 2013, Högström *et al.*, 2002, Hunt & Morrison, 2000). Katul & Chu (1998) provides a comprehensive review of this. Kunkel & Marusic (2006) point out that the large length and time scales involved in the atmospheric surface layer flows often affect the convergence of low- to moderate-wavenumbers, and consequently, discerning a k_x^{-1} scaling from a pre-multiplied spectra is reportedly difficult from such measurements. Interestingly, some of the recent high Reynolds number DNS studies (up to $Re_\tau \approx 5200$) suggests that the k^{-1} scaling becomes more evident when the 1-D spectrum of u is measured as a function of spanwise wavenumbers k_y (Lee & Moser, 2015, Pirozzoli & Bernardini, 2013).

Possible reasons for an inconclusive k_x^{-1} scaling

The k_x^{-1} scaling in 1-D streamwise spectra is arguably the most popular tool that has been put forth to probe geometric self-similarity in high Reynolds number turbulent boundary layers. While some of the previous studies suggest that the measurement technique (Hutchins *et al.*, 2009) and the geometry of the flow (Chung *et al.*, 2015) could affect the k_x^{-1} scaling in the 1-D streamwise spectra, some recent studies highlight the inherent limitations of single-point measurements (and hence a 1-D spectrum) to isolate the self-similar scales. Synchronous two-point measurements enabled Baars *et al.* (2017) to compute the 1-D linear coherence spectra (LCS) at high Reynolds numbers. The authors reported evidences supporting self-similarity even when a k_x^{-1} scaling was lacking in the 1-D streamwise spectrum. Later, with similar coherence based filters, Baars & Marusic (2018*a*) performed a triple decomposition of the 1-D energy spectrum and isolated the energy contributions from wall-attached self-similar structures that are typical of Townsend's (1976) attached eddies or the 'type-A' eddies of Perry & Marusic (1995) and Marusic & Perry (1995). Baars & Marusic (2018*a*) reported that the energy contribution from such self-similar eddies often overlap with the energy contributions of the non-self-similar very-large-scale motions and the energetic detached structures (Jiménez & Hoyas, 2008, Marusic & Perry, 1995), consequently masking a potential k_x^{-1} scaling at least up to $Re_\tau \approx 80000$.

As discussed in §1.1, another concern raised by Davidson *et al.* (2006) is that 'aliasing' contaminates the 1-D streamwise spectrum by artificially shifting energy to lower wavenumbers (or larger wavelengths). Davidson (2015) defines aliasing as the "tendency for one-dimensional spectra to give a misleading impression of three-dimensional processes." As illustrated in figure 2.6 (adapted from Tennekes & Lumley, 1972), a 1-D spectrum obtained with a single-point measurement would show a peak at λ_1 for both the cases (a) and (b), because the shorter waves ($\lambda_2 < \lambda_1$) are inclined to the direction of measurement.

2.2.3 Two-dimensional energy spectrum

In wall-bounded flows, a direct measurement of the 2-D energy spectrum, which is a function of both k_x and k_y, avoids the aliasing problem, that was discussed above, in the homogeneous directions (Tennekes & Lumley, 1972). While 2-D energy spectra are more commonly used in numerical studies to gain structural information of turbulence (for example, del Álamo *et al.*, 2004, Jiménez & Hoyas, 2008, Kraheberger *et al.*, 2018), its use in experimental studies is rare. One of the earliest experiments was carried out by Morrison & Kronauer (1969) using hot-wire anemometry and they investigated the 2-D frequency-transverse wave number spectra in narrow frequency bands to report structural self-similarity in

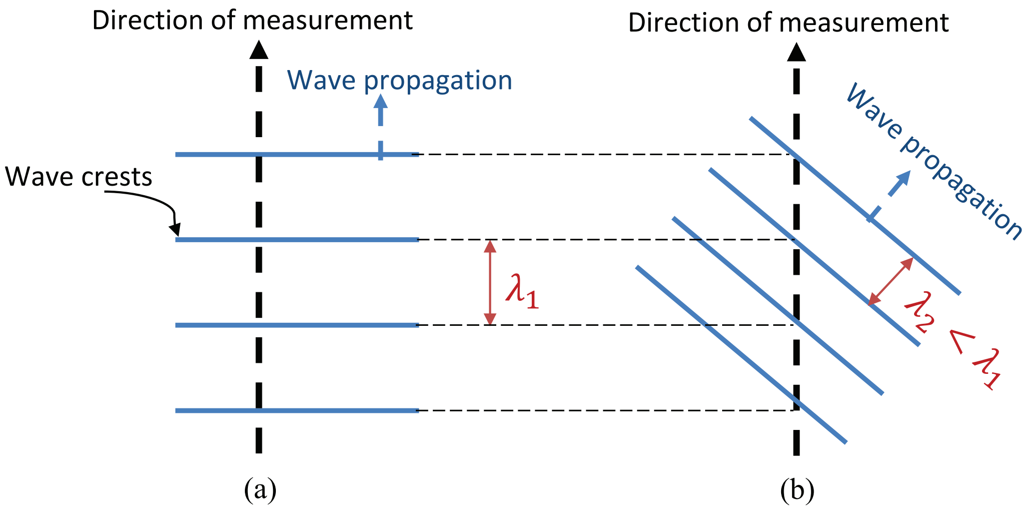

FIGURE 2.6: Depiction of aliasing in 1-D spectra: (a) wave propagates along the direction of measurement and (b) wave propagates oblique to the direction of measurement. Adapted from Tennekes & Lumley (1972).

the logarithmic region of a fully developed pipe flow. In turbulent boundary layers, 2-D spectral information at low to moderate Reynolds numbers were obtained by Tomkins & Adrian (2005) using particle image velocimetry (PIV). They studied the average growth of energetic motions throughout the logarithmic region by considering the energy containing spanwise modes for various streamwise length scales.

The 2-D spectra can also be used as a tool to observe self-similarity. Chung *et al.* (2015) put forth a dimensional consideration of the 2-D spectrum in the inertial region. They considered a constant-energy region in the 2-D spectrum to be bounded by $\lambda_y/z = \lambda_L/z \sim f_1(\lambda_x/z)$ and $\lambda_y/z = \lambda_U/z \sim f_2(\lambda_x/z)$, as shown in figure 2.7. Here, f_1 and f_2 are arbitrary power laws and $[\lambda_L, \lambda_U]$ represent the range of spanwise wavelengths (*eddy-widths*) associated with a particular streamwise wavelength λ_x (*eddy-length*). This 2-D spectrum is related to the 1-D streamwise energy spectrum as,

$$\frac{k_x\phi_{uu}(k_x)}{U_\tau^2} = \int_{\lambda_L}^{\lambda_U} \frac{k_x k_y \phi_{uu}(k_x, k_y)}{U_\tau^2}\, \mathrm{d}\left(\log \frac{\lambda_y}{z}\right). \tag{2.12}$$

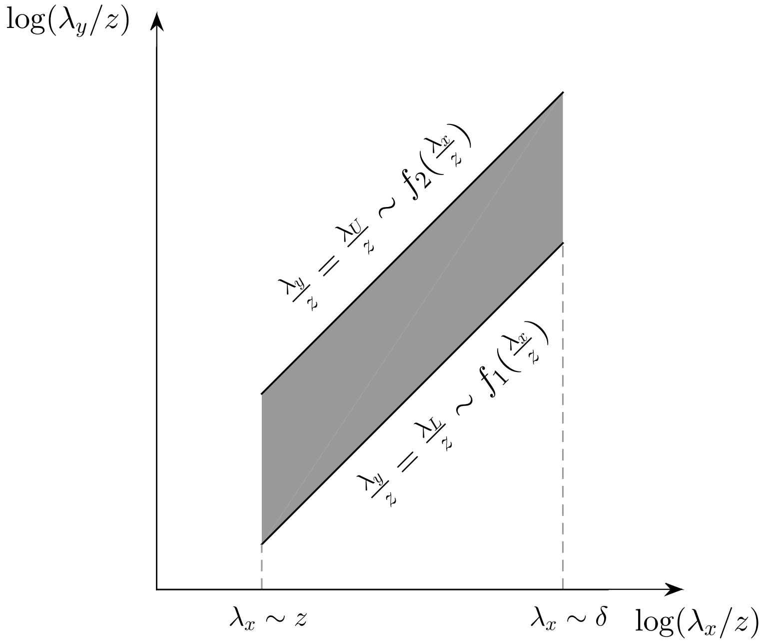

FIGURE 2.7: An illustration of the 2-D spectrum of u. The grey patch bounded by $[\frac{\lambda_L}{z}, \frac{\lambda_U}{z}]$ indicates a region of constant energy. Adapted from Chung *et al.* (2015).

If $k_x k_y \phi_{uu}(k_x, k_y)/U_\tau^2 \approx 1$ is assumed for simplicity,

$$\frac{k_x \phi_{uu}(k_x)}{U_\tau^2} \approx \log\left(\frac{\lambda_U}{\lambda_L}\right). \tag{2.13}$$

Based on this, the authors argued that in order to have a k_x^{-1} behaviour in the 1-D spectrum, equation 2.13 is required to be a constant (and equal to A_1), and therefore the power laws f_1 and f_2 have to be identical. Based on Townsend's (1976) attached eddy hypothesis, to satisfy the assumption of geometric self-similarity, f_1 and f_2 should represent linear relationships. However, del Álamo *et al.* (2004) examined the 2-D spectra of u from direct numerical simulations (DNS) of a channel flow at $Re_\tau \leq 1900$ and showed that such a region of constant energy is bounded at larger scales by a square-root relationship of the form $\lambda_y/z \sim (\lambda_x/z)^{1/2}$ (figure 2.8). The authors reported this square-root relation between the *lengths* and *widths* of the structures to indicate a failure of self-similarity, which, based on the arguments above, would require a $\lambda_y \sim \lambda_x$ relationship instead. To obtain further clarification of these arguments and test the validity of Townsend's (1976) self-similarity assumptions, it is significant to obtain the 2-D spectra at high Reynolds

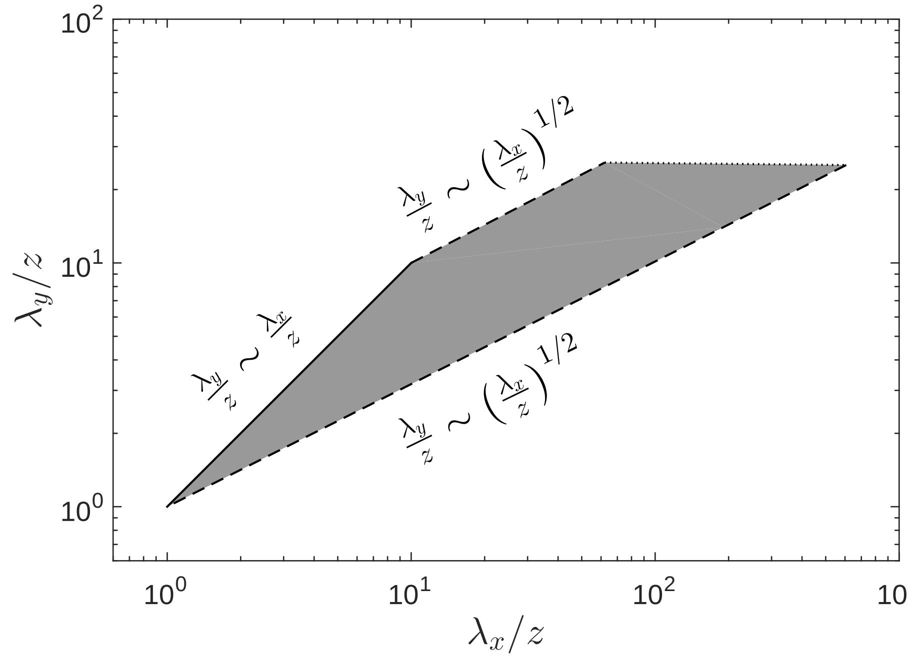

FIGURE 2.8: Sketch of the organization of a region of constant energy in the 2-D spectrum of u at $Re_\tau \approx 2000$. Adapted from del Álamo *et al.* (2004).

numbers and thereby identify the functional relationships f_1 and f_2 (figure 2.7) proposed by Chung *et al.* (2015).

Chapter 3

Experiment setup

3.1 Low Reynolds number facility

The low Reynolds number experiments ($Re_\tau = 2430$ and 4210) are conducted in the open return turbulent boundary layer wind tunnel (low-*Re* facility) located in the Walter Bassett Aerodynamics Laboratory at The University of Melbourne. As shown in figure 3.1, a centrifugal fan driven by a 19 kW DC motor, delivers the air to the working section. The flow passes through the settling chamber, comprising honeycombs and mesh screens and followed by a 8.9:1 contraction. The freestream turbulence level is maintained below 0.2% in the working section, which is 6.7 m long with a cross-sectional area of 0.94×0.375 m^2. The fully adjustable roof of the wind tunnel allows for conducting measurements at different streamwise pressure gradients. However, in the present study, all the measurements are carried out at zero pressure gradient (ZPG) and at a streamwise location of $x = 3.8$ m. A coarse 40 grit sand paper trip at the inlet of the working section trips the boundary layer to a turbulent state (consistent with Kulandaivelu (2012)) resulting in a boundary layer thickness of $\delta \sim 7$ cm at the measurement location. The boundary layer thickness δ is computed by fitting the mean velocity profile to the composite profile of Chauhan *et al.* (2009) and the friction velocity, U_τ, is obtained by a Clauser chart method using the log law constants, $\kappa = 0.4$ and $A = 5$.

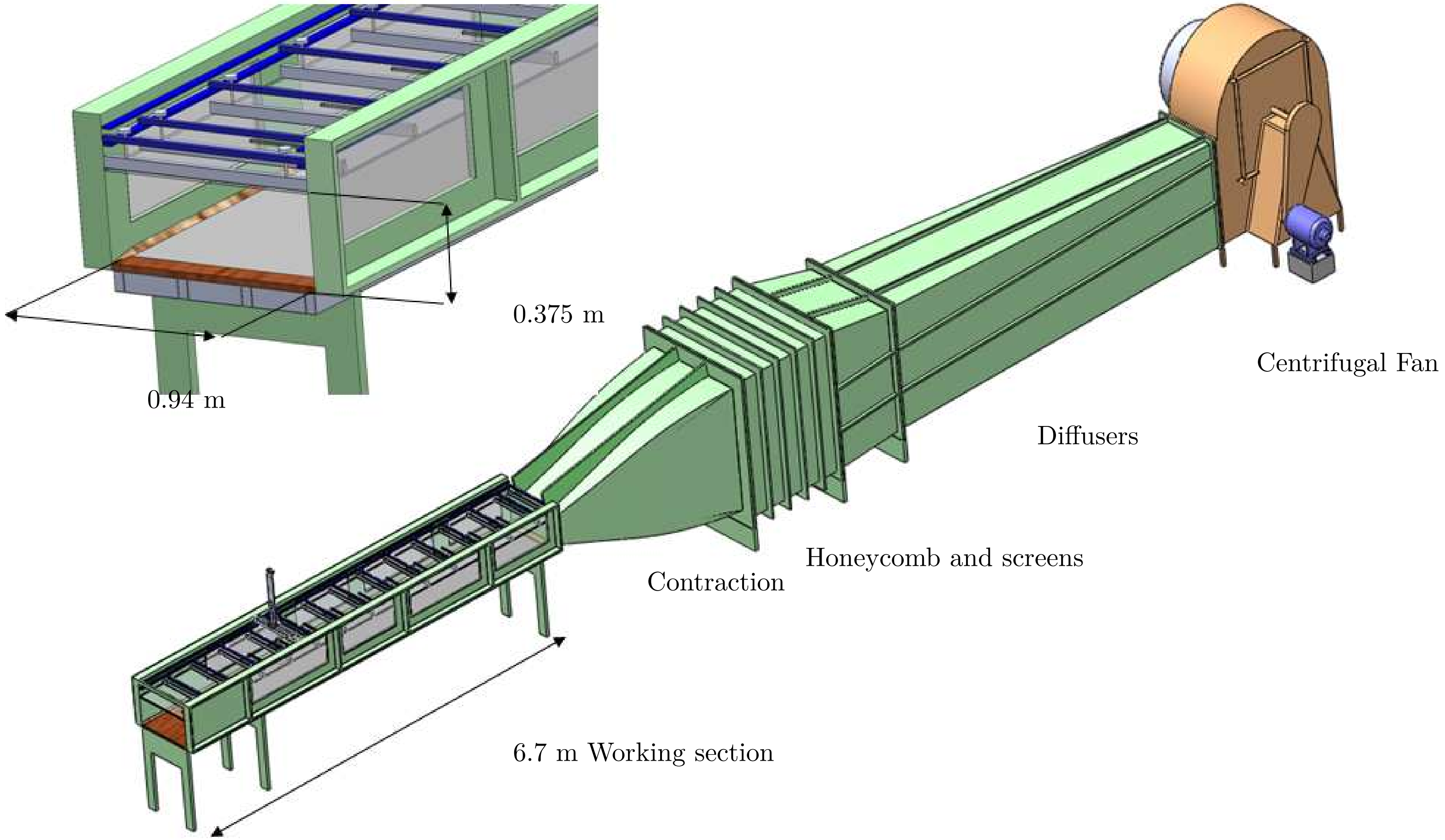

Figure 3.1: A schematic of the Low-*Re* facility located in the Walter Bassett Aerodynamics Laboratory, The University of Melbourne. Adapted from Nugroho (2015).

The experimental technique at low-Re uses two single-wire hot-wire probes: HW1 and HW2. The details of the hot-wire anemometry, calibration of hot-wires and data acquisition are provided in the following sections. While HW1 is stationed at a fixed streamwise-spanwise location, HW2 is traversed in the spanwise direction relative to HW1, while acquiring signals synchronously from both the hot-wires. The hot-wires are sampled for ~ 40 discrete spanwise separations, with the spacing between the hot-wires increasing logarithmically from an initial separation of $\Delta y \approx 0.025\delta$, up to a final spacing of $\Delta y \approx 2.8\delta$. To this end, a fully automated 2-D traverse is used. The traverse is mounted on the roof of the tunnel and the long cylindrical sting, which carries the sensor (HW2), moves along the spanwise/wall-normal directions through sealed slots provided on the roof. Two Vexta PKK266M-03A stepper-motors, connected to Velmex VXM-2 controllers, drive the traverse along the wall-normal and spanwise directions. The wall-normal traverse is equipped with an optical encoder with an accuracy of $\pm 0.5\,\mu$m. The distance from the wall of the stationary hot-wire (HW1) is adjusted using a Mellis Griot linear translation stage, with a least count of $10\,\mu$m. Further details of the facility can be found in Nugroho (2015) and the measurement technique is detailed in chapter 4.

3.2 High Reynolds number facility

The high Reynolds number experiments ($Re_\tau = 15100$, 20250 and 26090) are conducted in the High Reynolds Number Boundary Layer Wind Tunnel (HRNBLWT) facility located in the Walter Bassett Aerodynamics Laboratory at The University of Melbourne. Figure 3.2, adapted from Kulandaivelu (2012), shows a schematic of the facility. The bell mouth entrance ensures the air passes in smoothly with minimal separation and noise. A heat exchanger following the plenum maintains the air temperature within ±0.1°C. At the following chamber, the cross-section smoothly transitions from rectangle to circle at the inlet of the fan. The massive axial fan, powered by a 250 kW DC motor, is capable of delivering, at its full capacity, 45 m/s air flow in the working section ($27 \times 2 \times 1$ m). The motor can be remotely controlled and hence a full automation of the test procedure, which includes hot-wire calibration at different air speeds, is possible. After the fan assembly, the air expands into the chamber, comprising two guide vane cascades, which gradually turns the flow by 180° into the settling chamber. The flow straightener (honeycomb) and the series of fine meshes that follows, maintain the freestream turbulence at the working section to be less that 0.3%, for the measured range of velocities. After the mesh series, a 6.25:1 contraction accelerates the flow into the working section. A coarse 40 grit sand paper, at the inlet of the working section, trips the air flow to produce a 'canonical' turbulent boundary layer in the working section (Marusic *et al.*, 2015).

The 27 m long working section floor is constructed using polished aluminium plates with a surface roughness less than 1.5 μm (Nickels *et al.*, 2007) and the ceiling of the working section comprises a series of medium-density fibre board panels with embedded spanwise slots for bleeding air. A ZPG flow, with the pressure coefficient C_p being a constant within ± 0.87%, is set up for all the present measurements with an adjustable ceiling (Marusic *et al.*, 2015).

As shown in figure 3.2, a 2.7 m long and 0.7 m wide drag balance is located at a distance of 19.5 m downstream of the working section inlet. The floor at this section is made of nine interchangeable aluminium plates, each with a dimension of 0.3 m × 0.7 m. All the current measurements are carried out at this section of the tunnel, at a streamwise distance of $x \approx 21$ m from the inlet. Measurements are conducted at freestream velocities of $U_\infty = 20$, 30 and 40 m/s amounting to a friction Reynolds number of $Re_\tau = 15100$, 20250 and 26090 respectively. The boundary layer thickness (δ), defined by fitting the velocity profile to the composite profile of Chauhan *et al.* (2009), varies subtly from $\delta = 0.37$ m to 0.337 m with increasing Re_τ considered here. Since the smallest length scale is $\nu/U_\tau = \delta/Re_\tau$, such a thick boundary layer at the measurement location (following the *big and slow* approach) enables the smallest scales to be resolved using the conventional measurement techniques. Here, U_τ is determined using a Clauser fit approach with $\kappa = 0.39$ and $A = 4.3$ spanning the logarithmic region limits of Marusic *et al.* (2013).

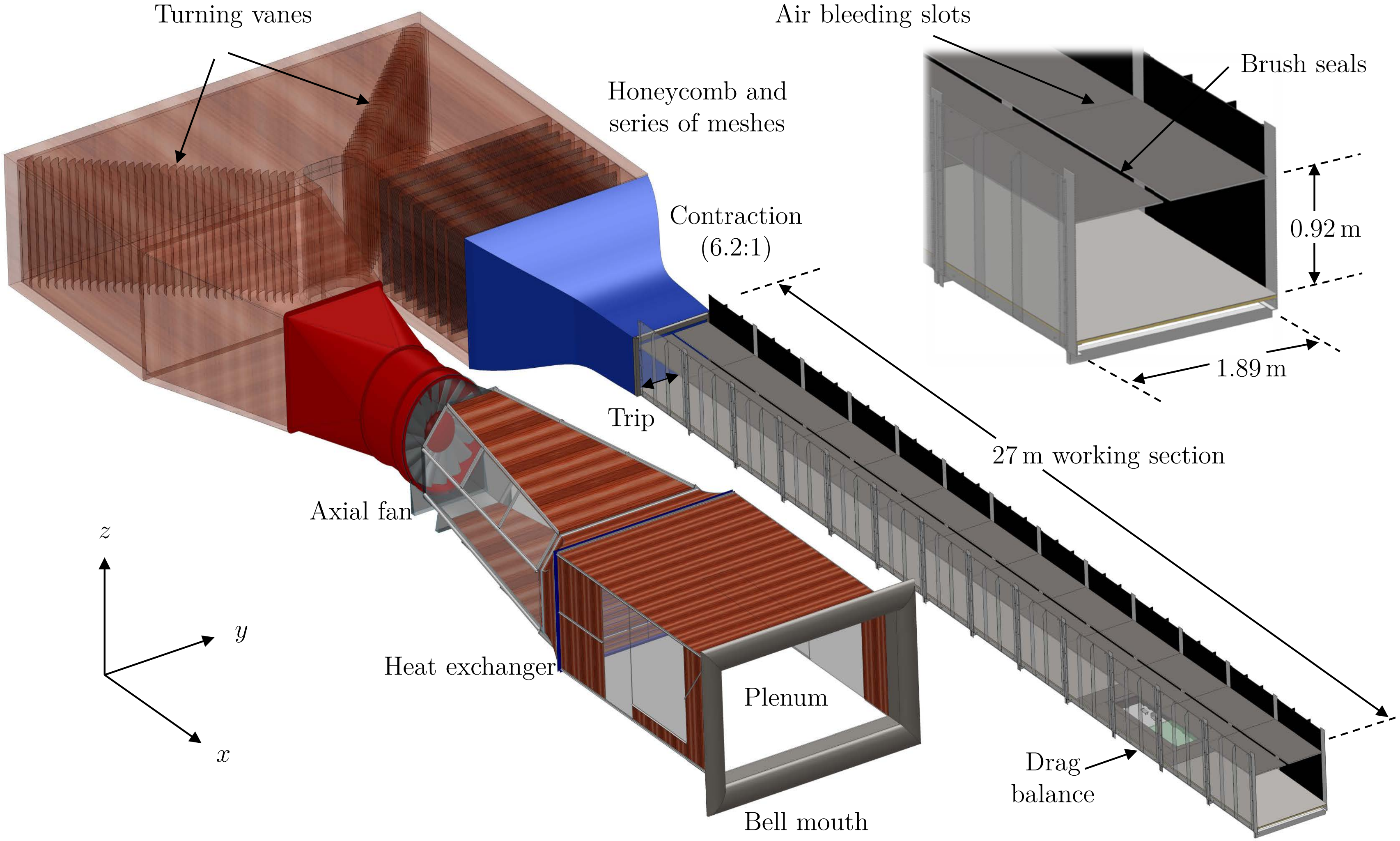

Figure 3.2: A schematic of the High Reynolds Number Boundary Layer Wind Tunnel located in Walter Bassett Aerodynamics Laboratory, The University of Melbourne. Adapted from Kulandaivelu (2012).

3.2.1 Hot-wire arrangement

For the current measurements, one of the nine aluminium plates in the drag balance is replaced with a custom made instrument plate, which houses the traverse systems, as shown in figure 3.3. Due to the space constraints in the tunnel and also to reduce the duration of the experiment, the measurement setup employs four hot-wire probes (1 to 4 as shown in the figure) that are carried by three traverse mechanisms.

Traverse 2, which carries HW3, is the major traversing mechanism in HRNBLWT and is identical to Kulandaivelu (2012). Traverse 2 allows fully automated movement in the streamwise (possible with the streamwise slot provided in the ceiling) and wall-normal directions. A linear optical encoder (Reinshaw RGH24) with a feedback mechanism enforces a positional accuracy of $\pm 0.5\,\mu$m in the wall-normal movement. Any blockage effect is avoided by using a streamlined body (NACA 0016) for the traverse and a very long arm for the probe holder which enables measurements sufficiently upstream of the traverse body (Kulandaivelu, 2012). The flow-induced vibrations are significantly dampened by anchoring the traverse to the floor using a retractable pneumatic foot.

Traverse 1 and Traverse 3 are attached to the custom made instrument plate (0.3 m × 0.7 m). Traverse 3, which carries HW4, moves only in the wall-normal direction and Traverse 1, carrying HW1 and HW2, moves both in the wall-normal and spanwise directions. In order to reduce any blockage effects, most parts of the traverse system exposed to the flow have airfoil cross-sections. The horizontal airfoil in Traverse 1, which is custom made for the present measurements, is supported by a pair of 8 mm diameter rods that slide inside the 10 mm wide spanwise slot (brush sealed) provided in the instrument plate. The diameter of the rods and the location of the support points in the airfoil are optimized so as to reduce the blockage effect, to minimize the width of the slot in the instrument plate and to minimize the flow-induced vibration of the probes. The flow-induced vibration of the hot-wire probes carried by Traverse 1 was studied. To this end, a time series of vertical and horizontal displacements of the probe-tip was acquired using a high

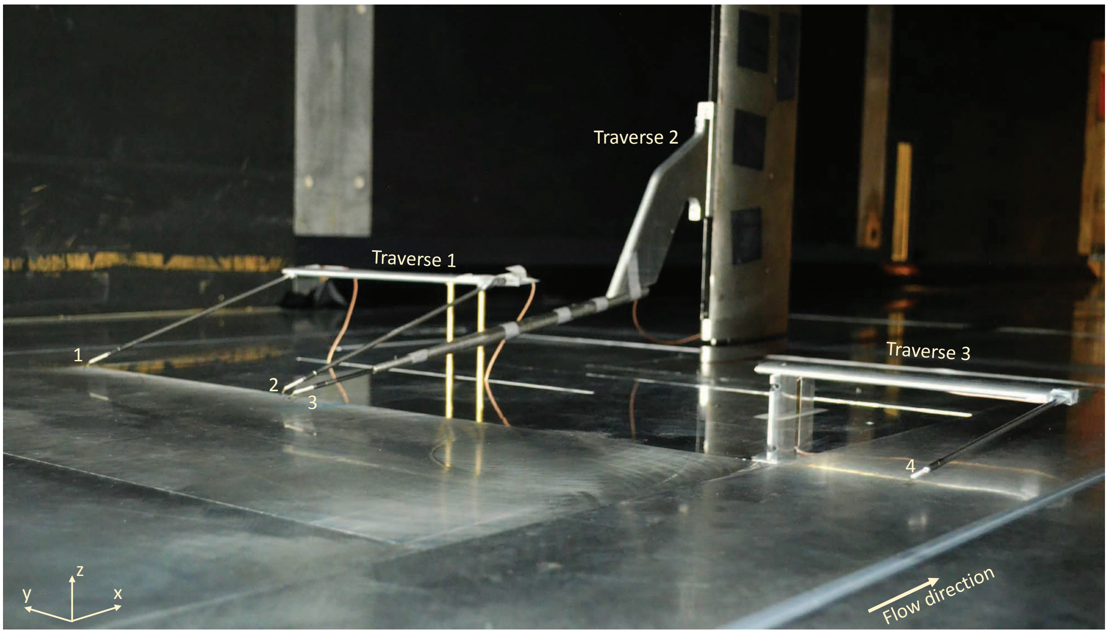

FIGURE 3.3: The arrangement of hot-wires along with the traverses inside the HRNBLWT.

resolution camera, at $U_\infty = 20$ m/s. The results showed the viscous-scaled root-mean-square vertical and horizontal displacements of the probe tip to be small enough (~ 1). The movements of Traverse 1 were constantly monitored using a digital scale within an accuracy of 0.01 mm.

At the start of the measurement, HW2 and HW3 are as close as practicable to each other with $dy_{initial} \approx 0.01\delta$ as the initial spacing between them. HW3 and HW4 are stationed at a fixed spanwise location, whereas HW1 and HW2 are traversed together in the spanwise direction (with logarithmic spacing), while acquiring the data simultaneously from all the hot-wires. Hence the distance between hot-wire pairs, HW1 and HW2 is fixed at all times as is the distance between HW3 and HW4. The maximum spanwise spacing achieved with the current arrangement is about 2.7δ (≈ 1 m in physical units) between HW1 and HW4 at the last measurement point. The measurement technique is detailed in chapter 5.

3.3 Hot-wire positioning

Prior to the start of the measurement, the following steps are performed to accurately position all the hot-wires: (i) ensure all the hot-wire sensors are parallel to the wall, (ii) record the initial spacing between the closest hot-wires ($dy_{initial}$), i.e., the initial spacing between HW1 and HW2 for low-Re experiments and that between HW2 and HW3 for high-Re experiments, (iii) ensure all the hot-wire sensors are at a fixed streamwise position, and (iv) set the initial wall-normal position of all the hot-wires. Steps (i) and (ii) are performed using a wall-parallel microscope connected to a digital camera (AmScope). The divisions in the microscope are scale-calibrated which enables accurate measurement of the spacing (centre-to-centre) between the hot-wires. For step (iii), the streamwise alignment of the hot-wire sensors are set using a FatMax cross line laser level. Finally, the initial wall-normal positions of all the hot-wires are individually set to the required value using a displacement microscope from Titan tool supply that could be connected to the AmScope digital camera. The microscope has a shallow depth of focus of approximately 30 μm and its vertical shift could be recorded using a digital indicator with a fine resolution of 1 μm. The wall-normal position of a hot-wire is measured by first focusing the microscope on to the wall surface and then shifting the focus on to the hot-wire sensor. The difference between the two readings indicates the distance of the sensor from the wall. However, to account for the aerodynamic loading, slight adjustment in the wall-normal location ($\sim 50\,\mu$m) is made, after the calibration of the hot-wires and immediately before the measurement, by monitoring the mean velocity from all the hot-wires.

3.4 Hot-wire probes and their operation

Single sensor, boundary layer type miniature wire probes from Dantec (55P15) are used in the present study. The spacing between the prongs is 1.5 mm and the shape of the prongs allow measurements very close to the wall. Wollaston wires are soldered on to the prong tips and etched at the centre to reveal the platinum sensing element. The sensor length (l) is 0.5 mm and diameter is 2.5 μm.

Hot-wires are operated using in-house Melbourne University Constant Temperature Anemometers (MUCTA) in all cases. The overheat ratio, which decides the temperature of the wire, is maintained to be 1.8 (Samie, 2017). Prior to the measurement, all the hot-wires are annealed at this overheat ratio for about seven hours in order to stabilize them (Perry, 1982). We adopt the method suggested by Perry (1982) to estimate the frequency response of the system, which includes both the constant temperature anemometer (CTA) and the hot-wire. The method involves perturbing the anemometer circuit using a square wave voltage (inbuilt in MUCTA) and the dynamic response of the CTA-hot-wire system is measured. The test is performed with the probe at the freestream to avoid any additional perturbation induced by the turbulent field. The frequency response was approximately 25 kHz at a velocity of $U_\infty/3$ (corresponding to the mean velocity at $z^+ = 15$ where turbulence intensity is the highest) and the lowest being 18 kHz at zero freestream velocity.

3.4.1 Data acquisition

All hot-wires, used in a given experiment, are simultaneously sampled using DT9836 Data Translation 16-bit data-acquisition board in the range of ±10 V. The sampling frequencies for measurements at high-Re are $f_s = 50$, 70 and 100 kHz for $U_\infty = 20$, 30 and 40 m/s respectively and $f_s = 30$ kHz for low-Re measurements. Following the Nyquist criterion, temporal aliasing is avoided by low-pass filtering the signals at a cut-off frequency of $f_c = f_s/2$ using Frequency Devices 9002-LP00. When scaled in viscous units, $f_c^+ (= f_c\,\nu/U_\tau^2)$ varies between 0.5 to 0.9 across the range of Reynolds numbers measured in the present study. These values of f_c^+ are significantly above the maximum frequency of the energetic scales in the boundary layer ($f_{max}^+ = 0.33$) as reported by Hutchins *et al.* (2009). The total sampling times (T) of the hot-wires are selected such that the non-dimensional boundary layer turnover times (TU_∞/δ), associated with the largest structures in the flow, are $\mathcal{O}(10^4)$. Such long sampling durations help accomplish sufficient convergence of the largest length scales in the energy spectra.

3.4.2 Calibration

All hot-wires are calibrated immediately before and after each measurement, allowing compensation for drift in the hot-wire voltage during the measurements. The calibration of HW2 in the low-*Re* facility and HW3 in the HRNBLWT are carried out in the freestream with a Pitot-static probe. A 10 Torr698A MKS Baratron differential pressure transducer, along with MKS 270 signal conditioner, measures the pressure difference from the Pitot-static probe. At the start of every measurement, the sensitivity of the transducer is set to the highest with a zero correction performed. The number of calibraiton points are 15 and 25 respectively, for the low- and high-*Re* measurements. The hot-wire voltages are converted to velocities using a third-order polynomial fit to the calibration data (Bruun, 1995). Any drift in these freestream-calibrated hot-wires were accounted for following the single point recalibration technique discussed in Talluru *et al.* (2014*b*). The current arrangement of the hot-wires did not allow HW1 in the low-*Re* facility and hot-wires HW1, HW2 and HW4 in the HRNBLWT to move to the freestream. Therefore, they are calibrated while inside the boundary layer using the freestream-calibrated hot-wire, i.e, HW2 and HW3 respectively in low-*Re* facility and HRNBLWT. This is achieved by placing all the wires at the same wall-normal location (corresponding to the wall-height of a given measurement) inside the boundary layer. Any-drift in the hot-wires calibrated inside the boundary layer were accounted for by interpolating the pre- and post-calibration data with time. Extreme care is taken to minimize any error associated with the in-boundary layer calibration method. In order to ensure the convergence of mean velocity while inside the boundary layer, the hot-wires are sampled for a longer time, corresponding to $TU_\infty/\delta \approx 10000$. Furthermore, a good agreement is observed between the 1-D streamwise spectra computed from all the hot-wires in the measurement with a maximum uncertainty

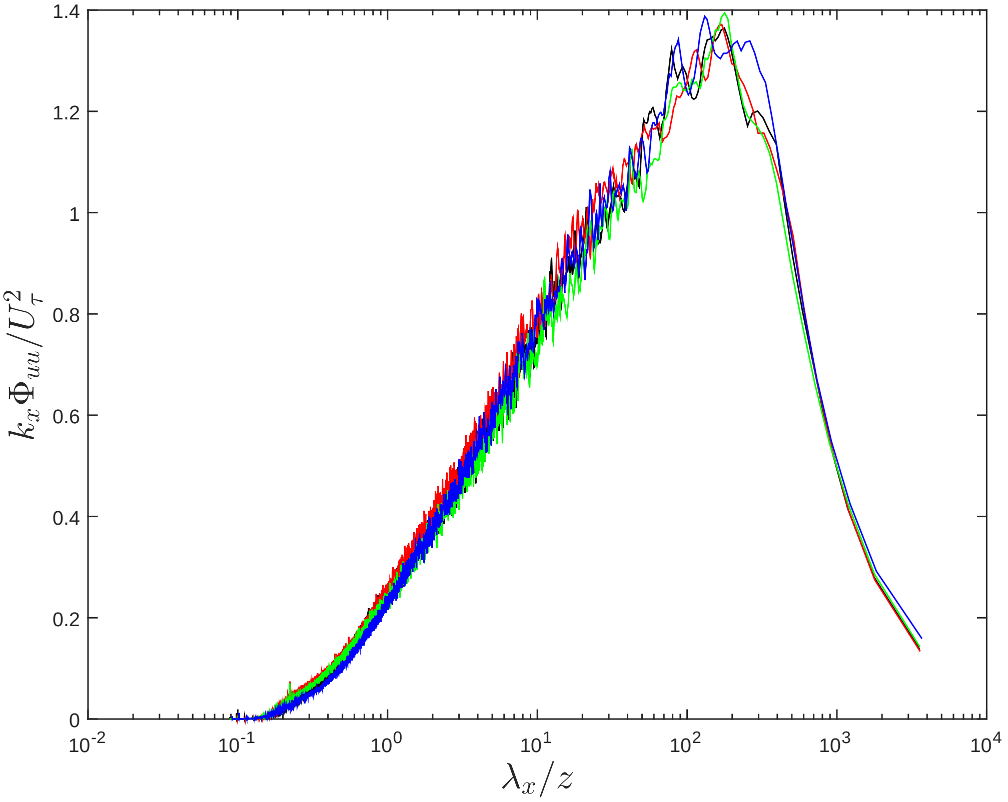

FIGURE 3.4: 1-D spectra obtained from HW1, HW2, HW3 and HW4 that are stationed at different spanwise locations for $Re_\tau \approx 26000$ case.

of $\sim 5\%$ (refer to figure 3.4). Therefore, for in-boundary layer calibration, the inclusion of higher order moments in the calibration equations (Breuer, 1995) were deemed not necessary. Also, it is to be noted that no temperature corrections were performed as the maximum variations in temperature during the calibration, and also between the pre- and post-calibrations, were within 1.5°C (refer to Samie (2017)).

Chapter 4

Calculation of 2-D spectra: corrections and validation

This chapter presents the results of Chandran, D., Baidya, R., Monty, J. P. & Marusic, I. 2016 Measurement of two-dimensional energy spectra in a turbulent boundary layer. In *Proceedings of the 20th Australasian Fluid Mechanics Conference*, Perth, Australia.

In this chapter, we present an experimental technique using hot-wire anemometry to measure the two-dimensional (2-D) energy spectra of the streamwise velocity component (u). The measurements are carried out in a turbulent boundary layer at friction Reynolds numbers of 2430 and 4210 and are validated against the 2-D spectra obtained from the direct numerical simulation (DNS) of Sillero *et al.* (2014) at matched Reynolds numbers. Based on these comparisons, a correction is introduced to account for the spatial resolution associated with the initial separation of the hot-wires. These findings establish the proposed technique for high Reynolds number flows in future works.

4.1 Introduction

As discussed in the introduction, the suitability of 1-D spectrum as a tool to observe self-similarity is debated due to aliasing. The work of Davidson *et al.* (2006) suggested that aliasing could contaminate the 1-D streamwise spectra by artificially shifting the energy to lower wavenumbers. However, a direct measurement of 2-D spectrum avoids the aliasing problem in the homogeneous directions (refer §2.2.3). A 2-D spectrum details the contribution of both the streamwise and spanwise length scales to the total turbulent intensity. On the other hand, a 1-D spectrum only provides the energy contribution by a particular streamwise length scale, λ_x, and does not inform us of the range of λ_y associated with that particular λ_x.

On the basis of the attached eddy hypothesis, the existence of geometrically self-similar eddies (whose lengths scale with z) suggest a region of constant energy in the 2-D spectrum at high Reynolds numbers to be bounded by a linear relationship, $\lambda_y \sim \lambda_x$. However, to discern such a behaviour, 2-D spectra at high Reynolds numbers need to be examined. As a first step towards high Reynolds number results, this chapter is concerned with establishing a reliable experimental technique to measure 2-D spectra of u. Validation of the experimental results with required corrections to obtain a well resolved 2-D spectra is described in the following sections.

4.2 Experimental Setup

The experiments are conducted in the open return turbulent boundary layer wind tunnel at The University of Melbourne (see §3.1 for details of the facility). The experiments are all conducted at a streamwise location of $x = 3.8$ m, further details are provided in table 4.1. Here, the boundary layer thickness (δ) is defined by fitting the velocity profile to the composite profile of Chauhan *et al.* (2009).

Facility	Re_τ	U_∞ (m/s)	δ (m)	U_τ (m/s)	z^+	l^+	TU_∞/δ ($\times 10^3$)
Low-*Re*	2430	15	0.069	0.545	**116**	17	26
Low-*Re*	2430	15	0.069	0.545	200	17	26
Low-*Re*	4210	25	0.076	0.86	200	27	39

TABLE 4.1: Details of experimental data; the values highlighted in bold indicate $z^+ = 2.6Re_\tau^{1/2}$.

Further, the friction velocity, U_τ, is obtained by a Clauser chart method using the log law constants, $\kappa = 0.4$ and A= 5.

The tailored experimental technique uses two single-wire hot-wire probes: HW1 and HW2 (as shown in figure 4.1). The details of the hot-wire anemometry, calibration of hot-wires and data acquisition are provided in chapter 3. The hot-wires are sampled at 30kHz for $T = 120$ seconds corresponding to about 26000 and 39000 boundary layer turnover times (TU_∞/δ) for $Re_\tau = 2430$ and 4210 respectively.

At the start of the measurement, HW1 and HW2 are positioned close to each other, at a fixed wall-normal location, as shown in figure 4.1. $dy_{initial}$ corresponds to the initial centre to centre spacing between the hot-wire sensors. For the present measurements, both HW1 and HW2 are sampled simultaneously, with HW1 at a fixed position, while HW2 is traversed in the spanwise direction up to a final spacing of $\Delta y \sim 2.8\delta$ (see figure 4.1). To acquire spatial information at smaller spanwise distances the spanwise traversing mechanism of HW2 is traversed on a logarithmic scale.

4.3 Calculation of 2-D spectra

The first step in the calculation of 2-D spectra from experiments, is to compute the two-point correlation in x-y plane. The streamwise velocity fluctuations, u_1 and u_2, acquired simultaneously using HW1 and HW2 respectively (for different spanwise spacings (Δy)) are used to construct the 2-D correlation. To this end, HW2 is physically traversed in the spanwise direction, while fixing HW1, to construct the

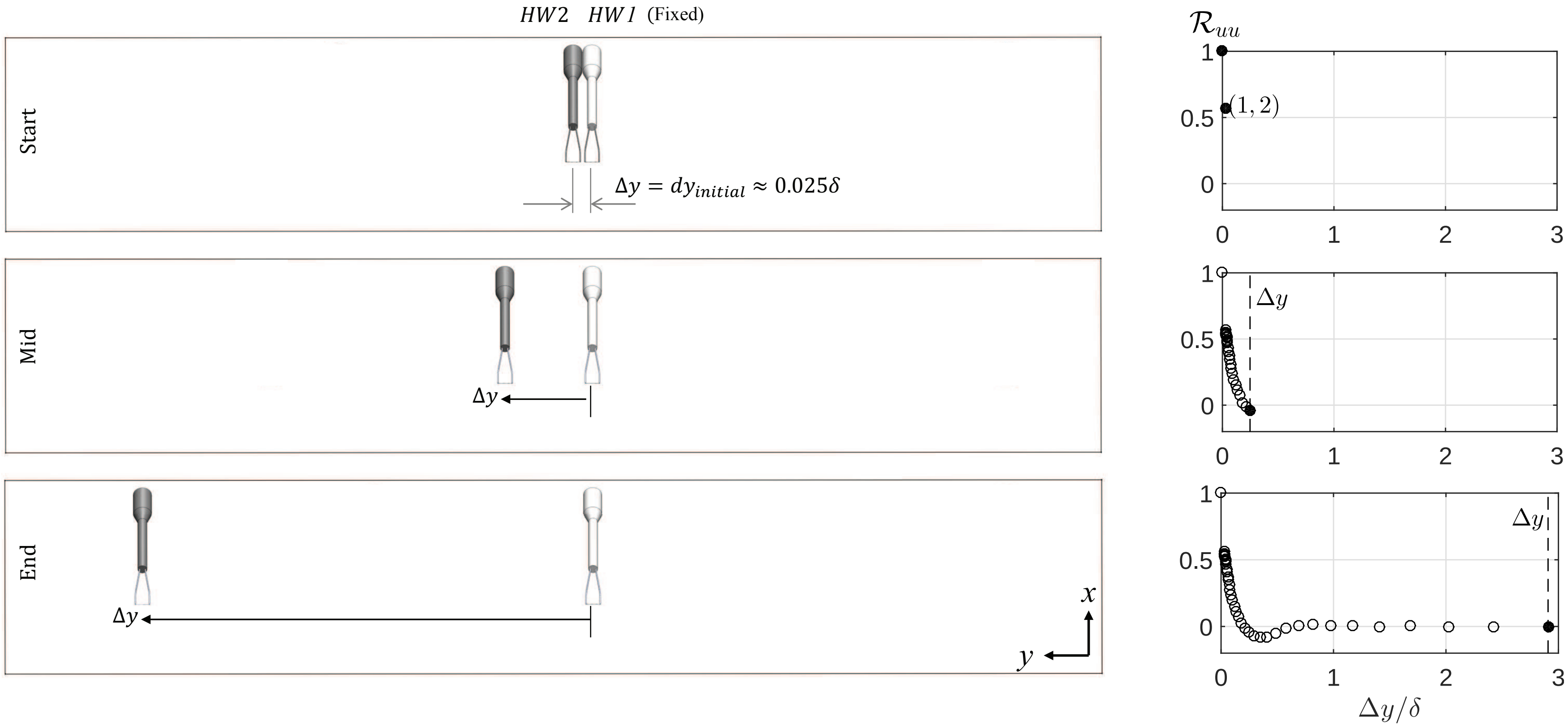

FIGURE 4.1: Schematic of experimental set-up with two hot-wire probes - HW1 and HW2 in the low-*Re* facility and normalized two-point correlation as a function of spanwise separation.

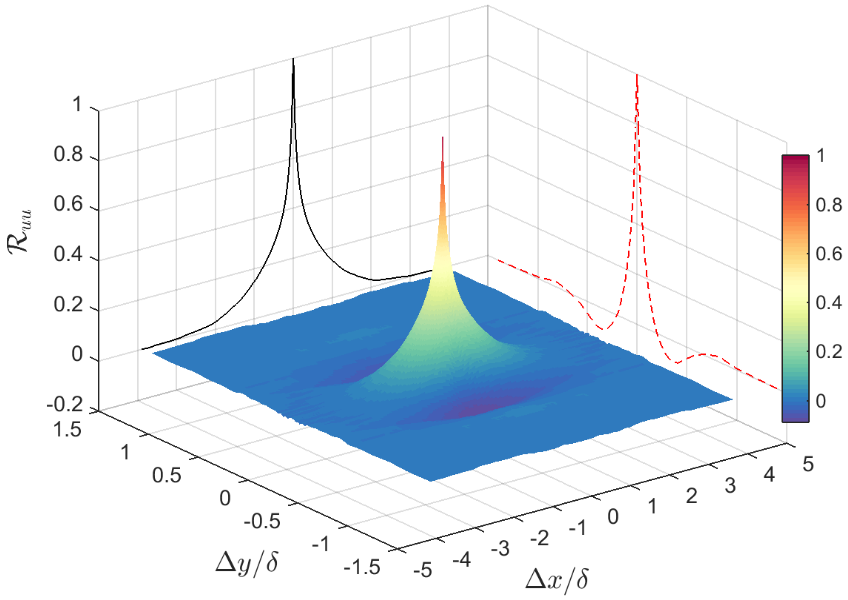

FIGURE 4.2: Normalized 2-D correlation constructed from the velocity time series with projections of 1-D correlations at $\Delta x = 0$ and $\Delta y = 0$

correlation as a function of Δy. Figure 4.1 schematically shows the arrangement of hot wires for three sets of spanwise locations and the corresponding calculations of the spanwise correlation R_{uu} as a function of Δy. The present setup allowed to compute correlation at $\Delta y = 0$ and for $dy_{initial} \leq \Delta y \leq 2.8\delta$. After computing the spanwise correlation, Taylor's frozen turbulence hypothesis allows the conversion of temporal information of the hot-wires into spatial information and hence enables the construction of correlation functions at different streamwise spacings (Δx). To this end, the convection velocity is assumed to be the mean velocity at that wall-height. We note, since the hot-wires (HW1 and HW2) are stationed at the same wall-normal location, spanwise homogeneity within the turbulent boundary layer can be assumed. As a consequence, the entire spanwise-streamwise correlation can be constructed from a series of independent two-point measurements conducted at different Δy. Hence, a 2-D correlation can be constructed by cross-correlating the streamwise velocity time series acquired using HW1 and HW2 by computing,

$$R_{uu}(\Delta x, \Delta y) = \overline{u_1(x, y)u_2(x + \Delta x, y + \Delta y)}. \tag{4.1}$$

Figure 4.2 shows the 2-D correlation obtained along with the projections of 1-D correlations. The black and red contours correspond to the 1-D streamwise and spanwise correlations respectively at $\Delta x = 0$ and $\Delta y = 0$. Here, R_{uu} is normalized using the variance of the velocity time series to get $\mathcal{R}_{uu}$.

Here, we note that while Taylor's hypothesis is reported to perform well in the outer region for $\lambda_x < 6\delta$ (Dennis & Nickels, 2008), uncertainties in the measured spectra are observed for larger scales due to an assumption of a constant convection velocity (del Álamo & Jiménez, 2009, Monty & Chong, 2009). Recent very large field of view PIV measurements (de Silva *et al.*, 2015) suggest that in the log region, the good agreement between the pre-multiplied spectra from hot-wire and PIV, extend to $\sim 15\delta$ in the streamwise direction. Additionally, Renard & Deck (2015) reports that, in comparison to a constant convection velocity (equal to the mean velocity) assumption, the effect of scale-dependent convection velocity is most significant near the wall with only subtle differences in the outer-region. Hence, here we anticipate the effects of Taylor's frozen turbulence hypothesis to be minimal, and do not affect any of the conclusions in this study.

4.3.1 Computing 2-D spectrum from the 2-D correlation

A uniformly spaced grid is a prerequisite for Fourier transformation. The computed 2-D correlation is uniformly spaced in the streamwise direction, but has a logarithmic spacing in the spanwise direction. Apart from this, the correlation is not resolved below $\Delta y = dy_{initial}$. Hence, there is a gap between $\Delta y = 0$ and $dy_{initial}$. Therefore, before performing Fourier transformation, the correlation is interpolated to a uniform spanwise spacing. While considering various interpolation schemes, it was observed that the linear interpolation scheme performed better. The other interpolation schemes were found to be more susceptible to noise present in the experimental data.

The 2-D energy spectrum of streamwise velocity fluctuations is obtained by taking a two dimensional Fourier transform of the calculated 2-D correlation $R_{uu}(\Delta x, \Delta y)$,

$$\phi_{uu}(k_x, k_y) = \int\int_{-\infty}^{\infty} R_{uu}(\Delta x, \Delta y) e^{-j2\pi(k_x \Delta x + k_y \Delta y)} \mathrm{d}(\Delta x)\mathrm{d}(\Delta y). \tag{4.2}$$

Here j is a unit imaginary number. In this way, the correlation in a 2-D physical space is transformed into energy spectrum (ϕ_{uu}) in a 2-D wavenumber space. Results for $\phi_{uu}(k_x, k_y)$ are presented as a function of λ_x and λ_y as shown in figure 4.3(a). Figure 4.3(a) is obtained by taking Fourier transform of the 2-D correlation shown in figure 4.2 at $Re_\tau \approx 2400$. It is to be noted that a few steps are adopted to filter the raw 2-D spectrum in order to improve the signal-to-noise ratio. These involve corrections to R_{uu} at large Δx and small Δy, interpolation of the 2-D spectrum to a logarithmic-spaced grid (coarser towards larger wavelengths) and further use of median and Savitzky-Golay filters. These steps are performed on all the measured low- and high-Reynolds number data and the details are provided in Appendix A.

If we consider λ_x and λ_y as a measure of the 'length' and 'width' (respectively) of the eddies in the flow, the 2-D spectrum can be considered as the energy contribution of different aspect ratio eddies. In other words, for a particular streamwise wavelength λ_x, a 2-D spectrum provides details of the range of spanwise length scales λ_y, at that particular λ_x.

The 1-D streamwise spectrum is obtained by integrating the 2-D spectrum across all the spanwise length scales (λ_y) and similarly, 1-D spanwise spectrum is obtained by integrating across all the streamwise length scales (λ_x), as given by,

$$\frac{k_x \phi_{uu}(k_x)}{U_\tau^2} = \int_0^\infty \frac{k_x k_y \phi_{uu}(k_x, k_y)}{U_\tau^2} \, \mathrm{d}\left(\ln \lambda_y\right) \tag{4.3a}$$

$$\frac{k_y \phi_{uu}(k_y)}{U_\tau^2} = \int_0^\infty \frac{k_x k_y \phi_{uu}(k_x, k_y)}{U_\tau^2} \, \mathrm{d}\left(\ln \lambda_x\right). \tag{4.3b}$$

Hence, say for a 1-D streamwise spectrum, the information on the range of λ_y at a particular λ_x is lost due to integration and which in turn attributes to aliasing

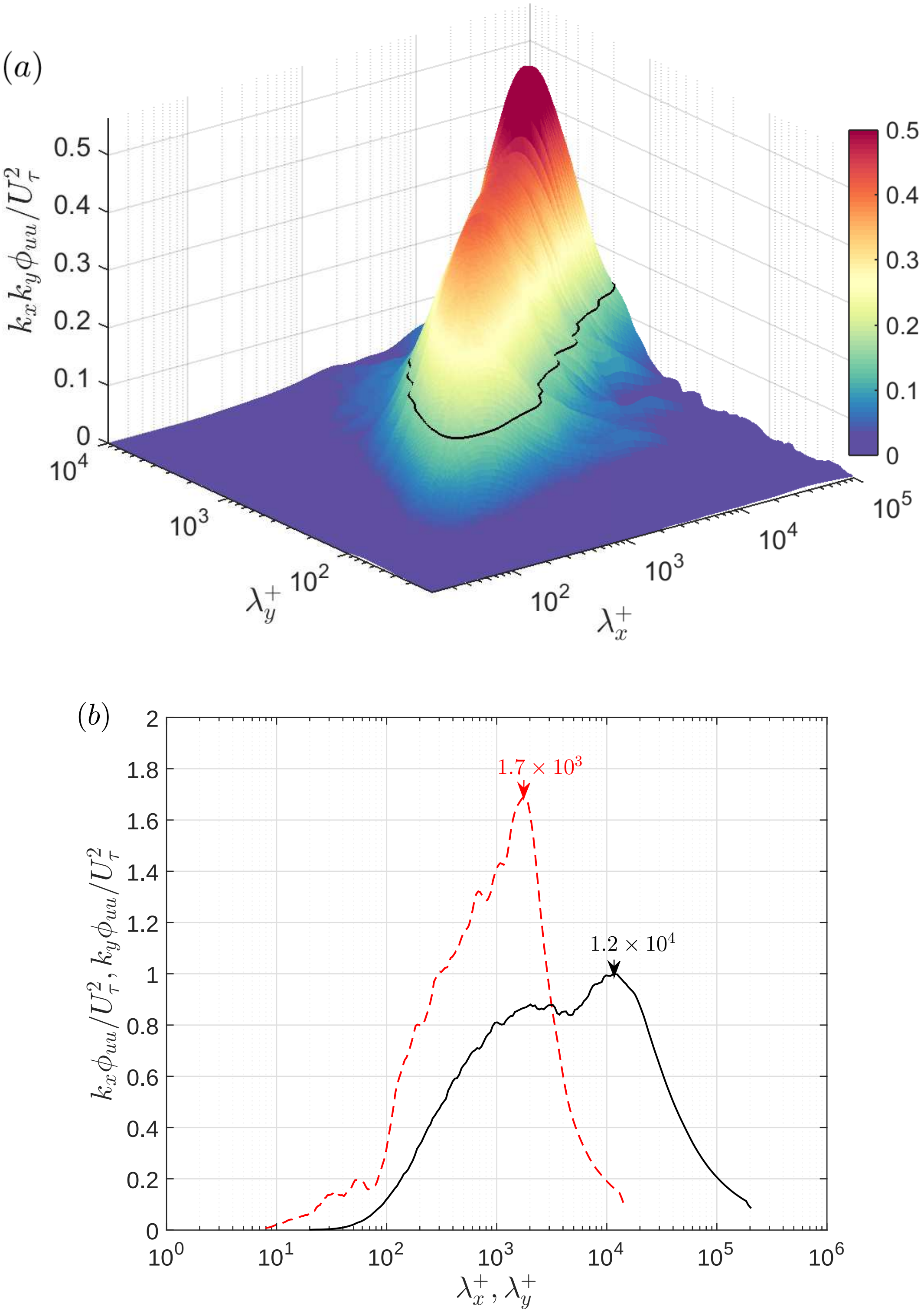

FIGURE 4.3: (a) 2-D spectrum at $Re_\tau \approx 2400$ obtained from the 2-D correlation shown in figure 4.2; the black line contour represents a constant energy of $k_x k_y \phi_{uu}/U_\tau^2 = 0.15$ and (b) 1-D streamwise (—) and 1-D spanwise (- - -) spectra obtained by integrating the 2-D spectrum.

errors (Tennekes & Lumley, 1972). This is the primary reason why a 2-D spectrum is devoid of aliasing error in the homogeneous plane.

Figure 4.3(b) shows the 1-D streamwise and spanwise spectra of u obtained after integrating the 2-D spectrum (shown in figure 4.3(a)) across λ_y and λ_x respectively, following equation 4.3. It is to be noted that the areas under the 1-D streamwise and 1-D spanwise spectra are the same and are equivalent to the variance ($\overline{u^2}$) of the streamwise velocity at that wall-normal location, as given by,

$$\overline{u^2}^+ = \int_0^\infty \int_0^\infty \frac{k_x k_y \phi_{uu}}{U_\tau^2} \mathrm{d}(\ln \lambda_x)\mathrm{d}(\ln \lambda_y). \tag{4.4}$$

4.4 Comparison with DNS at low-*Re*

The results obtained from the experiments at $Re_\tau \approx 2400$ (≈ 2000 based on δ_{99}) are compared against the DNS of ZPG boundary layer data of Sillero *et al.* (2014) to validate the novel experimental technique before moving to high Reynolds numbers. To this end, a two-dimensional Fourier transformation is carried out on the 2-D correlation obtained from the DNS database. Figure 4.4 shows a comparison between a contour of constant energy from the 2-D spectra (as highlighted in figure 4.3(a)), at $k_x k_y \phi_{uu}/U_\tau^2 = 0.15$, from both experiments and DNS. An energy level of $k_x k_y \phi_{uu}/U_\tau^2 = 0.15$ is chosen here for the comparison as it roughly corresponds to one-third of the maximum energy and therefore includes the contribution from a broad range of streamwise and spanwise length scales (refer to figure 4.3(a)). The results show good agreement between the experimental ($\cdots$) and DNS (—) results at $z^+ \approx 200$ (figure 4.4b), however, closer to the wall ($z^+ \approx 100$) a larger disagreement in the small scale region is present (figure 4.4a). This discrepancy is likely to be caused by insufficient spatial resolution of the experiments due to the initial spacing ($dy_{initial}$) between the hot-wires (see figure 4.1). Note that this spatial resolution issue is only due to the initial spacing between the hot-wires ($dy^+_{initial}$) and not to the sensor size (l^+). From figure 4.1, the smallest spanwise length scale that can be resolved by this arrangement of hot-wires is limited to

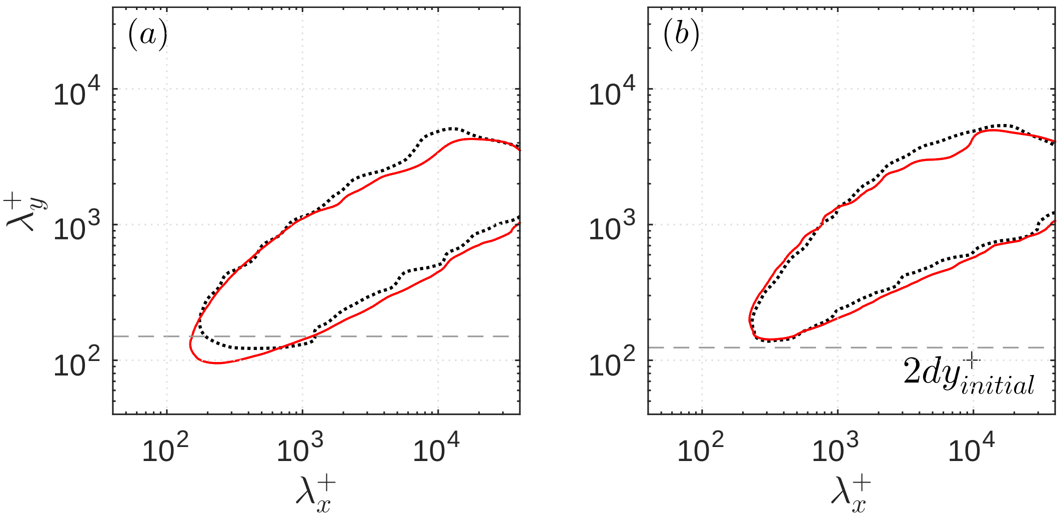

FIGURE 4.4: Comparison of experimental and DNS results for $k_x k_y \phi_{uu}/U_\tau^2 = 0.15$ at $Re_\tau \approx 2400$ and, (a) $z^+ \approx 100$ and (b) $z^+ \approx 200$; where, ······ raw experiment and —— DNS

$2dy_{initial}$. Therefore, all the points between $\Delta y = 0$ and $\Delta y = dy_{initial}$ in the spanwise correlation map are obtained by linear interpolation. Hence, the wavelength corresponding to a spanwise spacing of $dy^+_{initial}$ acts as a cut-off wavelength (dashed line in figure 4.4) and all the smaller scales (below the dashed line) are directly impacted by the interpolation scheme. We note that this discrepancy is more significant closer to the wall as there is more contribution from scales smaller than the cut-off wavelength (at $z^+ \approx 100$). Further, the area under the 2-D spectrum has to be equal to the variance at that wall-normal location, therefore, any unresolved energy at smaller scales will be redistributed across larger scales. Hence, to minimize such a scenario, ideally $dy^+_{initial}$ should be sufficiently small so that the smallest scales are well resolved. However, for the present experimental technique, it is not physically possible to reduce $dy^+_{initial}$ below a limit where the two hot-wires come in contact with each other.

4.4.1 Possibility of overlapping hot-wires

The prospect of overlapping hot-wires in order to resolve the scales smaller than $2dy^+_{initial}$ was considered. This would result in a separation in the wall-normal direction, Δz, between the hot-wires. To understand how Δz affects the energy spectra, the DNS data of channel flow (del Álamo *et al.* (2004)) corresponding to $Re_\tau = 950$ is used (the particular DNS dataset is used due to the availability of sufficient velocity fields, required for a reasonably converged 2-D spectrum). The 2-D spectrum and the associated 1-D spectra are calculated by correlating streamwise velocity fluctuations from different wall parallel planes, separated in the wall-normal direction by Δz. For the measurements at $z^+ = 100$, the effect of different values of $\Delta z^+ = 10$, 20 and 50 are shown in figure 4.5, and the results are compared against the base case when there is no wall-normal separation ($\Delta z^+ = 0$). It could be observed that the information of smaller scales are lost with increasing Δz. Therefore, the option of overlapping hot-wires to better resolve the small scales is worthwhile only if $\Delta z^+ < 10$. At $Re_\tau = 26000$, $\Delta z^+ = 10$ would correspond to a physical separation of $\Delta z = 0.13$mm. Due to the size of the

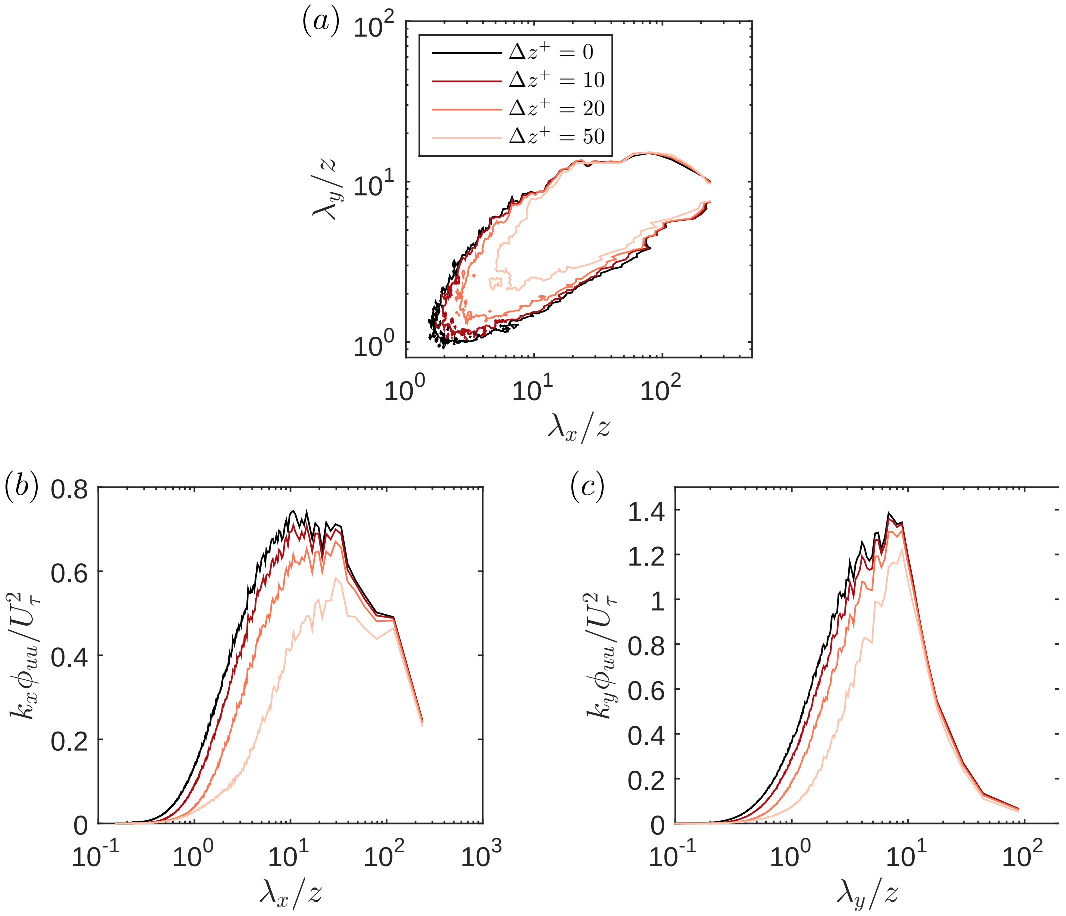

FIGURE 4.5: Simulating the effect of overlapping the closest hot-wires using DNS of channel flow at $Re_\tau = 934$ (del Álamo *et al.*, 2004) for different values of Δz^+: (a) 2-D spectra, (b) 1-D streamwise spectra and (c) 1-D spanwise spectra.

prongs of the hot-wire, such a small separation is not feasible practically. Baars *et al.* (2016) reports from their two-point measurements in the HRNBLWT that the minimum wall-normal separation possible between a pair of Dantec 55P15 probes is about 2.2 mm. Therefore, we resort to a correction scheme based on DNS to account for the spatial resolution issue associated with the initial spacing between the hot-wires.

4.5 Initial spacing correction

A method is adopted based on the DNS data available, to correct for the spatial resolution issue associated with $dy^+_{initial}$. Figure 4.6 shows the 1-D correlation in the spanwise direction obtained using DNS data, which is interpolated to match the experimental resolution. Here, the data points corresponding to a spanwise length of $0 < \Delta y^+ \leq dy^+_{initial}$ are initially omitted from the original correlation

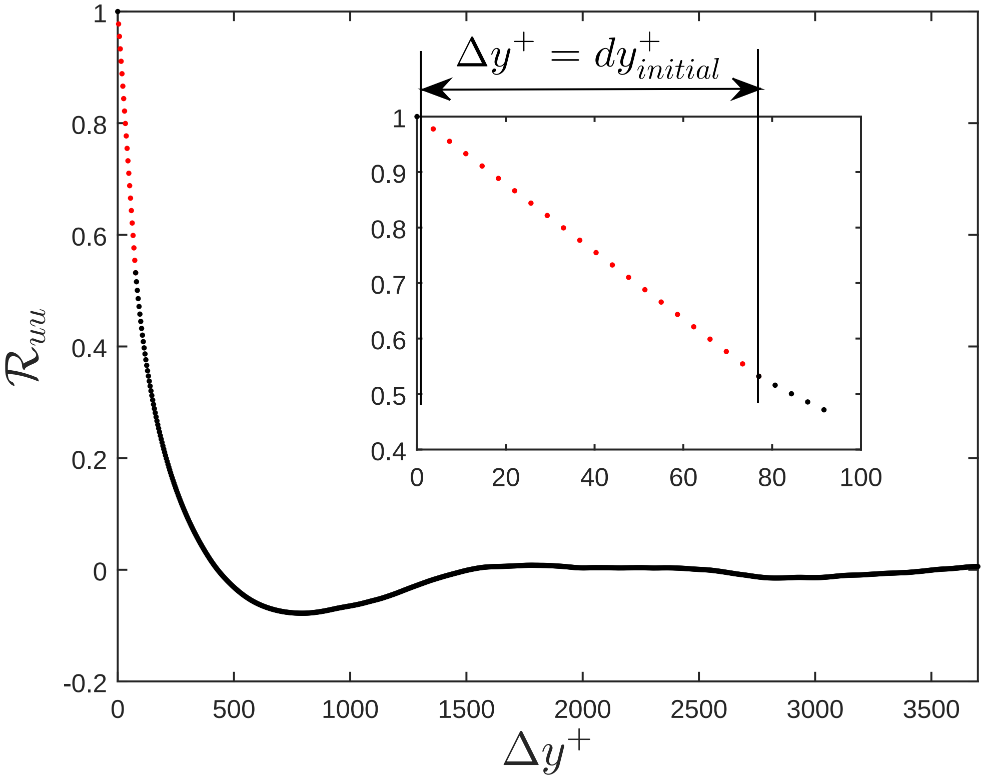

FIGURE 4.6: 1-D spanwise correlation demonstrating the method of correcting $dy^+_{initial}$ error.

and then recomputed using a linear interpolation scheme (red symbols in figure 4.6) to match the experimental conditions.

The computed 2-D spectra from the original and interpolated DNS correlation functions are shown in figures 4.7(a) and 4.7(b) respectively. The difference ($\Delta k_x k_y \phi^+_{uu}$) of the two spectra is computed and shown in figure 4.7(c). This difference corresponds to the amount of energy redistributed due to $dy^+_{initial}$. The 2-D spectra calculated from experiments is now corrected by adding this difference to it. Namely,

$$\Delta k_x k_y \phi^+_{uu} = \left[\frac{k_x k_y \phi_{uu}}{U_\tau^2}\right]_{DNS,o} - \left[\frac{k_x k_y \phi_{uu}}{U_\tau^2}\right]_{DNS,i} \tag{4.5}$$

$$\left[\frac{k_x k_y \phi_{uu}}{U_\tau^2}\right]_{EXP,c} = \left[\frac{k_x k_y \phi_{uu}}{U_\tau^2}\right]_{EXP} + \Delta k_x k_y \phi^+_{uu}. \tag{4.6}$$

where the subscripts $_{DNS,o}$ and $_{DNS,i}$ represent original and interpolated DNS results respectively. Similarly, subscripts $_{EXP,c}$ and $_{EXP}$ represent the corrected and uncorrected experimental results respectively. As one would expect, the difference is largest near λ^+_y corresponding to $dy^+_{initial}$ (see white dashed line in figure 4.7).

A contour of constant energy in the corrected experimental spectrum (—) is compared against the DNS(—) as shown in figure 4.8. A good agreement with DNS is observed at smaller scales where the uncorrected experimental spectrum ($\cdots$) shows a mismatch.

4.5.1 Relevance to High Reynolds number Measurements

The correction method discussed is highly relevant for measurements at high Reynolds number as the smallest scales are typically even more harder to resolve. Consequently, one would require even smaller spacing between the hot-wires to maintain a fixed spacing in viscous units. Hutchins *et al.* (2009) has shown that at smaller scales, the energy contribution shows minimal variance with increasing Reynolds numbers. Equipped with this knowledge, the proposed correction scheme should be applicable at high Reynolds numbers as well. To illustrate this,

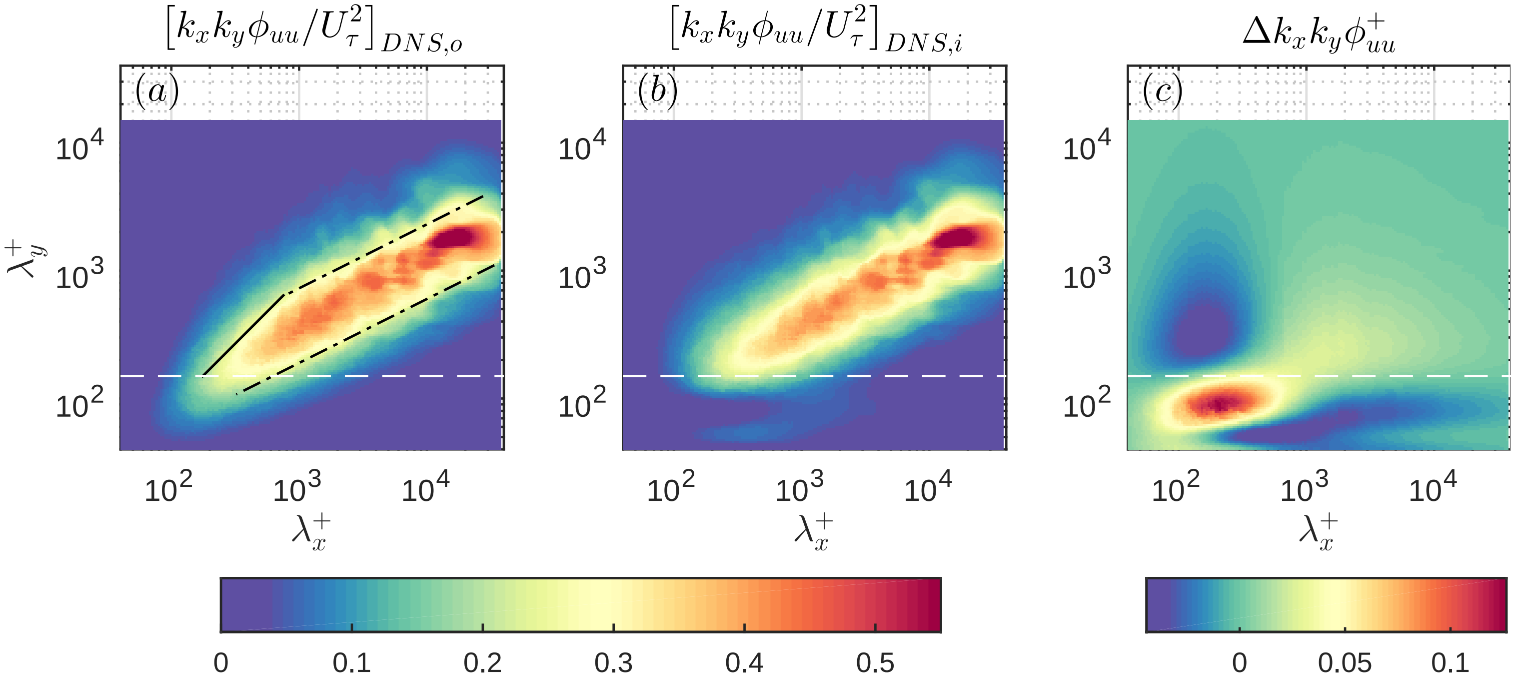

FIGURE 4.7: (a) 2-D spectrum obtained from the original DNS correlation, where —— and -·- represent the relationships $\lambda_y/z \sim \lambda_x/z$ and $\lambda_y/z \sim (\lambda_x/z)^{1/2}$ respectively as reported by del Álamo *et al.* (2004), (b) 2-D spectrum obtained from the interpolated DNS correlation and (c) difference between (a) and (b).

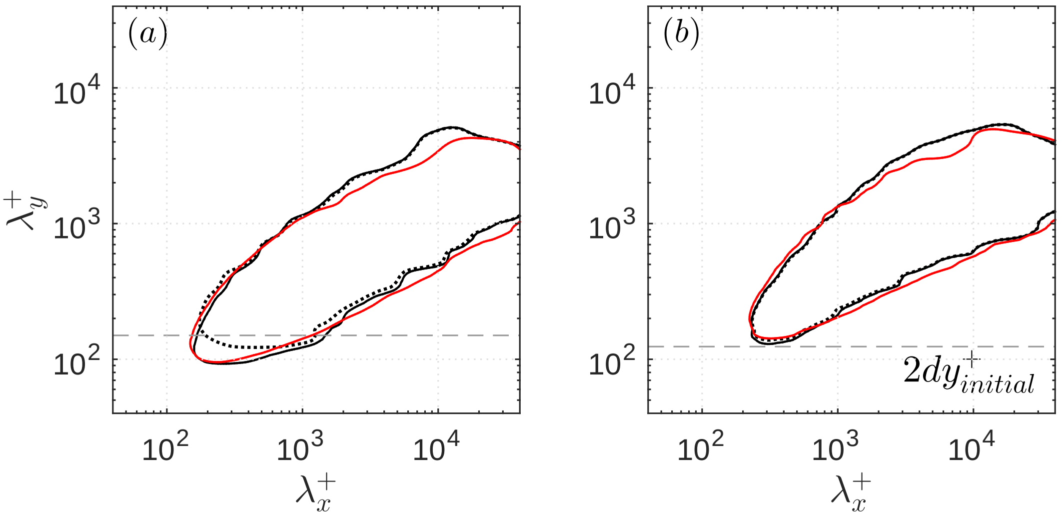

FIGURE 4.8: Comparison of experimental and DNS results for $k_x k_y \phi_{uu}/U_\tau^2 = 0.15$ at $Re_\tau \approx 2400$ and, (a) $z^+ \approx 100$ and (b) $z^+ \approx 200$; where, ······ uncorrected experiment; —— corrected experiment and —— DNS

the DNS data obtained at $Re_\tau \approx 2000$ is used to correct the experimental data obtained at $Re_\tau \approx 4200$ at matched z^+. The results are given in figure 4.9 which show good agreement at the smaller scales between the uncorrected experimental and interpolated DNS spectrum (figure 4.9a). Furthermore, after the correction, the small scales now agree with the original DNS 2-D spectrum (figure 4.9b). The agreement is only expected at smaller scales since we are comparing two different

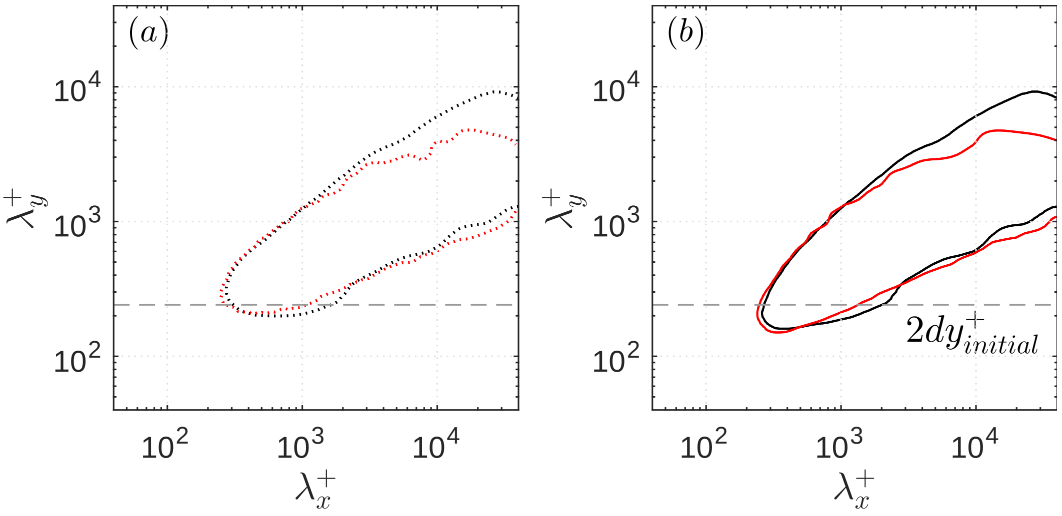

FIGURE 4.9: Comparison of experimental ($Re_\tau \approx 4200$) and DNS ($Re_\tau \approx 2000$) results at $k_x k_y \phi_{uu}/U_\tau^2 = 0.15$, (a) before correction where, ······ uncorrected experiment $[k_x k_y \phi_{uu}/U_\tau^2]_{EXP}$ and ······ interpolated DNS $[k_x k_y \phi_{uu}/U_\tau^2]_{DNS,i}$ and (b) after correction where, —— corrected experiment $[k_x k_y \phi_{uu}/U_\tau^2]_{EXP,c}$ and —— original DNS $[k_x k_y \phi_{uu}/U_\tau^2]_{DNS,o}$.

Reynolds numbers. Therefore, the proposed correction enables one to compare the 2-D spectra across multiple Reynolds numbers and wall heights, while still maintaining a practical $dy_{initial}$.

4.6 Chapter summary

In this chapter, we have introduced the experimental technique to measure the 2-D energy spectra of the streamwise velocity in a turbulent boundary layer. The technique involves the use of a pair of hot-wire sensors that are sampled simultaneously for different spanwise spacings. A description of how to construct a 2-D correlation, as a function of streamwise and spanwise distance, from the velocity time series is presented. This procedure is then used to compute the 2-D spectra, as a function of streamwise and spanwise wavelengths. Results are validated against the statistics computed from DNS databases at matched Reynolds numbers. This comparison revealed the importance of the initial spacing between the hot-wires and its detrimental impact on resolving the small scale region of the 2-D spectra. To account for this, a correction scheme is outlined based on results computed from DNS databases. Collectively, the proposed experimental technique and correction schemes lay the foundation for measurements at higher Reynolds numbers, which is detailed in the next chapter.

Chapter 5

Low- and high-Reynolds number 2-D spectra

This chapter incorporates the results of Chandran, D., Baidya, R., Monty, J. P. & Marusic, I. 2017 Two-dimensional energy spectra in high-Reynolds-number turbulent boundary layers. ***J. Fluid Mech.*****, 826, R1.**

In this chapter, we report the measurements of two-dimensional (2-D) spectra of the streamwise velocity (u) in a high Reynolds number turbulent boundary layer. After validating the novel experimental technique in chapter 4, experiments employing multiple hot-wire probes were carried out at friction Reynolds numbers ranging from 2400 to 26000. Taylor's frozen turbulence hypothesis is used to convert temporal-spanwise information into a 2-D spatial spectrum which shows the contribution of streamwise (λ_x) and spanwise (λ_y) length scales to the streamwise variance at a given wall height (z). At low Reynolds numbers, the shape of the 2-D spectra at a constant energy level shows $\lambda_y/z \sim (\lambda_x/z)^{1/2}$ behaviour at larger scales, which is in agreement with the existing literature at a matched Reynolds number obtained from direct numerical simulations. However, at high Reynolds numbers, it is observed that the square-root relationship tends towards a linear relationship ($\lambda_y \sim \lambda_x$) as required for self-similarity and predicted by the attached eddy hypothesis.

5.1 Introduction

As discussed in §2.2.3, Chung *et al.* (2015) argue that in order to have a k_x^{-1} behaviour in the 1-D spectrum, a region of constant energy in the 2-D spectrum should be bounded by $\lambda_y/z \sim f_1(\lambda_x/z)$ and $\lambda_y/z \sim f_2(\lambda_x/z)$ where f_1 and f_2 are identical power laws. Additionally, based on Townsend's (1976) attached eddy hypothesis, geometric self-similarity would require f_1 and f_2 to be linear relationships. However, these arguments are not yet tested due to the lack of 2-D energy spectra at high Reynolds numbers. At low Reynolds numbers ($Re_\tau \leq 1900$), del Álamo *et al.* (2004) showed that such a region of constant energy is bounded at larger scales by a square-root relationship of the form $\lambda_y/z \sim (\lambda_x/z)^{1/2}$. This square-root relation between the lengths and widths of the structures, is reported by the authors, to indicate a failure of self-similarity. However, it is noted that Townsend's arguments are only expected to strictly hold at high Reynolds number. Therefore, employing the experimental technique established in chapter 4, in this chapter, we present measurements of 2-D energy spectra over a range of Reynolds numbers, up to $Re_\tau \approx 26000$. The objective is to test the above arguments and to explore 2-D energy spectra as a tool to observe self-similarity.

5.2 Experiments

Two sets of experiments were conducted in zero-pressure-gradient boundary layers, in two separate facilities. The first, which we refer to as the low Reynolds number experiments, were conducted in an open return boundary layer wind tunnel (described in §3.1), and the high Reynolds number experiments were conducted in the HRNBLWT (described in §3.2). Details of the experiments are summarized in table 5.1. Here, the boundary layer thickness (δ) is defined by fitting the velocity

Facility	Re_τ	U_∞ (m/s)	δ (m)	U_τ (m/s)	z^+	z/δ	l^+	TU_∞/δ ($\times 10^3$)
Low-*Re*	2430	15	0.069	0.545	**116**	0.047	17	26
Low-*Re*	2430	15	0.069	0.545	150	0.062	17	26
Low-*Re*	2430	15	0.069	0.545	209	0.086	17	26
Low-*Re*	4210	25	0.076	0.86	**150**	0.036	27	39
Low-*Re*	4210	25	0.076	0.86	200	0.047	27	39
HRNBLWT	15100	20	0.37	0.64	150	0.01	20	19.5
HRNBLWT	15100	20	0.37	0.64	**320**	0.021	20	19.5
HRNBLWT	15100	20	0.37	0.64	1025	0.068	20	19.5
HRNBLWT	20250	30	0.35	0.92	150	0.007	29	20.6
HRNBLWT	20250	30	0.35	0.92	**376**	0.019	29	20.6
HRNBLWT	20250	30	0.35	0.92	425	0.021	29	20.6
HRNBLWT	20250	30	0.35	0.92	1365	0.067	29	20.6
HRNBLWT	26090	40	0.337	1.231	125	0.005	39	14.2
HRNBLWT	26090	40	0.337	1.231	**418**	0.016	39	14.2
HRNBLWT	26090	40	0.337	1.231	550	0.021	39	14.2
HRNBLWT	26090	40	0.337	1.231	1757	0.067	39	14.2

TABLE 5.1: Details of experimental data; the values highlighted in bold indicate $z^+ = 2.6Re_\tau^{1/2}$.

profile to the composite profile of Chauhan *et al.* (2009), while l, U_∞ and T denote the hot-wire sensor length, freestream velocity and total sampling duration. It is noted that for the highest Reynolds numbers measured, the value of l^+ are slightly higher than the established standard of $l^+ \lesssim 20$ that is adopted to minimize the hot-wire spatial resolution issues. However, they are not expected to affect the large-scales that are the focus of the present study (refer to Hutchins *et al.* (2009)) and therefore do not alter any of the conclusions from this study.

Measurements of 2-D u-spectra were achieved by employing a novel setup that uses two and four single-wire hot-wire probes for the low and high Reynolds number experiments respectively. Hot-wires were operated using an in-house Melbourne University Constant Temperature Anemometer (MUCTA) in all cases. The schematic of the experimental setup for the high Reynolds number measurements is shown in figure 5.1 (see §4.2 for details of the low Reynolds number experiment). The setup comprises four hot-wires: HW1, HW2, HW3 and HW4. All hot-wires are calibrated immediately before and after each measurement allowing compensation for

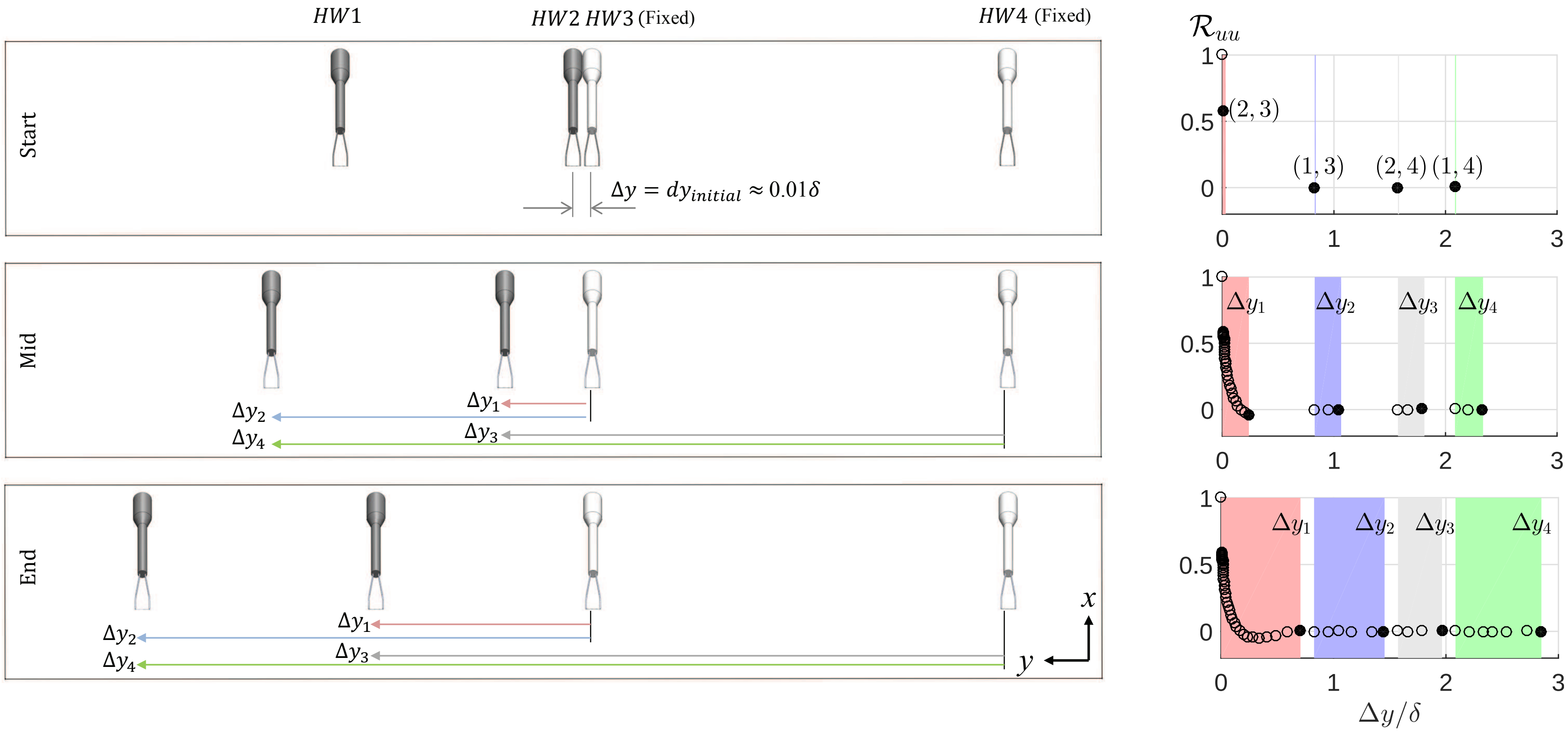

FIGURE 5.1: Schematic of experimental set-up with four hot-wire probes - HW1, HW2, HW3 and HW4 in the high Reynolds number boundary layer facility and normalized two-point correlation as a function of spanwise separation.

Δ_y	R_{uu}	Colour-code
$\Delta y_1(0.01\delta - 0.7\delta)$	$u_2 * u_3$	🔴
$\Delta y_2(0.7\delta - 1.4\delta)$	$u_1 * u_3$	🔵
$\Delta y_3(1.4\delta - 2\delta)$	$u_2 * u_4$	⚪
$\Delta y_4(2\delta - 2.7\delta)$	$u_1 * u_4$	🟢

TABLE 5.2: Details of constructing spanwise correlation at high-*Re*.

drift in the hot-wire voltage during the measurements. The calibration procedure adopted for all four hot-wires are detailed in §3.4.2.

Figure 5.1 schematically shows the arrangement of hot-wires, for the high Reynolds number case, for three sets of spanwise locations and the corresponding calculations of the spanwise correlation. In all cases, HW3 and HW4 are stationed at a fixed spanwise location, whereas HW1 and HW2 are traversed together in the spanwise direction (with logarithmic spacing). Hence the distance between hot-wire pairs, HW1 and HW2 is fixed at all times as is the distance between HW3 and HW4. At the start of the measurement, HW2 and HW3 are as close as practicable to each other with $dy_{initial} \approx 0.01\delta$ as the initial spacing between them. The correlation coefficient, R_{uu}, as a function of spanwise spacing (Δy) is obtained by cross-correlating the velocity time series obtained from a pair of hot-wires. Since four hot-wires are employed, each step movement of the traverse gives R_{uu} corresponding to four spanwise spacings: Δy_1, Δy_2, Δy_3 and Δy_4, which are shown as filled circles in figure 5.1. The figure is colour-coded (as represented in table 5.2) to show the correlation points obtained with a particular pair of hot-wires.

The spanwise traversing is carried out up to a maximum spacing of $\Delta y_{max} \approx 2.7\delta$. Therefore, the complete measurement (~ 40 discrete locations) captures R_{uu} for $\Delta y = 0$ and $0.01\delta < \Delta y < 2.7\delta$, as shown in figure 5.1. The use of Taylor's frozen turbulence hypothesis using the local mean velocity as the convection speed allows the construction of correlation functions at different streamwise spacings (Δx) as well (also refer to §4.3). Therefore, the complete 2-D, two-point correlation,

$$R_{uu}(\Delta x, \Delta y) = \overline{u(x, y)u(x + \Delta x, y + \Delta y)}, \tag{5.1}$$

can be calculated (overbar denotes ensemble time-average). A 2-D Fourier transformation of the computed 2-D correlation yields the 2-D spectrum of streamwise velocity fluctuations as a function of k_x and k_y,

$$\phi_{uu}(k_x, k_y) = \int\int_{-\infty}^{\infty} R_{uu}(\Delta x, \Delta y) e^{-j2\pi(k_x \Delta x + k_y \Delta y)} \mathrm{d}(\Delta x)\mathrm{d}(\Delta y), \tag{5.2}$$

where j is a unit imaginary number. Similar to the low-Reynolds number cases, the raw 2-D spectra measured at high Reynolds numbers are also filtered by following the steps discussed in Appendix A. Additionally, it is to be noted that, we have applied the DNS-based small-scale correction described in §4.5, to all the measured 2-D spectra discussed in this chapter.

5.3 Low- versus high-Reynolds number spectra

Figure 5.2(a) shows contours of the 2-D spectrum for the $Re_\tau \approx 2400$ case at $z^+ = 116\,(\approx 2.6Re_\tau^{1/2})$, corresponding to the start of the logarithmic region (Klewicki *et al.*, 2009). Here, the spectrum is scaled with U_τ^2 and wavelengths are scaled with z. The black line contours represent constant energy levels $k_x k_y \phi_{uu}/U_\tau^2 =$ 0.25, 0.35 and 0.45. A linear relationship of the form $\lambda_y/z \sim \lambda_x/z$ is observed only in the small scale region ($\lambda_x/z, \lambda_y/z < 10$), as marked by the blue solid line. At larger scales, a square-root relationship of the form $\lambda_y/z \sim (\lambda_x/z)^{1/2}$ is evident, as marked by the blue dashed line. These relationships are in agreement with the results of del Álamo *et al.* (2004) from their DNS of turbulent channel flow at a similar Reynolds number. If λ_x and λ_y characterize the length and width of turbulent structures respectively, such a square-root relationship suggests that the eddies in this scale range are growing longer but not as wide, meaning such eddies are not self-similar.

At high Reynolds number, however, there is a significant difference in the large-scale behaviour. Figure 5.2(b) shows the 2-D spectrum measured at $Re_\tau \approx$ 26000 and at $z^+ = 418\,(= 2.6Re_\tau^{1/2})$. Again, the black line contours represent $k_x k_y \phi_{uu}/U_\tau^2 = 0.25$, 0.35 and 0.45 and the blue solid and dashed lines denote the

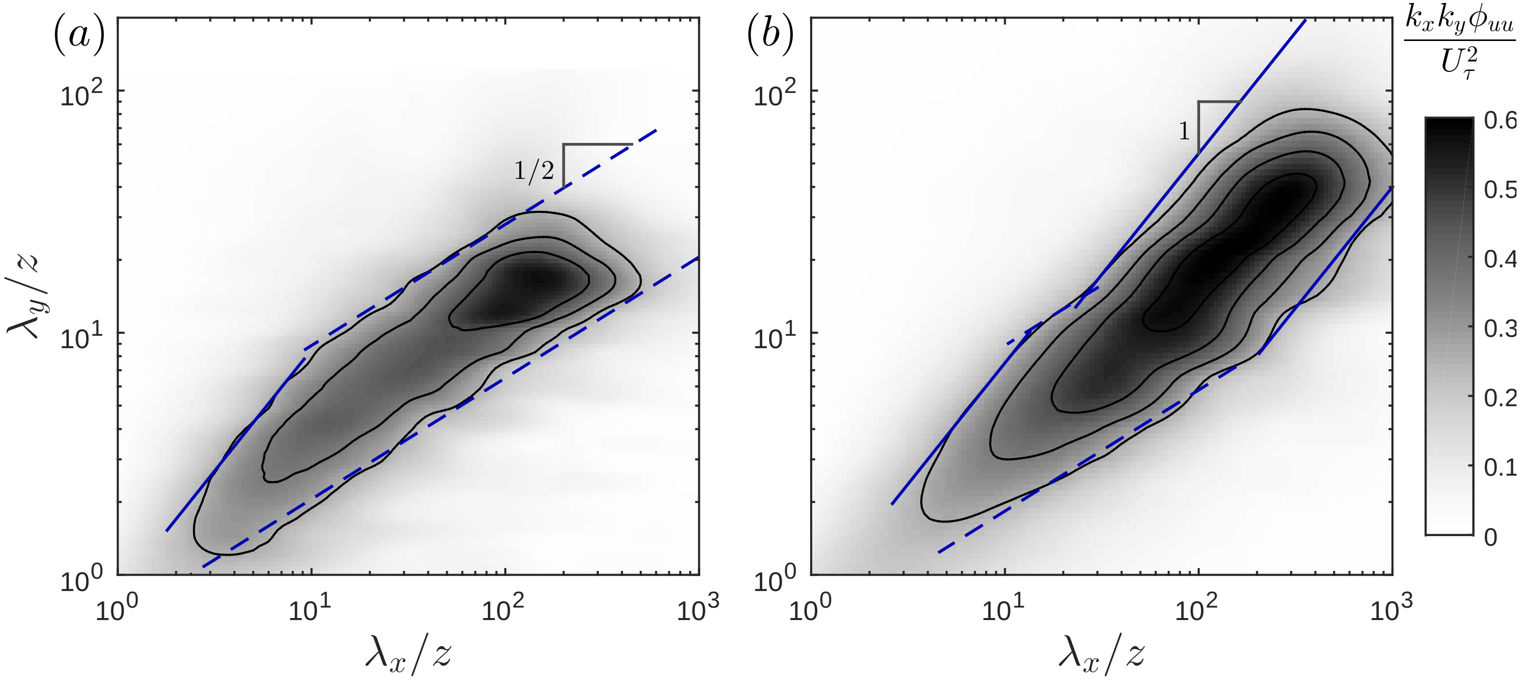

FIGURE 5.2: 2-D spectra at $z^+ = 2.6 {Re_\tau}^{1/2}$ for (a) $Re_\tau \approx 2400$ and (b) $Re_\tau \approx 26000$; the black line contours represent $k_x k_y \phi_{uu}/U_\tau^2 =$ 0.25, 0.35 and 0.45 and the blue solid and dashed lines denote the $\lambda_y/z \sim \lambda_x/z$ and $\lambda_y/z \sim (\lambda_x/z)^{1/2}$ relationships respectively.

$\lambda_y/z \sim \lambda_x/z$ and $\lambda_y/z \sim (\lambda_x/z)^{1/2}$ relationships respectively. The lower end of the large scale region behaves the same way as in the lower Reynolds number case; i.e, the square-root relationship remains. However, the larger scales deviate away from the square-root relationship and tend towards $\lambda_y/z \sim \lambda_x/z$. This linear relationship, as discussed in §5.1, is a necessary condition for self-similarity, which was notably absent for the low Reynolds number case. The length scales at which the peak energy deviates from the low Reynolds number behaviour are approximately $\lambda_x \sim 100z(\sim 1.5\delta)$ and $\lambda_y \sim 15z(\sim 0.2\delta)$. These values denote the minimum dimensions of the scales that are highly energetic and self-similar, and these are certainly large-scales, with an average aspect ratio of $\lambda_x/\lambda_y \approx 7$ at the energetic ridge of the spectrum. From an attached eddy perspective, the large aspect ratio observed is consistent with the existence of packets of eddies. Furthermore, the results suggest that the most energetic large-scale structures only become self-similar after maturing into such high aspect ratios.

5.4 2-D spectra: condition for self-similarity

To illustrate the expected qualitative 2-D spectrum from a field of self-similar eddies, here we will utilize the attached eddy model, where hierarchies of representative eddies which are aligned in the streamwise direction, such as those shown in figure 5.3(a), are used to model the logarithmic region (Perry *et al.*, 1986). In figure 5.3(a), for illustrative purposes, a discretized model with distinct hierarchies is shown. However, in the actual simulation, a continuous hierarchy is used with the heights of the smallest and the largest eddies being 100 viscous units and δ respectively. Further, the aspect ratio of the representative eddy is roughly the average aspect ratio of the large scales observed in the high Reynolds number results. Further details of the attached eddy model along with the procedure to compute the 2-D spectrum can be found in chapter 6.

Figure 5.3(b) shows the 2-D spectrum obtained from this idealized model at similar conditions to the high Reynolds number experiment: $Re_\tau \approx 26000$ and $z^+ =$

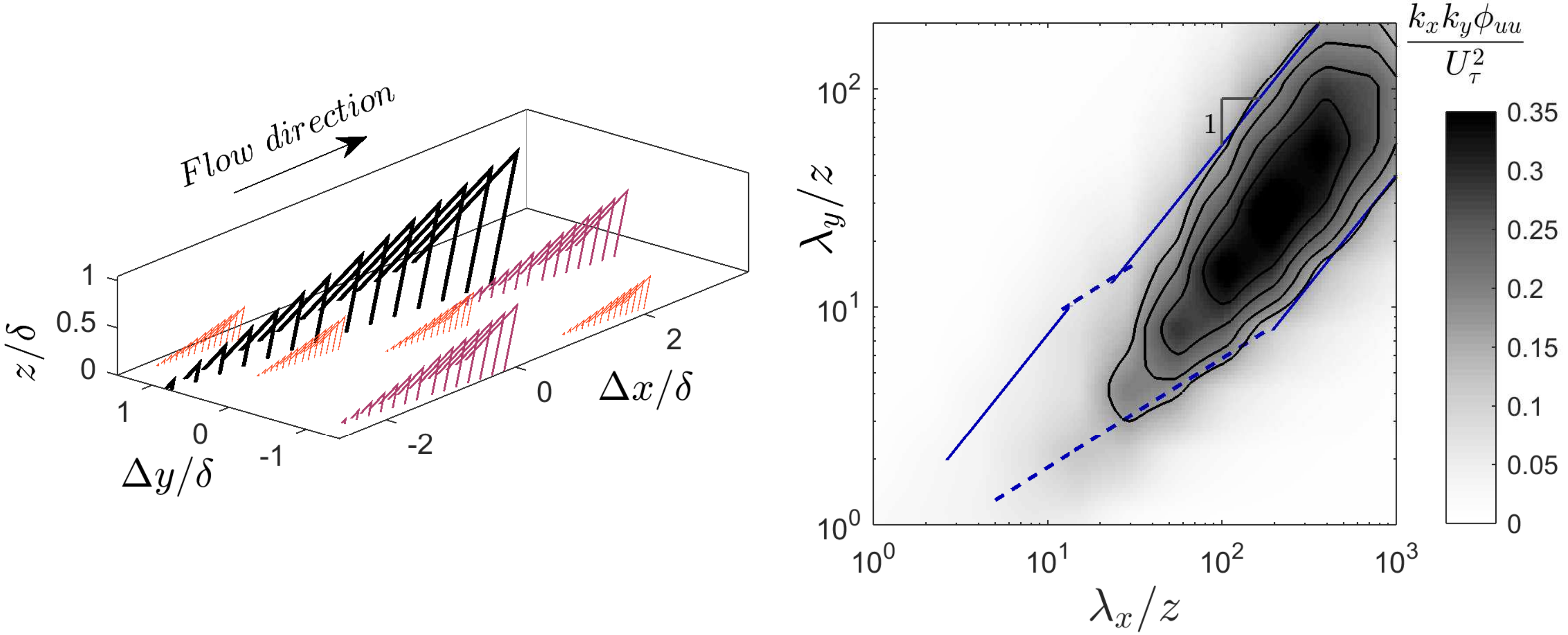

FIGURE 5.3: (a) Illustration of the attached eddy model showing three distinct hierarchies of self-similar packet-eddies with the size of the largest eddy (black) of the order of δ and (b) 2-D spectrum obtained from attached eddy model at $Re_\tau \approx 26000$ and $z^+ = 2.6{Re_\tau}^{1/2}$; blue lines correspond to the constant energy bounds shown in figure 5.2(b).

$2.6Re_\tau^{1/2}$. It was shown recently by Baidya *et al.* (2017) that asymptotic features such as a k_x^{-1} law are not necessarily observable at finite Reynolds numbers even when self-similarity is strictly enforced. Therefore, it is interesting to note that the contours of the 2-D spectrum at $Re_\tau \sim \mathcal{O}(10^4)$ shown in figure 5.3(b), follow a $\lambda_x \sim \lambda_y$ relation as predicted for the asymptotic state, while the corresponding 1-D spectra still do not exhibit a clear k^{-1} region (see figure 5.5e). Furthermore, the attached eddy results are not expected to follow the square-root relationship observed in experiments (blue dashed line in figure 5.3b) as the model comprises purely self-similar eddies.

5.5 A simplified model of 2-D spectra

Following the sketch of the organization of 2-D spectra at low Reynolds number by del Álamo *et al.* (2004), let us consider a simplified 2-D spectra model at high Reynolds number for the logarithmic region. The model is idealized by assuming 2-D spectra in the logarithmic region as a constant energy level bounded by the relationships mentioned in figure 5.2. The energy is assumed to be zero outside these bounds. In figure 5.4(a), the dark shaded patch represents such a region of constant energy for the low Reynolds number case. This is exactly the same as the region sketched in figure 3(c) of del Álamo *et al.* (2004). The overlaid light shaded patch is the constant energy level for the high Reynolds number case.

Following the experimental results, the large scale region of the high Reynolds number spectra (bounded by a-b-c-d) deviates from the low Reynolds number characteristics and tends towards a higher power law. This region will be referred to as the '*large eddy region*'. As described by Chung *et al.* (2015), the upper and lower limits of this region of constant energy are denoted by power laws of the form $\lambda_y/z = C_1 f_1(\lambda_x/z)$ and $\lambda_y/z = C_2 f_2(\lambda_x/z)$ respectively. Here (C_1, C_2) is the range of the width of eddies for a specified length. As the *large eddy region* is bounded by parallel lines, this range (C_1, C_2) is constant for all eddies of sizes within the *large eddy region*. Now, if the transition from a square-root relationship occurs at

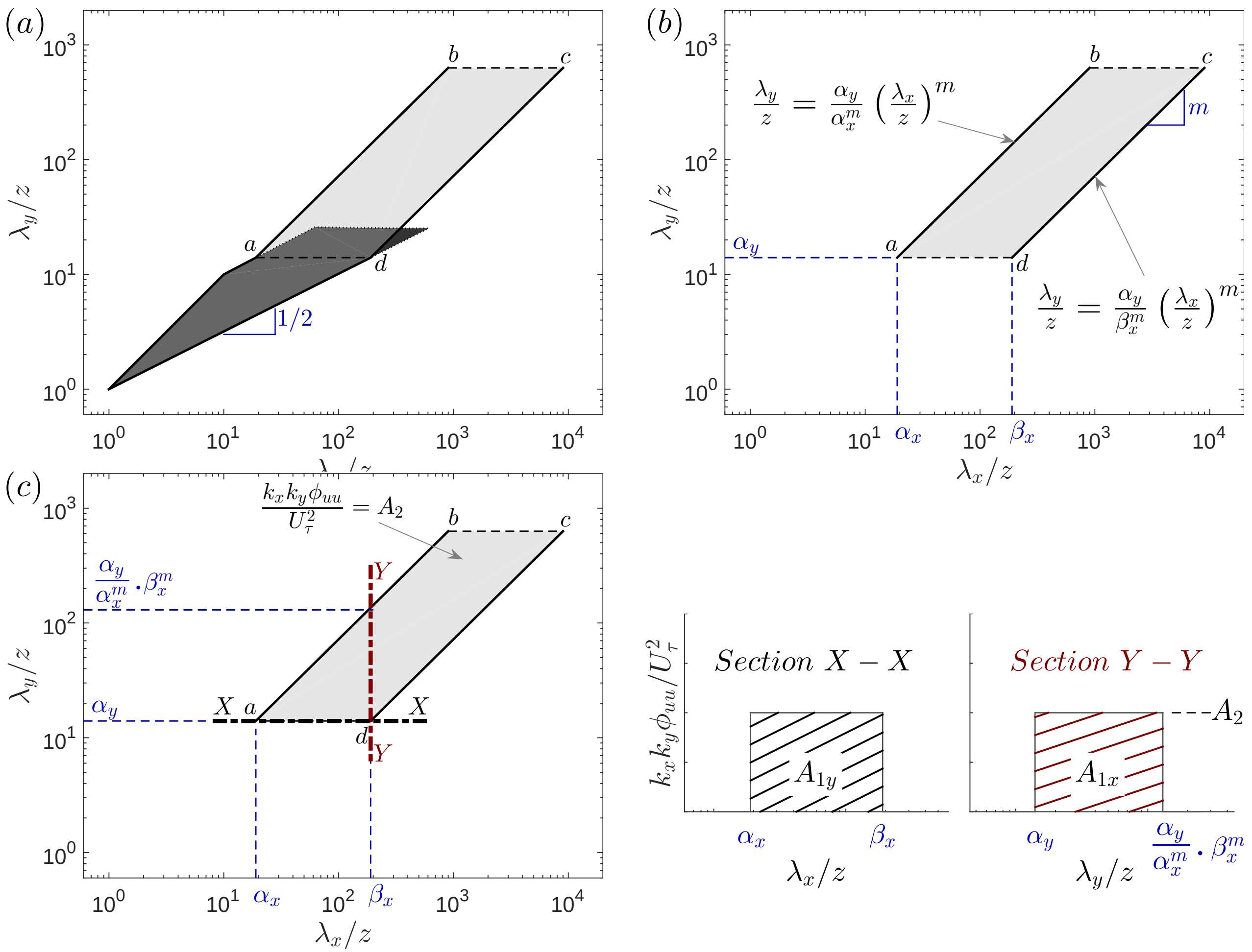

FIGURE 5.4: (a) Sketch of organization of the 2-D spectra for low (dark shade) and high (light shade) Reynolds numbers, (b) *large eddy region* (a-b-c-d) with the associated power law and (c) graphical representation of line integrals of the *large eddy region* with A_{1x} and A_{1y} denoting the respective hatched cross-sectional areas.

length scales, α_x, β_x and α_y (as shown in figure 5.4(b)), then (α_x, β_x) represent the range of *lengths* for the transitional eddy *width*, α_y. In this case, the power laws described by Chung *et al.* (2015) could be modified as $\lambda_y/z = \alpha_y/\beta_x^m(\lambda_x/z)^m$ and $\lambda_y/z = \alpha_y/\alpha_x^m(\lambda_x/z)^m$ respectively where the power law coefficient 'm' is the slope of the *large eddy region* as shown in the figure.

In most turbulent flow experiments at very high Reynolds number, only the 1-D spectrum is available. The 1-D spectrum is simply the line integral of the 2-D spectrum at a given wavelength and can be calculated from our model as a function of streamwise and spanwise wavenumbers. If A_{1x} and A_{1y} denote the line integral of the *large eddy region* (with energy level, say, A_2) across the spanwise and streamwise wavenumbers respectively (as shown graphically in figure 5.4c), then,

$$A_{1x} = \left.\frac{k_x\phi_{uu}(k_x)}{U_\tau^2}\right|_{\frac{\lambda_x}{z}=\beta_x} = \int_{\alpha_y}^{\frac{\alpha_y}{\alpha_x^m}\cdot\beta_x^m} \frac{k_xk_y\phi_{uu}(k_x,k_y)}{U_\tau^2}\,\mathrm{d}\left(\ln\frac{\lambda_y}{z}\right) = A_2\ln\frac{\beta_x^m}{\alpha_x^m}, \tag{5.3a}$$

$$A_{1y} = \left.\frac{k_y\phi_{uu}(k_y)}{U_\tau^2}\right|_{\frac{\lambda_y}{z}=\alpha_y} = \int_{\alpha_x}^{\beta_x} \frac{k_xk_y\phi_{uu}(k_x,k_y)}{U_\tau^2}\,\mathrm{d}\left(\ln\frac{\lambda_x}{z}\right) = A_2\ln\frac{\beta_x}{\alpha_x} \tag{5.3b}$$

and $A_{1x}/A_{1y} = m$. The value of the coefficient, m, is therefore the ratio of the constant energy plateaus in the corresponding 1-D streamwise and spanwise pre-multiplied spectra. So when $m = 1$, the slope of the bounds of the *large eddy region* is unity, meaning the eddies within this region have the same energy and they grow proportionally in both the streamwise and spanwise dimensions. Hence, these eddies in the *large eddy region* satisfy the conditions of self-similarity.

For comparison of the results with the simple spectra model above, figure 5.5(a) shows the 1-D streamwise and spanwise pre-multiplied spectra of u measured at $Re_\tau \approx 26000$ and at $z^+ = 418\,(= 2.6Re_\tau^{1/2})$. Figure 5.5(b) shows the 'ridge' of the 2-D spectrum, which is defined as the maximum value of $k_xk_y\phi_{uu}/U_\tau^2$ corresponding to each streamwise wavelength. The deviation of the ridge from $m = 0.5$ (square-root relationship) to a higher slope in the *large eddy region* is evident. The length scales where the 1-D streamwise and spanwise spectra plateau to a constant energy are $\lambda_x \sim 150z$ (2.5δ) and $\lambda_y \sim 20z$ (0.3δ) respectively, and these length scales are

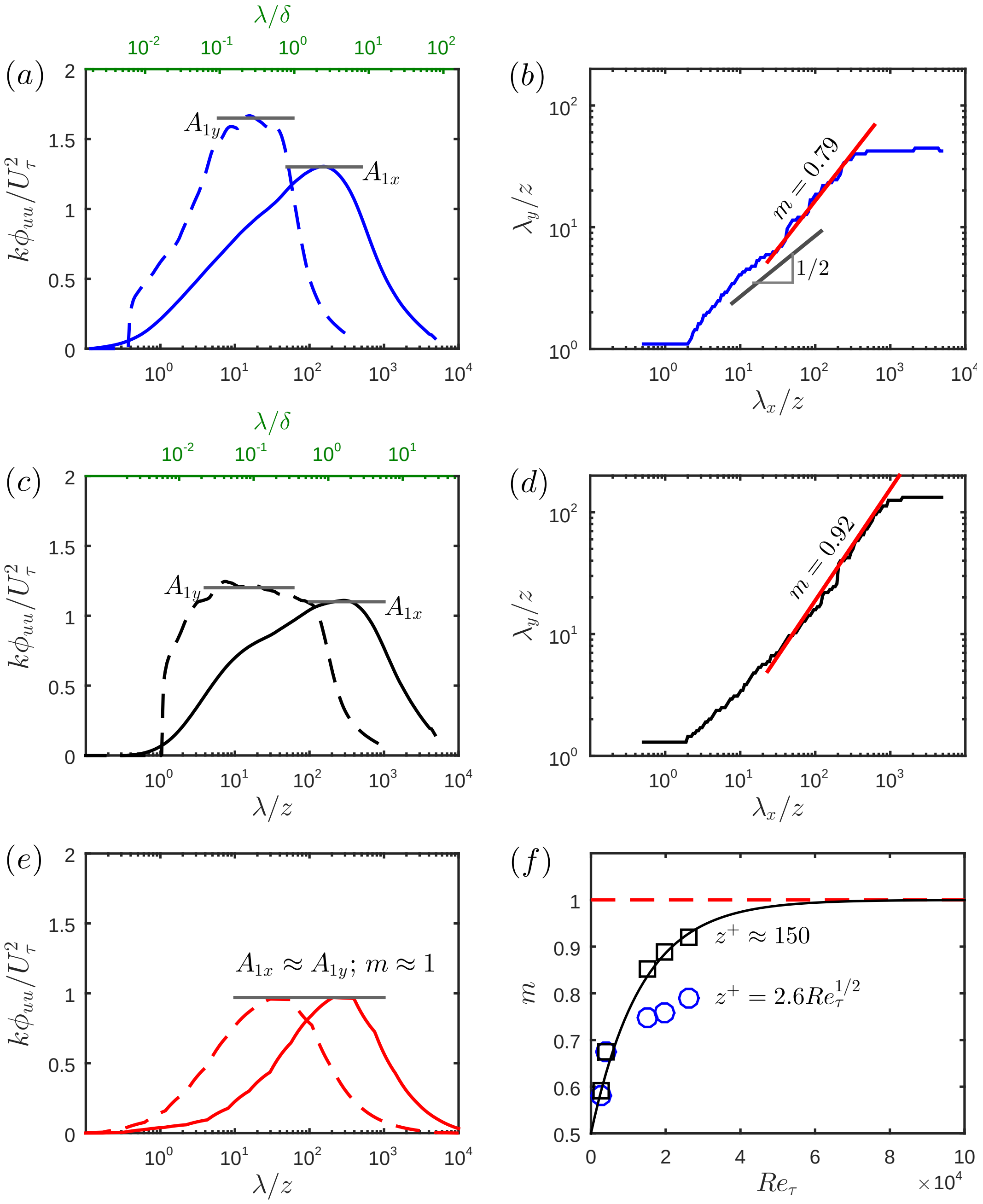

FIGURE 5.5: (a) & (c) 1-D streamwise (solid) and spanwise (dashed) spectra at $Re_\tau \approx 26000$ for $z^+ = 418\,(= 2.6{Re_\tau}^{1/2})$ (blue) and $z^+ \approx 150$ (black) respectively, (b) & (d) ridges of corresponding 2-D spectrum fitted with the calculated slope, (e) 1-D streamwise (solid) and spanwise (dashed) spectra from attached eddy model at matched $Re_\tau \approx 26000$ and $z^+ = 2.6{Re_\tau}^{1/2}$ and (f) variation of m versus Re_τ with the exponential fit of the form $m = 1 - C_1 exp(-Re_\tau/C_2)$.

within the *large eddy region* of figure 5.5(b). By considering either the slope of the ridge or the ratio of the peaks of the 1-D energy spectra (figure 5.5a), it is found that $m = A_{1x}/A_{1y} = 0.79$ is a good fit to the data. We now consider the same analysis applied to a lower wall height, $z^+ \approx 150$. Even though this wall location is below the log-region defined by Klewicki *et al.* (2009) at this Reynolds number, we might still find some scales of motion exhibiting self-similarity when sufficiently far from the wall. The availability of the 2-D spectra allows us to identify these scales, which would not be possible with only the 1-D spectrum. Figure 5.5(c) shows that the difference between A_{1x} and A_{1y} is less compared to the previous wall-distance. This results in a higher value of $m = 0.92$ (figure 5.5d). The increase in the value of m suggests a greater contribution to the energy at $z^+ \approx 150$ from structures that exhibit a self-similar growth. Provided there are still inertia-dominated motions at this wall-distance, the attached eddy hypothesis predicts a larger population of self-similar eddies to exist as we approach the wall (Townsend, 1976) and so the above result is not entirely unexpected. Figure 5.5(e) shows the 1-D streamwise and spanwise spectra obtained from the attached eddy model (refer figure 5.3), where only self-similar packets of eddies are present. The results show that $A_{1x} \approx A_{1y}$ such that $m = 1$, as expected. However, a clear k^{-1} scaling is still not evident due to an insufficient range of scales within the *large eddy region* (see figure 5.3b).

5.5.1 m vs Re_τ: indicator of self-similarity

The power law coefficient (m) is shown above to be an effective indicator of self-similarity and its value can be calculated from both 1-D and 2-D spectra. Arguments for self-similarity require asymptotically large Reynolds numbers, so it would be useful to understand the behaviour of m with increasing Reynolds number. The variation of m for $Re_\tau \approx 2400-26000$ is plotted in figure 5.5(f). The value of m increases monotonically with Reynolds number for both the $z^+ = 2.6Re_\tau^{1/2}$ and $z^+ \approx 150$ cases. However, the trend towards self-similarity is more evident at $z^+ \approx 150$. An exponential fit of the form $m = 1 - C_1 exp(-Re_\tau/C_2)$ is reasonable for the $z^+ \approx 150$ case. The value of C_1 is taken as 0.5 such that $m \to 0.5$ as $Re_\tau \to 0$, which preserves the square-root relationship of the bounds of high energy in the 2D spectrum at low Reynolds numbers. The value of C_2 is simply fitted to the data. Extrapolating the fit to very high Reynolds numbers, it is observed that the value of m approaches unity at $Re_\tau \approx 60000$ for the wall location considered (this is only indicative within the experimental uncertainty of the data). At such a high Reynolds number, a region of constant energy in the 2-D spectra at a wide range of length scales would be found to follow a linear relationship of the form $\lambda_y/z \sim \lambda_x/z$. This means we should not expect to see a clear k^{-1} scaling in both 1-D streamwise and spanwise spectra with $A_{1x} \approx A_{1y}$ for Reynolds numbers below $Re_\tau \approx 60000$. Here we note that the logarithmic law in $\overline{u^2}$ is less sensitive to deviations from self-similarity than the energy spectra (Chung *et al.*, 2015), and in fact several studies exist where the logarithmic law is observed even when the k^{-1} scaling remained elusive (Hultmark *et al.*, 2012, Marusic *et al.*, 2013).

5.6 Scaling of 2-D spectra

The scaling of 2-D spectra is discussed in this section with the aid of contours of constant energy ($k_x k_y \phi_{uu}/U_\tau^2$) and by also looking at the energetic ridges.

5.6.1 Viscous scaling

In the near-wall region, based on dimensional analysis of the streamwise energy spectrum of u, Samie *et al.* (2018) identified that spectra at moderate to very high wavenumber motions (moderate to very small wavelengths) are functions of only k^+ and z^+ (+ denotes inner-normalization) and are independent of Reynolds numbers. They showed Reynolds number invariance for $\lambda_x^+ < 15000$ and for $z^+ < 280$. In the present experiments, as discussed in §4.5, such invariance of small-scale energy with Reynolds number is utilized to correct for the smaller scales that are not resolved due to the initial separation between the closest hot-wires.

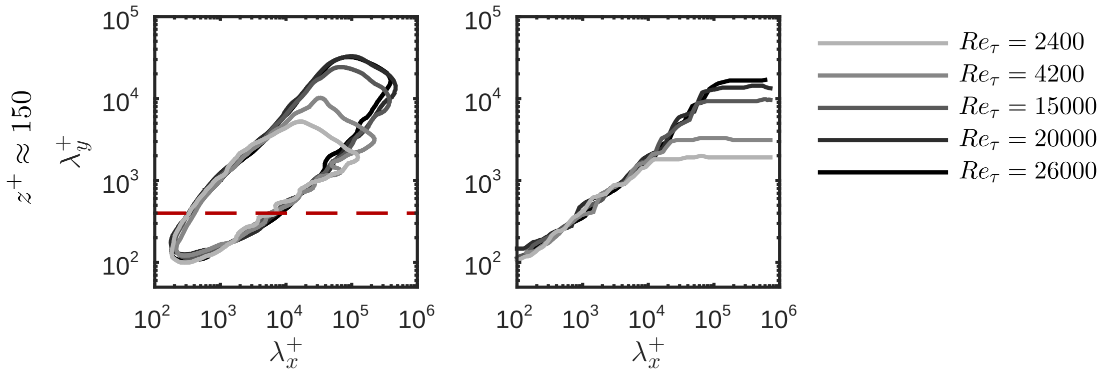

FIGURE 5.6: Viscous scaling of 2-D spectra for different Reynolds numbers: left panel shows contours of constant energies corresponding to $k_x k_y \phi_{uu}/U_\tau^2 = 0.15$, and the right panel shows the energetic ridges. The red dashed line in the left panel indicates $2 \times (dy^+_{initial})_{\max}$, above which the energetic scales are expected to be unaffected by the DNS-based correction scheme (refer §4.5). $(dy^+_{initial})_{\max}$ is the maximum value of $dy^+_{initial}$ at any given dataset, considered here.

Hence, the collapse of viscous-scaled small-scales in the corrected 2-D spectra is enforced. However, as shown in figure 5.6 for $z^+ \approx 150$ and $2400 \leq Re_\tau \leq 26000$, it is interesting to note that the collapse extends well beyond the corrected small-scale-region. In agreement to the observation of Samie *et al.* (2018), the scaling extend up to moderate streamwise wavelengths of $\lambda_x^+ \approx 15000$. In the spanwise direction, the scales smaller than $\lambda_y^+ \approx 2000$ appear to be invariant with Reynolds number, for the range considered. The Reynolds number trend is quite evident beyond $\lambda_x^+ \approx 15000$ and $\lambda_y^+ \approx 2000$.

5.6.2 Outer-flow scaling

Following Townsend (1976) and the dimensional analysis based arguments of Perry *et al.* (1986) (discussed in §2.2.1), in the logarithmic region where $\nu/U_\tau << z << \delta$, eddies having sizes $\mathcal{O}(\delta)$ would contribute only to the large-scale motions ($\lambda_x \sim \delta, \lambda_y \sim \delta$) in u. Hence, a constant energy region in the resulting 2-D spectrum is expected to follow outer-flow scaling of the form,

$$\frac{\phi_{uu}(k_x, k_y)}{\delta U_\tau^2} = f_1(k_x\delta, k_y\delta). \tag{5.4}$$

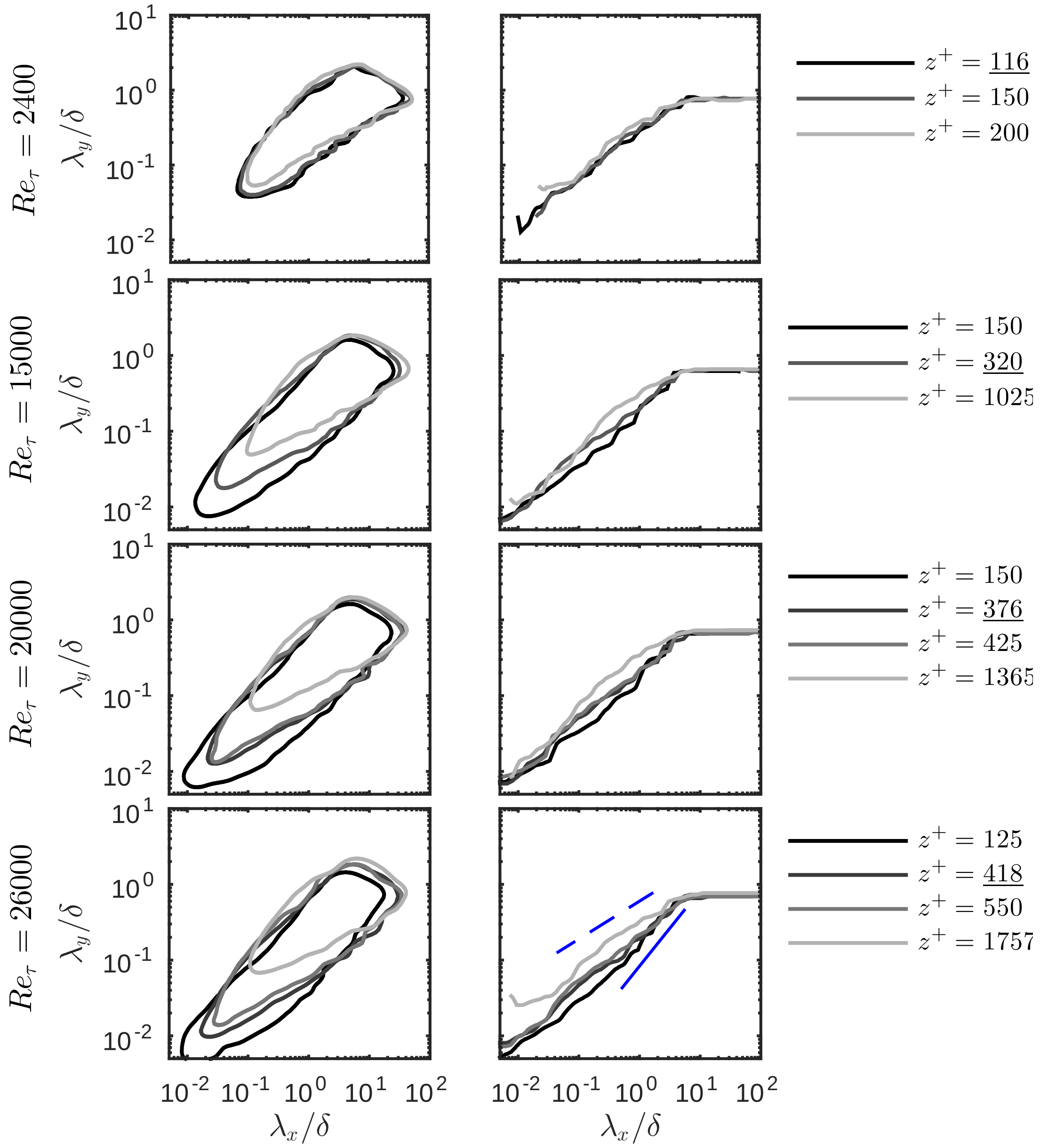

FIGURE 5.7: Outer-flow scaling of 2-D spectra for different Reynolds numbers: left panels are contours of constant energy corresponding to $k_x k_y \phi_{uu}/U_\tau^2 = 0.15$ and the right panels are the energetic ridges. The blue solid and dashed lines denote the $\lambda_y/\delta \sim \lambda_x/\delta$ and $\lambda_y/\delta \sim (\lambda_x/\delta)^{1/2}$ relationships respectively. The wall-heights that are underlined in the legend represent $2.6Re_\tau^{1/2}$.

The experimental 2-D spectra in outer-flow scaling, where the wavelengths are scaled with the boundary layer thickness δ, are shown in figure 5.7 for $2400 \leq Re_\tau \leq 26000$. A good collapse of the 2-D spectra at scales larger than $\lambda_x \approx 7\delta$ and $\lambda_y \approx \delta$ is observed at all Reynolds numbers and for $2.6Re_\tau^{1/2} \leq z^+ \leq 0.15Re_\tau$. However, for $z^+ < 2.6Re_\tau^{1/2}$ ($z^+ \approx 150$ in high Reynolds number cases), the contour of constant energy appears to be narrower and deviates from δ-scaling. This is likely to be the result of a relatively low energy contribution from the very large scale motions at that wall-height. The argument is in line with the findings of Baars & Marusic (2018*a*), who showed that the energy contributed by very large-scale structures that are coherent with the wall, is roughly constant for $2.6Re_\tau^{1/2} \leq z^+ \leq 0.15Re_\tau$ and reduces for $z^+ < 2.6Re_\tau^{1/2}$. However, from figure 5.7, it is interesting to note that the energetic ridges show a collapse at very large scales even for $z^+ \approx 150$, which means that structures of those scales do preserve their 2-D geometry for the wall heights considered. The energetic ridge appears to grow at a constant λ_y ($\approx \delta$) for $\lambda_x \geq 7\delta$; a characteristic of superstructures that generates long positive streamwise correlations flanked by anti-correlation in the spanwise direction. $\lambda_y \approx \delta$ agrees with the spanwise width of the anti-correlation (Hutchins & Marusic, 2007*a*). Since the width of such very large scale motions have been reported to grow linearly with wall-height (Ganapathisubramani *et al.*, 2005, Hutchins & Marusic, 2007*a*), the same trend could be expected of the 2-D spectra in the outer-region.

Now, in the *large eddy region*, for $\lambda_x < 7\delta$, the energetic ridges follow the relationship $\lambda_y/\delta \sim (\lambda_x/\delta)^m$, where m is the slope of the 2-D spectrum. As discussed in §5.5.1, the value of m increases with increasing Re_τ at a fixed wall-location. Figure 5.8 shows the δ-scaled 2-D spectra for different Reynolds numbers at fixed z/δ. Except for the very small viscosity-dependent motions, the spectra shows a good overlap especially at high Reynolds numbers. Hence increasing the Reynolds number (δ^+) at a fixed z^+ is equivalent of moving towards smaller z/δ for $z >> \nu/U_\tau$. Therefore, as observed in figure 5.7, the value of m increases with decreasing z/δ. Hence, a true δ-scaling at these length scales in the *large eddy region*, that contributes to the low-wavenumber peak, can be expected only when the value of m

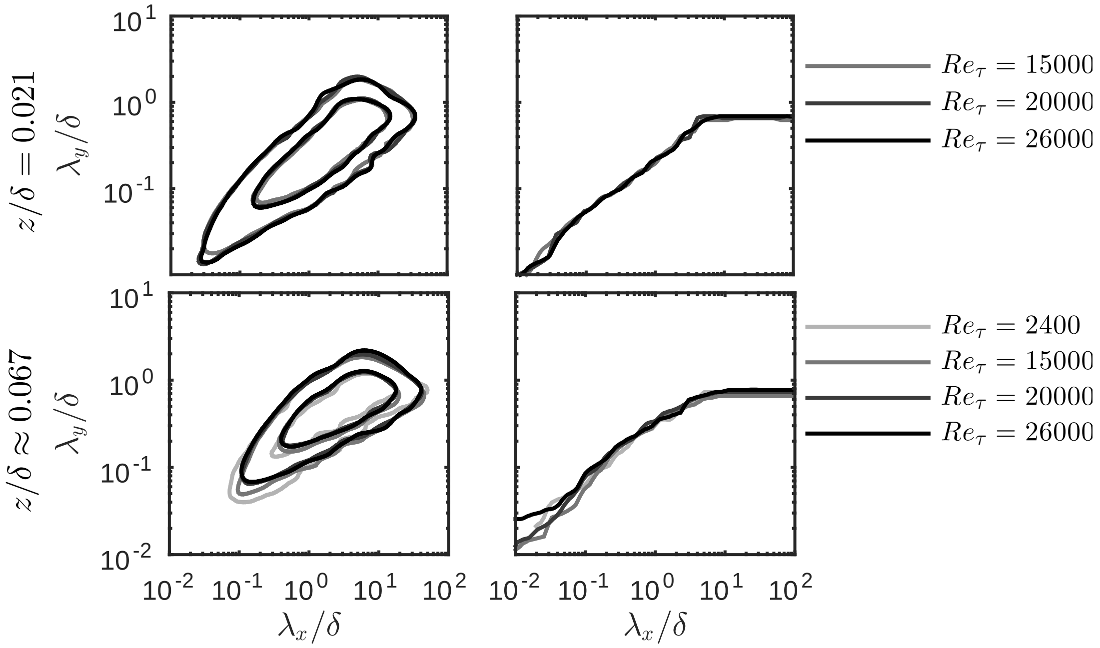

FIGURE 5.8: Outer-flow scaling of 2-D spectra at fixed z/δ for different Reynolds numbers: left panels are contours of constant energies corresponding to $k_x k_y \phi_{uu}/U_\tau^2 = 0.15$ and 0.35, and the right panels are the energetic ridges.

matures to 1 (expected approximately at $z/\delta = 150/60000 = 0.0025$ from figure 5.5f).

5.6.3 Inner-flow scaling

Similar to the outer-flow scaling arguments, the eddies of sizes $\mathcal{O}(z)$, in the logarithmic region where $\nu/U_\tau << z << \delta$, contribute to only the intermediate-scale motions ($\lambda_x \sim z, \lambda_y \sim z$) in u. Hence, a constant energy region in the resulting 2-D spectrum is expected to follow an inner-flow scaling of the form,

$$\frac{\phi_{uu}(k_x, k_y)}{zU_\tau^2} = f_2(k_x z, k_y z). \tag{5.5}$$

The experimental 2-D spectra in inner-flow scaling (z-scaling), where the wavelengths are scaled with the wall-normal distance z, are shown in figure 5.9 for $2400 \leq Re_\tau \leq 26000$. The energy contributed by streamwise and spanwise scales in the range $\mathcal{O}(z)$ to $\mathcal{O}(10z)$ appear to collapse well with inner-flow scaling at all Reynolds numbers and wall-heights considered here. Spectra at very small scales

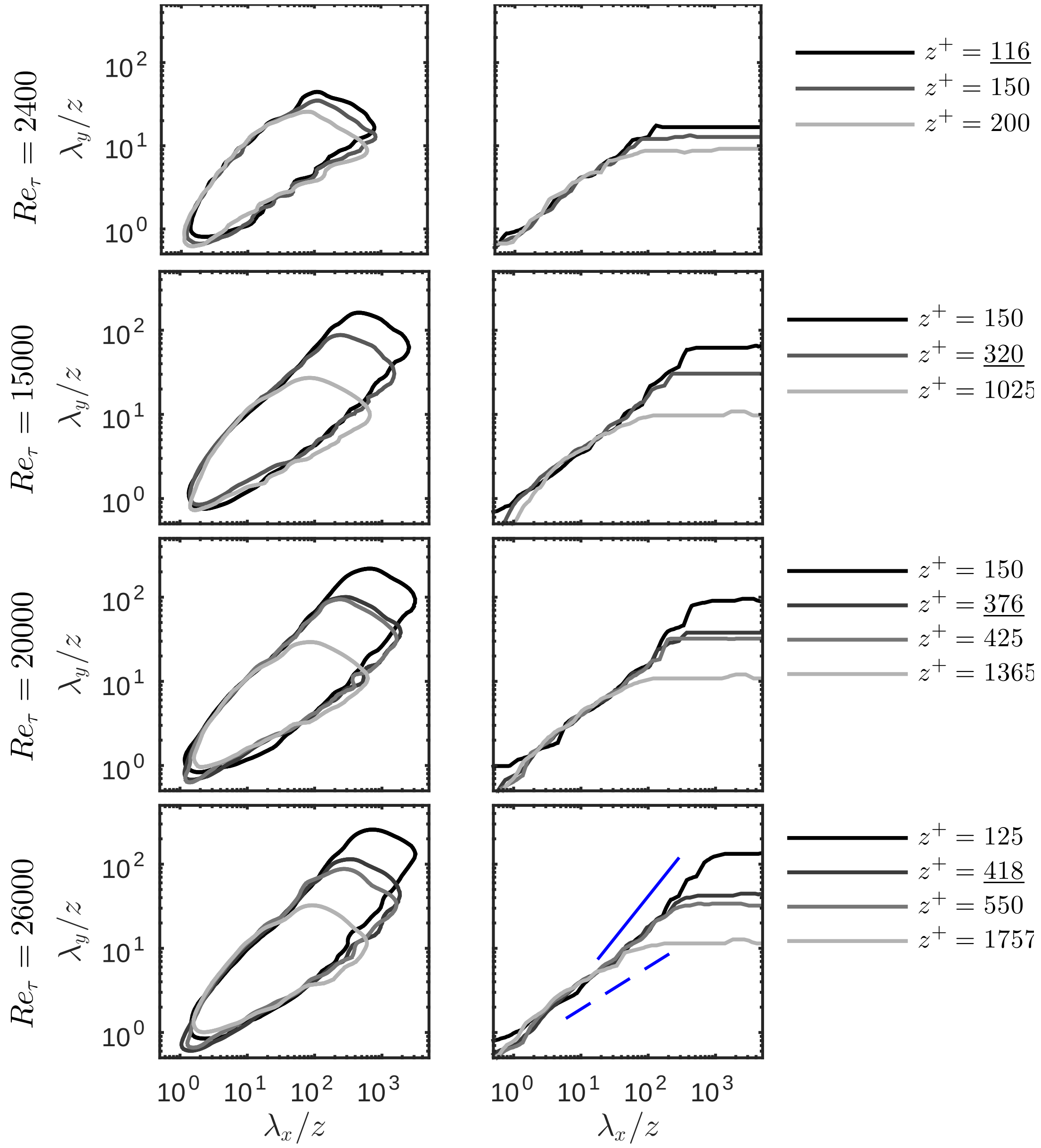

FIGURE 5.9: Inner-flow scaling of 2-D spectra for different Reynolds numbers: left panels are contours of constant energy corresponding to $k_x k_y \phi_{uu}/U_\tau^2 = 0.15$ and the right panels are the energetic ridges. The blue solid and dashed lines denote the $\lambda_y/z \sim \lambda_x/z$ and $\lambda_y/z \sim (\lambda_x/z)^{1/2}$ relationships respectively. The wall-heights that are underlined in the legend represent $2.6Re_\tau^{1/2}$.

(high wavenumber motions) that are viscosity dependent, deviate from the inner-flow scaling and are expected to follow the classic Kolmogorov scaling (Perry *et al.*, 1986, Saddoughi & Veeravalli, 1994). Now, at wavelengths larger than $(\lambda_x, \lambda_y) \sim \mathcal{O}(10z)$, the spectra deviates from a pure z-scaling while trending towards the relationship $\lambda_y/z \sim (\lambda_x/z)^m$. As highlighted in figure 5.9 for the highest Re case, the value of m is observed to vary from 0.5 to 1 while moving closer to the wall. This variation of m with z/δ (or Re_τ) results in the large-scales deviating from a pure z-scaling. Hence, for 2-D spectra whose slope m approaches unity (smaller z^+ at high Reynolds numbers), a better collapse with inner-flow scaling is observed in the *large eddy region* (up to $\lambda_x \sim 100z$). However, we note that the value of m should mature to unity in order to observe a pure wall-scaling at these large scales.

A comment on k^{-1} scaling in the 1-D spectrum

As discussed in §2.2.1, a k^{-1} plateau is expected in the overlap region in 1-D spectra where both the inner-flow and outer-flow scalings hold. This would require the low-wavenumber peak in the 1-D spectra to scale with both z and δ. Referring to the discussions in §5.3 to §5.5, the low-wavenumber peak in the 1-D spectra is contributed by structures occupying the *large eddy region* in the 2-D spectra. Therefore, a true k^{-1} plateau in the 1-D spectra would require a perfect inner-flow and outer-flow scaling of the *large eddy region* in the 2-D spectra. However, from the above discussions, such a scaling in the *large eddy region* would necessarily require the value of the slope (m) of the 2-D spectra to be unity, which is expected only at $Re_\tau > 60000$ (or $z/\delta < 0.0025$; for $z >> \nu/U_\tau$).

5.7 Chapter summary

Two-dimensional (2-D) spectra across a decade of Reynolds number ($Re_\tau \approx 2400-26000$) for the logarithmic region is presented. While the small-scale contributions are found to be universal when scaled in viscous units, the large-scale contributions show a clear trend for the Reynolds number range examined. Specifically, the contours of 2-D spectra for large streamwise and spanwise wavelengths (λ_x and λ_y) are observed to tend towards a $\lambda_y \sim \lambda_x$ relationship with increasing Reynolds number, starting from a $\lambda_y/z \sim (\lambda_x/z)^{1/2}$ behaviour observed at the lowest Reynolds number measured. It should be noted that the $\lambda_y \sim \lambda_x$ relation indicates self-similarity (i.e. the range of scales with an equal energetic contribution to the streamwise velocity maintain a constant aspect ratio λ_x/λ_y), while the lower Reynolds number $\lambda_y/z \sim (\lambda_x/z)^{1/2}$ behaviour is indicative of structures growing faster in the x direction compared to y.

A simple model that describes the 2-D spectral contributions from the large-scales as a region of constant energy bounded by $\lambda_y/z \sim (\lambda_x/z)^m$ is presented. Here the power law coefficient 'm' corresponds to the slope of the constant energy bounds of 2-D spectra at large scales, or equivalently, the ratio between the constant energy plateaus in 1-D pre-multiplied spectra in the streamwise and spanwise directions. The power law coefficient is proposed to be an effective indicator of self-similarity, and empirical evidence for m monotonically approaching unity with an increase in Reynolds number is presented. A true k^{-1} scaling in the 1-D spectra requires perfect inner-flow and outer-flow scalings of the 2-D spectra in the *large eddy region*, which further require the value of m to be unity.

Chapter 6

2-D spectra from the Attached Eddy Model

Driven by the scaling of experimental 2-D spectra of u, in this chapter we model the logarithmic region of turbulent boundary layers based on the attached eddy framework. The attached eddy hypothesis proposed by Townsend (1976) and the subsequent attached eddy model (AEM) remain the most prevalent model for the logarithmic region in turbulent boundary layers. The AEM predicts the kinematics and scaling laws associated with the energetic self-similar structures populating the logarithmic region, whose contribution is predominant at high Reynolds numbers. However, the discussions in chapter 5 and the recent high Reynolds number experiments (Baars & Marusic, 2018*a*, Baidya *et al.*, 2017) show that the self-similar wall-attached motions are not the only contributors to the total kinetic energy. In order to improve the predictions, we propose an extension to the AEM, based on the scaling arguments from the measured two-dimensional (2-D) spectra.

In this chapter, §6.1 details the procedure followed to compute the 2-D energy spectra from the AEM. In §6.2, an extension to the current AEM is proposed, where in, apart from the self-similar wall-attached eddies ($Type\,A$), we also incorporate two other structures into the model: $Type\,C_A$ and $Type\,SS$, that are representative of the wall-detached low-Reynolds number features and the wall-attached superstructures, respectively.

6.1 Attached Eddy Model

The key feature of the AEM is the concept of a 'representative attached eddy' (Marusic & Monty, 2019). Here, following experimental observations (Adrian *et al.*, 2000, Zhou *et al.*, 1996, 1999), the 'representative eddy' will be considered to be a packet of vortices (shown in figure 6.1(a)), with 'Λ-hairpins' at various stages of their self-similar growth aligned in the streamwise direction (Dennis & Nickels, 2011, Marusic, 2001). The growth angle of the packet, which is the angle of the line connecting the heads of the first and the last hairpins in a packet, is 10° (Zhou *et al.*, 1999). The height of the packet is $\mathcal{H}$ and Δx_p is the spacing between the hairpins within the packet. The width ($\mathcal{W}$) and the length ($\mathcal{L} = \mathcal{H} + (\mathcal{N} - 1)\Delta x_p$) of the packet are chosen such that the desired aspect ratio (λ_x/λ_y) is achieved in the resulting 2-D energy spectrum (details in §6.1.3). Here is the number of hairpins in the packet. The basis for choosing $\mathcal{N}$, the number of hairpins in the packet, and consequently Δx_p for a given $\mathcal{L}/\mathcal{H}$, is described in §6.1.2.

The boundary layer is then populated with multiple hierarchies of such representative eddies (Perry *et al.*, 1986), where a 'hierarchy' refers to a collection of eddies with identical characteristic heights. For illustrative purposes, figure 6.1(c) represents a discretized model with three distinct hierarchies of self-similar eddies. While the height of the largest eddy (black) in the topmost hierarchy is δ_E (of the order of boundary layer thickness δ), the next smallest hierarchy represents eddies whose heights are a fixed fraction of δ_E and so on. However, it is to be noted that unlike figure 6.1(c), the actual simulation assumes a continuous hierarchy of eddies with the heights of the largest and the smallest eddies being $\mathcal{H}_L = \delta_E$ and $\mathcal{H}_S^+ = 100$ respectively.

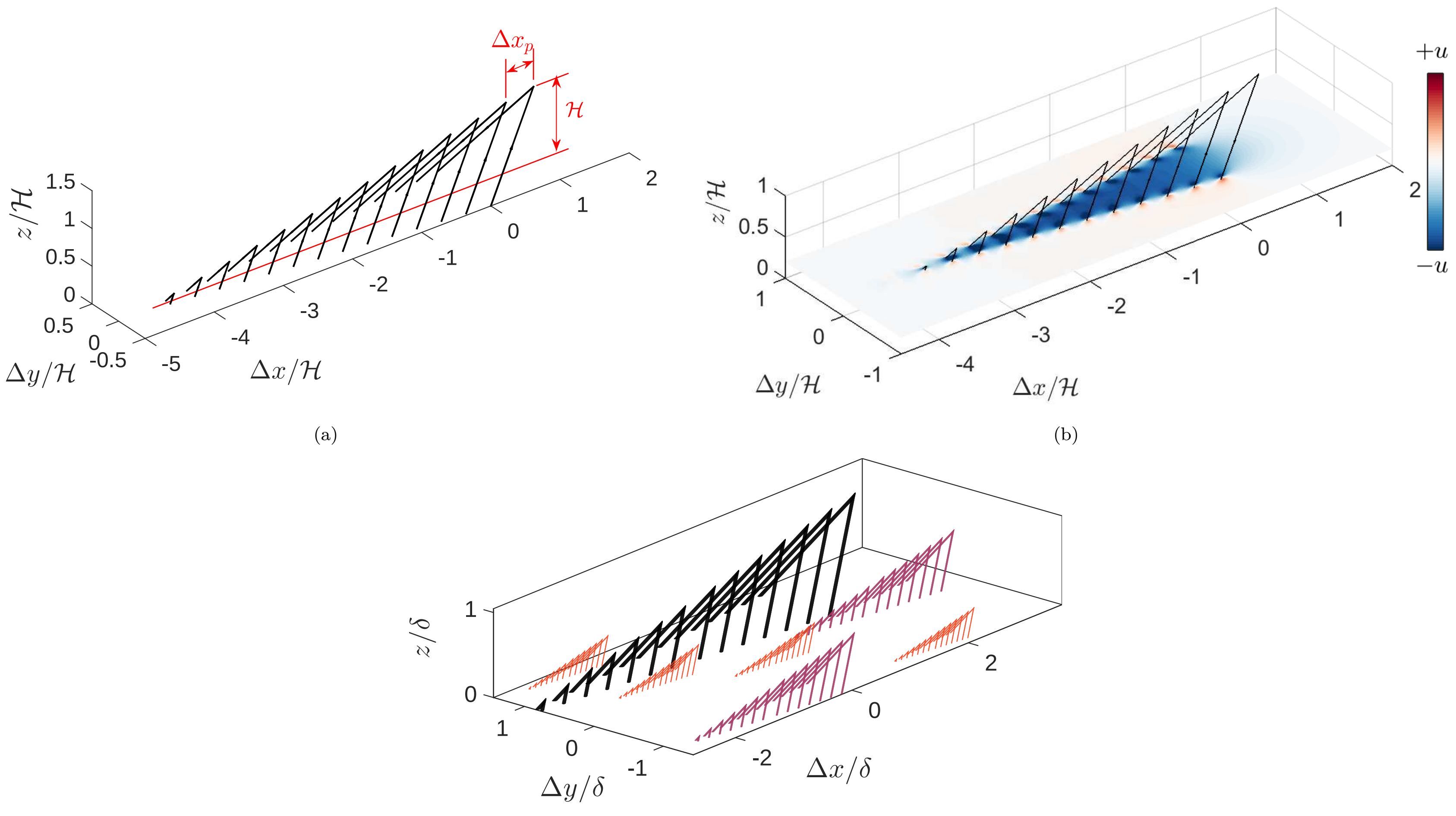

(a)

(b)

(c)

FIGURE 6.1: (a) Representative eddy, (b) streamwise velocity induced by the representative eddy at a wall-normal slice of $z/\mathcal{H} = 0.2$ and (c) illustration of the attached eddy model showing three distinct hierarchies of self-similar eddies with the size of the largest eddy (black) of the order of δ.

6.1.1 Details of the modelling procedure

An individual Λ-hairpin within a packet (as in figure 6.1(a)) is constructed using two vortex rods (together with their image vortices in the wall). Any discontinuity in the velocity field induced by connecting multiple vortex rods is observed to dissipate quickly (Perry & Chong, 1982). The characteristic radius of the rods are maintained to be $r_0 = 0.02\mathcal{H}$ and the vorticity varies along the thickness of the rod as a Gaussian distribution. The no-penetration condition at the wall is enforced by supplementing each vortex rod with its own mirror image at the wall. The velocity field $u_i(x/\mathcal{H}, y/\mathcal{H}, z/\mathcal{H})$, induced by the vortex rods of the representative eddy (along with its mirror image), is computed using the Biot-Savart law. Here, the subscript i denotes the different components of velocity. As an example, the streamwise velocity field at a fixed wall-height $z/\mathcal{H} = 0.2$, induced by a single representative eddy, is shown in figure 6.1(b). From the computed velocity field, the basis function for the 2-D spectrum, for a single representative eddy, is calculated as

$$\Phi_{ij}\left(k_x\mathcal{H}, k_y\mathcal{H}, \frac{z}{\mathcal{H}}\right) = \frac{2\,\hat{u}_i^*\,\hat{u}_j}{n_x^2 n_y^2 (\Delta k_x)(\Delta k_y)} \tag{6.1}$$

where, $\hat{u}_i(k_x\mathcal{H}, k_y\mathcal{H}, z/\mathcal{H}) = \mathcal{F}[u_i(x/\mathcal{H}, y/\mathcal{H}, z/\mathcal{H})]$ is the 2-D Fourier transform of u_i and the asterisk (*) indicates complex conjugate. In the above equation, n_x and n_y represent the number of streamwise and spanwise grid points respectively and $\Delta k_x = 2\pi/L_x$ and $\Delta k_y = 2\pi/L_y$, where L_x and L_y are the streamwise and spanwise lengths of the domain. The basis function Φ_{ij} is also known as the hierarchy spectral function (Perry *et al.*, 1986), which is the power spectral density of u_i, for a single representative eddy belonging to a hierarchy of size $\mathcal{H}$, and averaged in the wall-parallel plane at a fixed z.

Now, to compute the 2-D spectrum from all the representative eddies across the hierarchies ranging from $\mathcal{H}_S^+ = 100$ to $\mathcal{H}_L = \delta_E$, that are randomly aligned in the model, we use Campbell's theorem [1909] (see Woodcock & Marusic, 2015) along with the basis function Φ_{ij} computed from a single representative eddy as

$$\phi_{ij}\left(k_x\mathcal{H}, k_y\mathcal{H}, \frac{z}{\mathcal{H}_L}, \frac{z}{\mathcal{H}_S}\right) = \int_{\mathcal{H}_S}^{\mathcal{H}_L} \Phi_{ij}\left(k_x\mathcal{H}, k_y\mathcal{H}, \frac{z}{\mathcal{H}}\right)\mathcal{P}(\mathcal{H})\mathrm{d}(\mathcal{H}) \tag{6.2}$$

where,

$$\mathcal{P}(\mathcal{H}) = 1/\mathcal{H}. \tag{6.3}$$

Here, $\mathcal{P}(\mathcal{H})$ is the probability density function (Townsend, 1976). The inverse power distribution implies that within a hierarchy, when the size of an eddy (represented by its characteristic height $\mathcal{H}$) is halved, the number of eddies is doubled. Perry & Chong (1982) noted that such a distribution of eddies (equation 6.3) captures the logarithmic variation of U as well as the constant trend of the Reynolds shear stress $\overline{uw}$, as a function of wall-height.

Equation 6.2 can be written in logarithmic coordinates as,

$$\phi_{ij}\left(F_{zx}, F_{zy}, \zeta_L, \zeta_S\right) = \int_{\zeta_S}^{\zeta_L} \Phi_{ij}\left(F_{\mathcal{H}x}, F_{\mathcal{H}y}, \zeta_{\mathcal{H}}\right)\mathcal{W}_{\mathcal{F}}(\zeta_{\mathcal{H}} - \zeta_L)\,\mathrm{d}\zeta_{\mathcal{H}}, \tag{6.4}$$

where the logarithmic variables are defined as

$$F_{\mathcal{H}x} = \ln(k_x\mathcal{H}), \quad F_{\mathcal{H}y} = \ln(k_y\mathcal{H}), \quad F_{zx} = \ln(k_x z), \quad F_{zy} = \ln(k_y z) \tag{6.5a}$$

$$\zeta_{\mathcal{H}} = \ln(\mathcal{H}/z), \quad \zeta_S = \ln(\mathcal{H}_S/z), \quad \zeta_L = \ln(\mathcal{H}_L/z). \tag{6.5b}$$

In equation 6.4, $\mathcal{W}_{\mathcal{F}}(\zeta_{\mathcal{H}} - \zeta_L)$ is the weighting function that accounts for the probability density of the representative eddies in the hierarchy and following equation 6.3, $\mathcal{W}_{\mathcal{F}}(\zeta_{\mathcal{H}} - \zeta_L) = 1$. Further explanations of these steps along with graphical descriptions can be found in Perry *et al.* (1986).

As in experiments, the friction velocity U_τ is selected as the characteristic velocity scale and is computed by forcing the inner-normalized peak Reynolds shear stress to be unity in the logarithmic region (Buschmann *et al.*, 2009), i.e, peak $-\overline{uw}^+ = \max(-\overline{uw}/U_\tau^2) = 1$.

6.1.2 Criterion to choose Δx_p

The spacing between the hairpins, Δx_p (as shown in figure 6.1(a)), is chosen such that the wavelength corresponding to the periodicity imposed by Δx_p does not interfere with the energetic scales in the spectrum. As an example, let us consider three values of $\Delta x_p = 0.1\mathcal{H}, 0.2\mathcal{H}$ and $0.4\mathcal{H}$ to generate a packet with $\mathcal{L}/\mathcal{H} \approx 6$, and hence obtain their 2-D $u-$, $v-$ and $w-$ spectra, as shown in figure 6.2. It is observed that, for $\Delta x_p = 0.4\mathcal{H}$ and $0.2\mathcal{H}$, the spectra appears energetic at scales smaller than $\lambda_x/\delta_E = \Delta x_p/\mathcal{H}$ (indicated by the white dashed line), especially when considering the v and w velocity components. This is an artefact of the ringing in the velocity field, within the representative eddy, imposed by the spacing between the hairpins within the packet. Now, considering $\Delta x_p = 0.1\mathcal{H}$, even the wavelength corresponding to the hairpin-spacing of the largest eddy (i.e. $\lambda_x/\delta_E = 0.1$, that is indicated by the white dashed line) appear to be smaller than the smallest energetic scales. Hence the spectra of all three velocity components appear to be devoid of any artificial energy. Therefore, for the present study, $\Delta x_p = 0.1\mathcal{H}$ is chosen. An alternative method which is expected to give statistically similar results and is not implemented in the present study, would be to use a lesser number of hairpins and introduce randomness or 'jitter' in the spacing between them (to better represent the actual velocity field that is not made of such discrete eddies).

6.1.3 2-D spectra for representative eddies of different $\mathcal{L}/\mathcal{W}$

In this section, we study the effect of the streamwise-spanwise aspect ratio ($\mathcal{L}/\mathcal{W}$) of the representative eddy on the 2-D spectrum of u. The aspect ratio is varied from $\mathcal{L}/\mathcal{W} = 1$ to $\mathcal{L}/\mathcal{W} \approx 6$. Eddies of increasing $\mathcal{L}/\mathcal{W}$ are obtained by increasing the number of hairpins ($\mathcal{N}$) within a packet, while maintaining a constant hairpin-spacing of $\Delta x_p = 0.1\mathcal{H}$ and a fixed width ($\mathcal{W}$) for the largest hairpin in the packet. Therefore, $\mathcal{L}/\mathcal{W} = 1$ represents a single hairpin.

The 2-D spectra at a wall height $z^+ = 2.6 Re_\tau^{1/2}$ computed from such eddies of varying aspect ratios, at $Re_\tau \approx 26000$, is shown in figure 6.3. The constant

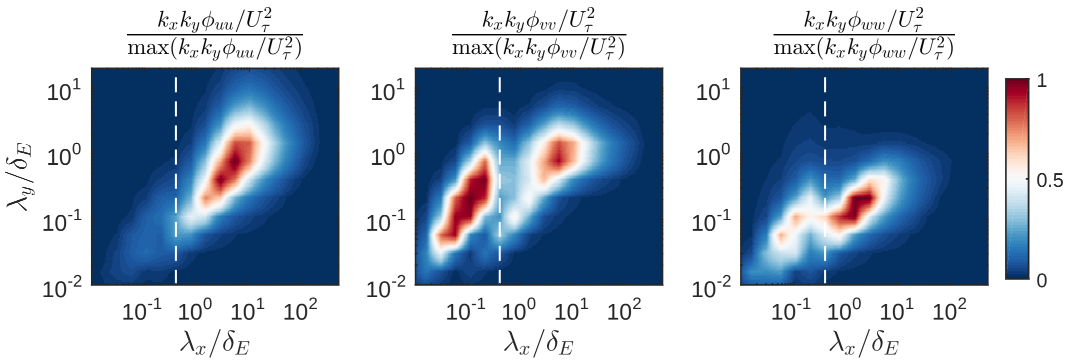

(a) $\Delta x_p = 0.4\mathcal{H}$

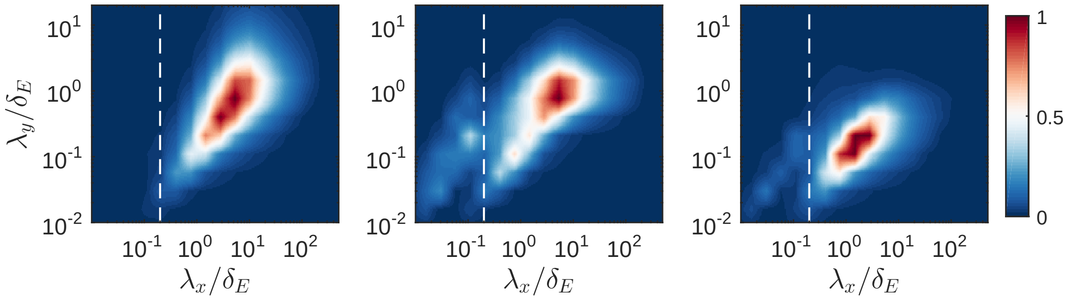

(b) $\Delta x_p = 0.2\mathcal{H}$

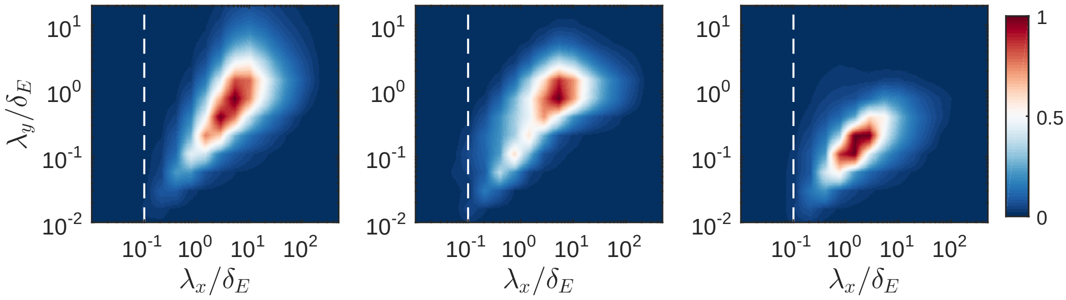

(c) $\Delta x_p = 0.1\mathcal{H}$

FIGURE 6.2: 2-D spectra of u, v and w velocity components for three values of Δx_p. The white dashed line indicates $\lambda_x/\delta_E = \Delta x_p/\mathcal{H}$.

energy bounds of the experimental 2-D spectrum at matched Reynolds number and wall-height are also indicated in the plots for reference. These bounds show the square-root (dashed line) as well as the linear (solid line) relationships between the streamwise and spanwise wavelengths. It can be observed that, with increasing $\mathcal{L}/\mathcal{W}$, the spectrum shifts towards larger streamwise wavelengths. On the other hand, the largest spanwise wavelength remains approximately the same for all the cases. This is because the spanwise wavelength is dictated by the width of the largest hairpin in the packet, which is fixed for all the cases. As seen from the $\mathcal{L}/\mathcal{W} = 1$ case (which was used exclusively until Marusic, 2001) in figure 6.3, there

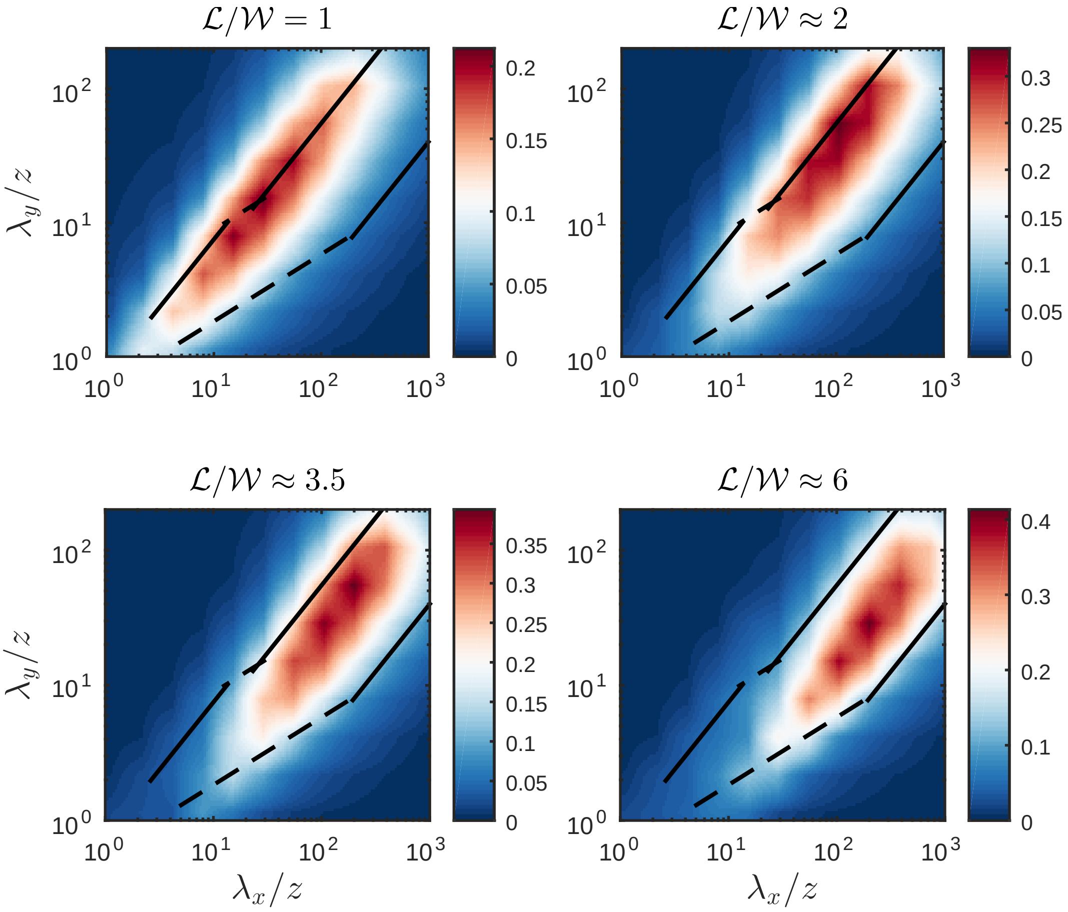

FIGURE 6.3: 2-D spectra of u at $Re_\tau \approx 26000$ and $z^+ = 2.6Re_\tau^{1/2}$ obtained with representative eddies of different $\mathcal{L}/\mathcal{W}$. The black lines correspond to the constant energy bounds from experimental 2-D spectra at matched Re_τ and z^+ as shown in figure 6.4(b).

is a clear mismatch between the constant energy bounds taken from experiments and the energy spectra computed from the single hairpins, which demonstrates that the 2-D spectrum cannot be modelled using single hairpins alone. On the other hand, the $\mathcal{L}/\mathcal{W} \approx 6$ case in figure 6.3 has an aspect ratio close to $\lambda_x/\lambda_y \approx 7$, which is the aspect ratio of the highly energetic ridge of the experimental 2-D spectrum, and therefore the *large eddy region* is captured reasonably well in this case.

However, as discussed in §5.4, such a model that comprises self-similar attached eddies alone resolves only a fraction of the total kinetic energy and also does not predict the square-root region in the 2-D spectrum. Therefore, extending the current AEM to include a greater range of energetic scales is essential (Marusic &

Monty, 2019) and forms the objective of the following section.

6.2 Extension of the attached eddy model

6.2.1 Introduction

The attached eddy model comprising solely of self-similar hierarchies of wall-attached motions (*Type A*) is observed to resolve only the *large eddy region* of the 2-D spectrum, as shown in figure 6.4. The smaller-scale region of the 2-D spectrum which follows a $\lambda_y/z \sim (\lambda_x/z)^{1/2}$ scaling is not captured by this model. The model also omits the contributions from the (non-self-similar) very large scale motions that are characteristic of the superstructures in turbulent boundary layers (Baars & Marusic, 2018*a*).

The significance of these energetic scales, that are unresolved by the attached eddy model, is emphasized in the recent investigations by Baars & Marusic (2018*a*,*b*). A data-driven approach is adopted in their studies to decompose the measured streamwise turbulent kinetic energy into three spectral components: a wall-incoherent

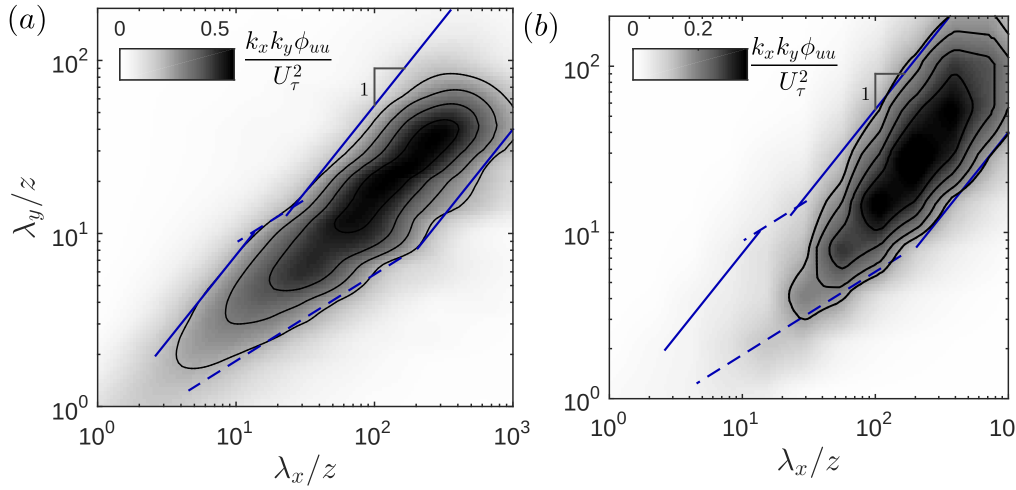

FIGURE 6.4: (a) 2-D spectrum at $z^+ = 2.6{Re_\tau}^{1/2}$ for $Re_\tau \approx 26000$; the black line contours represent $k_x k_y \phi_{uu}/U_\tau^2 = 0.25$, 0.35 and 0.45. (b) 2-D spectrum obtained from attached eddy model at same z^+ and Re_τ. The blue solid and dashed lines denote the $\lambda_y/z \sim \lambda_x/z$ and $\lambda_y/z \sim (\lambda_x/z)^{1/2}$ relationships respectively.

high wavenumber component and two wall-coherent lower wavenumber components that are the self-similar structures in the context of the attached eddy hypothesis and the very large scale motions, respectively. Baars & Marusic (2018*a*,*b*) report that a k^{-1} scaling in the 1-D streamwise spectra and the corresponding log-law in the streamwise turbulent intensity profile (Marusic *et al.*, 2013) are masked by the interaction of the above spectral subcomponents. Hence, at any practically encountered Reynolds number, a discussion of spectral self-similarity based on the attached eddy model is incomplete when only considering the *Type A* spectral component. This limitation of the attached eddy model is also noted by Marusic & Monty (2019), where they identify the extension of the current model by including a greater range of scales as a significant future study.

The objective of the current study is to extend the attached eddy model by identifying and incorporating (i) the representative wall-incoherent small-scale structures that populate the Reynolds number independent region of the 2-D spectra and (ii) the representative very large scale motions (or global modes) that are characteristic of the superstructures in turbulent boundary layers. To this end, in §6.2.2, a 2-D spectral scaling-driven approach is adopted and the significant spectral subcomponents are identified based on the scaling of measured 2-D spectra over a range of Reynolds numbers. §6.2.3 discusses the extension of the attached eddy model by incorporating the identified representative structures. §6.2.4 compares the results from the extended attached eddy model with those from experiments. A discussion on spectral self-similarity based on the extended attached eddy model is carried out in §6.2.6.

6.2.2 Inputs from experimental 2-D spectra to extend the model

The geometry and the organization of the eddies representing the major energy containing motions discussed above is chosen based on the scaling of experimental 2-D spectra at low ($Re_\tau = 2400$) and high ($Re_\tau = 26000$) Reynolds numbers. The details of the experimental data are given in table 6.1.

Facility	Re_τ	U_∞ (m/s)	δ (m)	U_τ (m/s)	z^+	z/δ	l^+	TU_∞/δ ($\times 10^3$)
Low-Re	2430	15	0.069	0.545	**116**	0.047	17	26
Low-Re	2430	15	0.069	0.545	150	0.062	17	26
Low-Re	2430	15	0.069	0.545	209	0.086	17	26
HRNBLWT	26090	40	0.337	1.231	125	0.005	39	14.2
HRNBLWT	26090	40	0.337	1.231	**418**	0.016	39	14.2
HRNBLWT	26090	40	0.337	1.231	550	0.021	39	14.2
HRNBLWT	26090	40	0.337	1.231	1757	0.067	39	14.2

TABLE 6.1: Details of experimental data used in this chapter; the values highlighted in bold indicate $z^+ = 2.6Re_\tau^{1/2}$.

6.2.2.1 Scaling of 2-D spectra

The surface plot of the pre-multiplied 2-D energy spectrum $k_x k_y \phi_{uu}/U_\tau^2$ (plotted in figure 6.4(a)) is shown in figure 6.5(a) as a function of λ_x and λ_y. The black contour represents a constant energy of $k_x k_y \phi_{uu}/U_\tau^2 = 0.15$ and the blue line is the energetic ridge of the 2-D spectrum which is calculated by finding the maximum value of $k_x k_y \phi_{uu}/U_\tau^2$ corresponding to each streamwise wavelength λ_x. The inner-flow scaling of the constant energy contours and the ridges is observed when the length scales are normalized by the wall-height (z), as shown in figures 6.5(b) and (c). The plot includes all the wall heights mentioned in table 6.1 for both the low ($Re_\tau \approx 2400$) and the high ($Re_\tau \approx 26000$) Reynolds numbers. Similarly, the outer-flow scaling of the constant energy contours and ridges is observed when the length scales are normalized by the boundary layer thickness (δ), as shown in figures 6.5(d) and (e). While a constant energy contour shows the spectrum of streamwise and spanwise length scales contributing equally to the turbulent kinetic energy, investigating its scaling at different wall-heights is important to establish 'energetic-similarity'. On the other hand, the energetic ridge of the 2-D spectra has been identified as a tool to observe 'geometric self-similarity' (del Álamo *et al.*, 2004, Chandran *et al.*, 2017).

The ridge represents the aspect ratios (λ_x/λ_y) of the most energetic scales at a given wall-height, and identifying these scales helps in the construction of a structure based model. For instance, in the case of the attached eddy model, the ridges can be used to estimate the geometry of the representative eddies, while the scaling of the ridges at different wall-heights and Reynolds numbers can explain the organization of these eddies within the boundary layer. Therefore, here we adopt a scaling-driven approach to identify the three major representative energy carrying motions, as discussed in §1, and these are described below.

(i) *Wall-coherent self-similar motions*:
Following the definition provided by Baars *et al.* (2017), wall-coherent structures in the outer-region would refer to the portions of velocity fluctuations in the outer-region, which are correlated with the velocity fluctuations very close to the wall (or the wall-shear stress signature). Baars *et al.* (2017) computes 1-D linear coherence spectra (LCS) to isolate such wall-coherent scales from the broadband turbulence. The readers could also refer to Tinney *et al.* (2006) and del Álamo *et al.* (2004) for a similar description of spectral coherence. Based on the 1-D LCS, Baars *et al.* (2017) observed that the structures that are coherent with the wall have streamwise wavelengths $\lambda_x > 14z$. These scales are represented by the dark-shaded region in figures 6.5(b) and (c). Note that the exact boundaries of the wall-coherent region in a 2-D spectrum can only be identified with the help of a 2-D LCS obtained as a function of both λ_x and λ_y (similar to figure 6.6). So the dark-shaded region is only an approximate reference for the wall-coherent scales, and some of the very small and the very large spanwise length scales within this region are expected to be incoherent with the wall. As discussed in chapter 5, the wavelengths of the large-scales tend to obey a relationship of $\lambda_y/z \sim (\lambda_x/z)^m$, where the value of m approaches unity at high Reynolds numbers, or as we move closer to the wall (for $z >> \nu/U_\tau$). It could be observed from the inner-flow scaling of the ridges (figure 6.5(c)) that the aspect ratio of such dominant large-scale structures that tend towards self-similarity ($\lambda_y \sim \lambda_x$) is $\lambda_x/\lambda_y \approx 7$. These large-scale self-similar structures that are coherent with the wall characterize Townsend's attached eddies. Additionally, when the wavelengths are scaled in δ as shown in figure 6.5(e), the ridges collapse at $\lambda_x \approx 7\delta$ and $\lambda_y \approx \delta$ resulting in the same aspect ratio

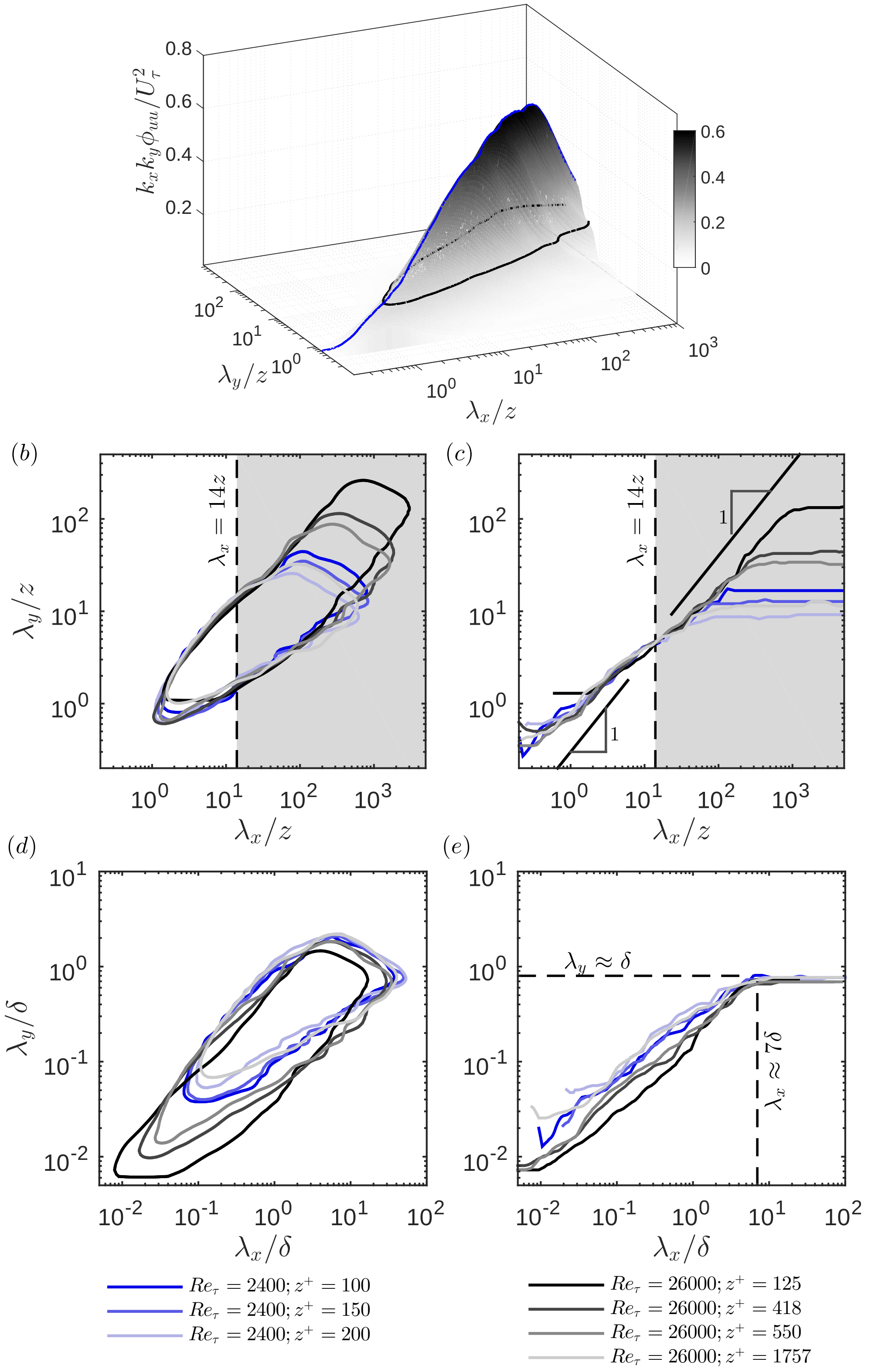

FIGURE 6.5: (a) The surface plot of a 2-D spectrum highlighting the energetic ridge (blue line) and a constant energy contour $k_x k_y \phi_{uu}/U_\tau^2 = 0.15$, (b & d) inner-flow scaling and outer-flow scaling respectively of the constant energy contour $k_x k_y \phi_{uu}/U_\tau^2 = 0.15$, (c & e) inner-flow scaling and outer-flow scaling respectively of the energetic ridge. The shaded region in (b) and (c) represents the wall-coherent scales as per Baars *et al.* (2017).

of $\lambda_x/\lambda_y \approx 7$. Therefore, the wall-attached self-similar structures would have a characteristic length and width of roughly 7δ and 1δ, in spectral space.

(ii) *Wall-coherent non-self-similar very large scale motions*:

The large-scales are observed to grow nearly self-similarly, i.e. $\lambda_y \sim \lambda_x$, until $\lambda_x \approx 7\delta$ and $\lambda_y \approx \delta$ (figure 6.5(e)). Beyond these limits, the ridge trend towards larger streamwise wavelengths (with the energy dropping), but maintaining a constant spanwise width of $\lambda_y \approx \delta$. A good collapse of the ridges is observed with outer-flow scaling, irrespective of Reynolds numbers. This agrees with the findings of Tomkins & Adrian (2005), which says that the structures with the largest streamwise wavelengths organize with a spanwise spacing of $\lambda_y/\delta = 0.75 - 0.9$. These spanwise spacings are consistent with the width of the anti-correlations of streamwise velocity in the spanwise direction, as observed by Hutchins & Marusic (2007*a*). They reported such events to have long streamwise correlations; a characteristic typical of 'superstructures' in boundary layer flows. It could be noted from figures 6.5(b) and (c) that these outer-scaled length scales are coherent with the wall but do not follow a self-similar scaling with z, similar to the 'global' modes of del Álamo & Jiménez (2003) that extends deep in the wall-normal direction. Even though the energetic ridges show a good collapse for $\lambda_x > 7\delta$ (figure 6.5e), the constant energy contours (figure 6.5d) collapse only within the logarithmic region ($2.6Re_\tau^{1/2} \leq z^+ \leq 0.15Re_\tau$). At $Re_\tau = 26000$, for $z^+ = 125 (< 2.6Re_\tau^{1/2})$, the contour appears to deviate from an energetic self-similarity. This trend is expected, since contribution to the energy at this wall height from the very large scale motions will be relatively low. The argument is also based on the findings of Baars & Marusic (2018*a*), who showed that the energy contribution from very large-scale structures that are coherent with the wall is roughly constant for $2.6Re_\tau^{1/2} \leq z^+ \leq 0.15Re_\tau$ and reduces for $z^+ < 2.6Re_\tau^{1/2}$. The authors showed that this results in an outer peak in the energy spectrogram of the very large scale sub-component, at about $\lambda_x \approx 10\delta$.

(iii) *Wall-incoherent wall-scaled motions*:

According to Baars *et al.* (2017), wall-incoherent motions are characterized by a streamwise/wall-normal aspect ratio of $\lambda_x/z < 14$ and correspond to the unshaded region in figures 6.5(b) and (c). In support of recent findings (Baars *et al.*, 2017, Baars & Marusic, 2018*a*,*b*), figure 6.5(b) shows the contribution of wall-incoherent structures to the turbulent kinetic energy, which is the area within 2-D spectra in the unshaded region, to be significant. Following the work of Perry & Marusic (1995) and Marusic & Perry (1995), Marusic & Monty (2019) in their recent review, identify the wall-incoherent motions as $Type\,C$ detached structures which chiefly constitute the Kolmogorov-type fine-scale turbulence and other detached structures including the self-similar ones that were formerly attached to the wall. The perfect inner-flow scaling of a large portion (all but the very small scales) of the wall-incoherent region of the 2-D spectra as shown in figure 6.5(b) justifies the existence of wall-detached motions whose characteristic lengths still scale with the distance from the wall. Additionally, the collapse of the constant energy contours for all the wall locations and Reynolds numbers considered here, suggests an invariant contribution of these wall-incoherent wall-scaled motions to the turbulent kinetic energy. Now, if we focus on the inner-flow scaling of the energetic ridges in this regime (figure 6.5(c)), a good collapse is observed and the ridges follow a $\lambda_y \sim \lambda_x$ behaviour towards the smaller scales resulting in an aspect ratio of $\lambda_x/\lambda_y \approx 1$. Such a linear relationship at the scales $\mathcal{O}(z)$ was also reported by del Álamo *et al.* (2004). So at high Reynolds number, the $\lambda_y/z \sim (\lambda_x/z)^{1/2}$ relationship (that was predominant at low Reynolds numbers) bridges the two $\lambda_y \sim \lambda_x$ relationships observed at smaller ($\lambda_x, \lambda_y \sim \mathcal{O}(z)$) and larger ($\lambda_x, \lambda_y > \mathcal{O}(10z)$) length scales.

Understanding wall-incoherent structures using 2-D LCS

In order to gain clarity on the z-scaling of the wall-detached eddies, the 2-D linear coherence spectrum (LCS) ($\gamma^2_{L,2D}$) is computed using the DNS data of a channel at $Re_\tau = 934$ obtained from del Álamo *et al.* (2004). The 2-D LCS, computed for a pair of velocity signals measured simultaneously at wall-heights z and z_R, provides a scale-specific distribution of the amount of energy that is shared between the two signals (Baars *et al.*, 2016, Tinney *et al.*, 2006). The 2-D LCS is given by

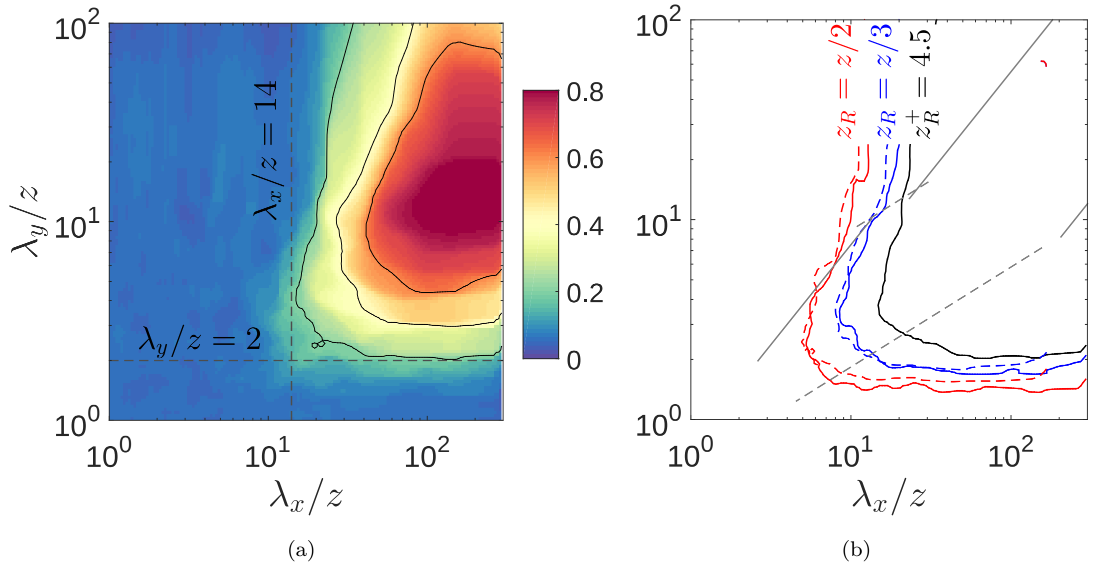

FIGURE 6.6: $\gamma^2_{L,2D}$ plots from Channel DNS at $Re_\tau = 934$; (a) $\gamma^2_{L,2D}$ distribution at $z^+ = 80 (= 2.6 Re_\tau^{1/2})$ and $z_R^+ = 4.5$ and (b) contours corresponding to $\gamma^2_{L,2D} = 0.2$ computed for various reference wall locations (z_R). The solid and dashed contour lines correspond to $z^+ = 80 (= 2.6 Re_\tau^{1/2})$ and $z^+ = 140 (= 0.15 Re_\tau)$ respectively. The grey lines correspond to the outline of 2-D spectra of u as shown in figure 6.4

$$\gamma^2_{L,2D}(z, z_R, \lambda_x, \lambda_y) = \frac{|\langle \hat{u}(z; \lambda_x, \lambda_y)\, \hat{u}^*(z_R; \lambda_x, \lambda_y)\rangle|^2}{\langle |\hat{u}(z; \lambda_x, \lambda_y)|^2\rangle \langle |\hat{u}(z_R; \lambda_x, \lambda_y)|^2\rangle}. \tag{6.6}$$

Here, $\hat{u}(z; \lambda_x, \lambda_y)$ is the coefficient of a 2-D Fourier transformation of the streamwise velocity u, while z and z_R denotes the measurement and reference wall-normal locations respectively.

Figure 6.6(a) shows the distribution of $\gamma^2_{L,2D}$ at $z^+ = 80 (= 2.6 Re_\tau^{1/2})$. The reference location is very close to the wall at $z_R^+ = 4.5$. The $\gamma^2_{L,2D}$ distribution shows the energetic scales at z which have a finite correlation at z_R and hence provides the range of scales that are coherent with respect to z_R. In this case, since z_R is very close to the wall, figure 6.6(a) indicates the range of scales at $z^+ = 80$ that are 'attached' to the wall. From figure 6.6(a), it can be observed that the coherent region is bounded by $\lambda_x/z \approx 14$ and $\lambda_y/z \approx 2$, and hence the most energetic scales would assume a streamwise/spanwise aspect ratio of $\lambda_x/\lambda_y \approx 7$. These numbers for the streamwise/wall-normal and streamwise/spanwise aspect ratios agree with Baars *et al.* (2017) and the results from the high-*Re* 2-D spectra discussed in the previous chapter, respectively. We also observe that the *large eddy region* where the $\lambda_y/z \sim (\lambda_x/z)^m$ relationship holds, and the 2-D spectrum modelled using attached eddies with matched aspect ratios (figure 6.4), are within these bounds of $\gamma^2_{L,2D}$. Therefore, the small-scale contributions outside these bounds of $\gamma^2_{L,2D}$, are from structures that are incoherent with $z_R^+ = 4.5$, and hence are 'detached' from the wall. A similar observation was reported by Baars & Marusic (2018*a*) at high Reynolds numbers using the 1-D LCS (figure 23).

To better understand the scaling of these wall-incoherent structures, consider figure 6.6(b). The black solid line represents the contour corresponding to $\gamma^2_{L,2D} = 0.2$, where $\gamma^2_{L,2D}$, as before, is computed with $z^+ = 80$ and $z_R^+ = 4.5$. Further, $\gamma^2_{L,2D}$ is computed keeping the $z^+ = 80$ and shifting the reference location to $z_R^+ = z^+/3 = 80/3$ and the contour corresponding to $\gamma^2_{L,2D} = 0.2$ is shown in figure 6.6(b) by the blue solid line. The range of scales in between the blue and black solid contours are those that are present at $z^+ = 80$ and are incoherent at the wall, while being coherent at $z^+/3$. The blue dashed line is obtained for a different measurement location (z^+) within the log region, where the reference location is again chosen such that $z_R^+ = z^+/3$. The collapse of the latter two contour lines gives evidence of the wall-scaling of energetic wall-detached motions. The same inference can be obtained when the reference location is fixed at $z_R^+ = z^+/2$ (red solid and dashed contours). A similar scaling of the two-point 2-D correlation of the wall-normal velocity component was reported by del Álamo *et al.* (2004).

6.2.3 Extended attached eddy model

In the previous section, based on scaling arguments, we identified three major contributors to the turbulent kinetic energy: (i) wall-coherent self-similar motions, (ii) wall-coherent very large scale motions and (iii) wall-incoherent wall-scaled motions. Here, we attempt to extend the attached eddy model by assigning representative geometries and organizations to the above identified sub-components, namely, *Type* A, *Type* SS and *Type* C_A respectively. Packet eddies constructed with Λ-hairpins, as detailed in §6.1, are used to represent *Type* A, *Type* SS and

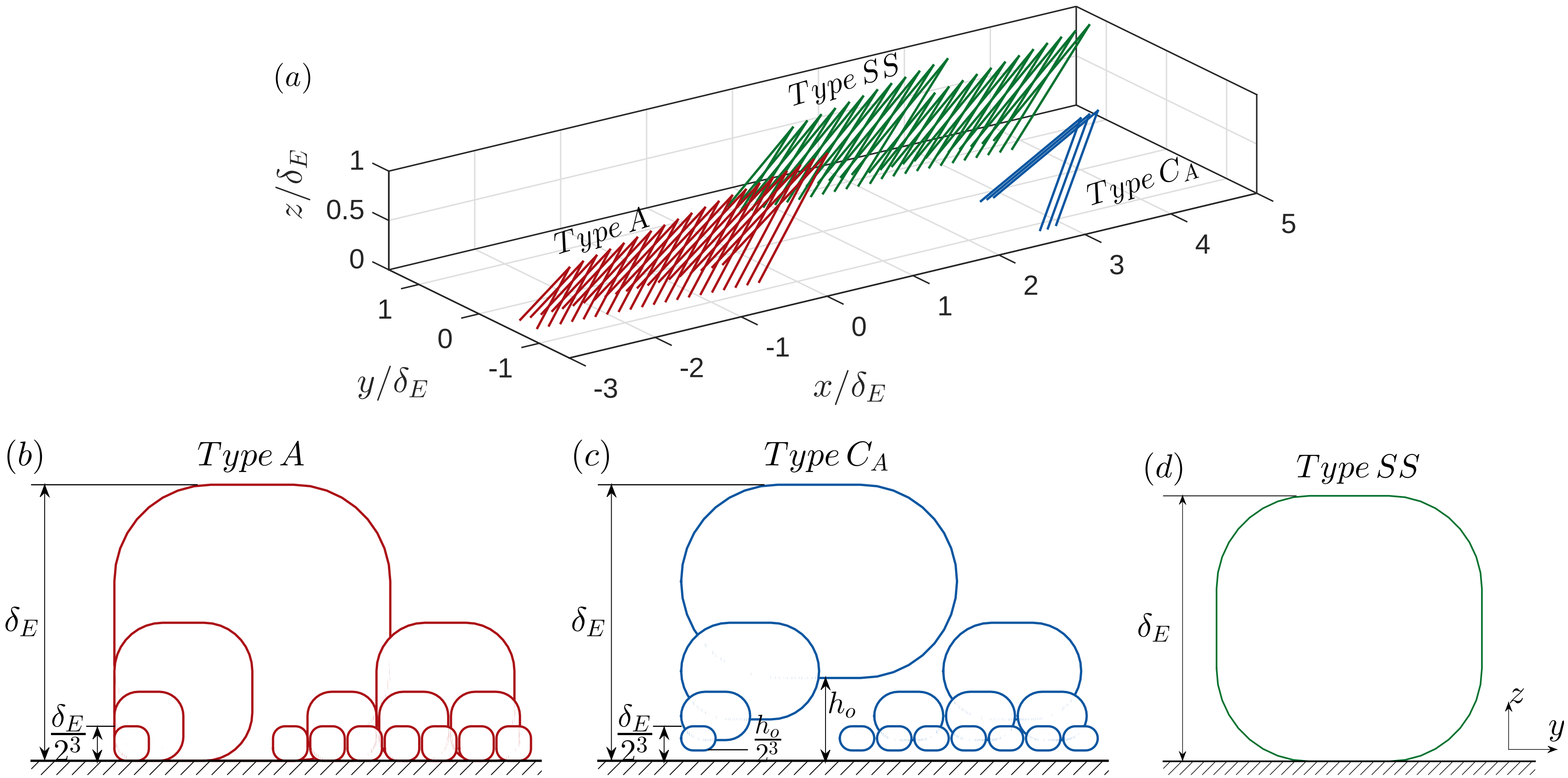

Figure 6.7: (a) Geometry of *Type A*, *Type* C_A and *Type SS* representative eddies considered in the study and (b,c,d) schematics showing the organization of *Type A*, *Type* C_A and *Type SS* eddies respectively. The largest *Type* C_A eddy ($\mathcal{H} \sim \delta_E$) is detached from the wall by h_o.

Type C_A motions (as shown in figure 6.7(a)). No other shapes for the hairpins are considered in the present study as we are interested in the scaling of representative packet eddies rather than focusing on the form of individual hairpins. The length ($\mathcal{L}$) and width ($\mathcal{W}$) of the packets are different for the three representative motions and are chosen based on the scaling of experimental 2-D spectra (as discussed in the following sections). The results obtained with *Type* A, *Type* SS and *Type* C_A structures are respectively colour-coded using shades of red, green and blue, and the results from the composite model are represented with shades of black.

6.2.3.1 *Type A*

Type A eddies represent the wall-attached self-similar motions as conceptualized by Townsend (Townsend, 1976). The geometry of the representative packet ($\mathcal{L}$ and $\mathcal{W}$) is chosen such that the aspect ratio, $\mathcal{L}/\mathcal{W}$, is equal to the average aspect ratio of the wall-coherent self-similar motions observed in experiments, which is $\lambda_x/\lambda_y \approx 7$. The boundary layer is then populated with hierarchies of representative packet eddies that belong to different stages of their self-similar growth (Perry *et al.*, 1986). For illustrative purposes, figure 6.7(b) represents a discrete model with four different hierarchies of *Type* A eddies; the sizes of the largest and the smallest eddies in the schematic being $\delta_E(\sim \mathcal{O}(\delta))$ and $\delta_E/2^3$ respectively. The curved boxes are illustrative of a cross-stream slice of the velocity field ($y-z$ plane) from the representative eddies and do not in any form represent the actual velocity field. Figure 6.7(b) is similar to the physical model of Perry *et al.* (1986) where the sizes of the representative eddies scale with the distance from the wall (z) and their probability density is inversely proportional to z. However, unlike in figure 6.7(b), the actual simulation assumes a continuous hierarchy of eddies with the heights of the largest and the smallest eddies being $\mathcal{H}_L = \delta_E$ and $\mathcal{H}_S^+ = 100$, respectively. Hence, the 2-D spectra resulting from this random distribution of self-similar eddies is computed using equaiton 6.2.

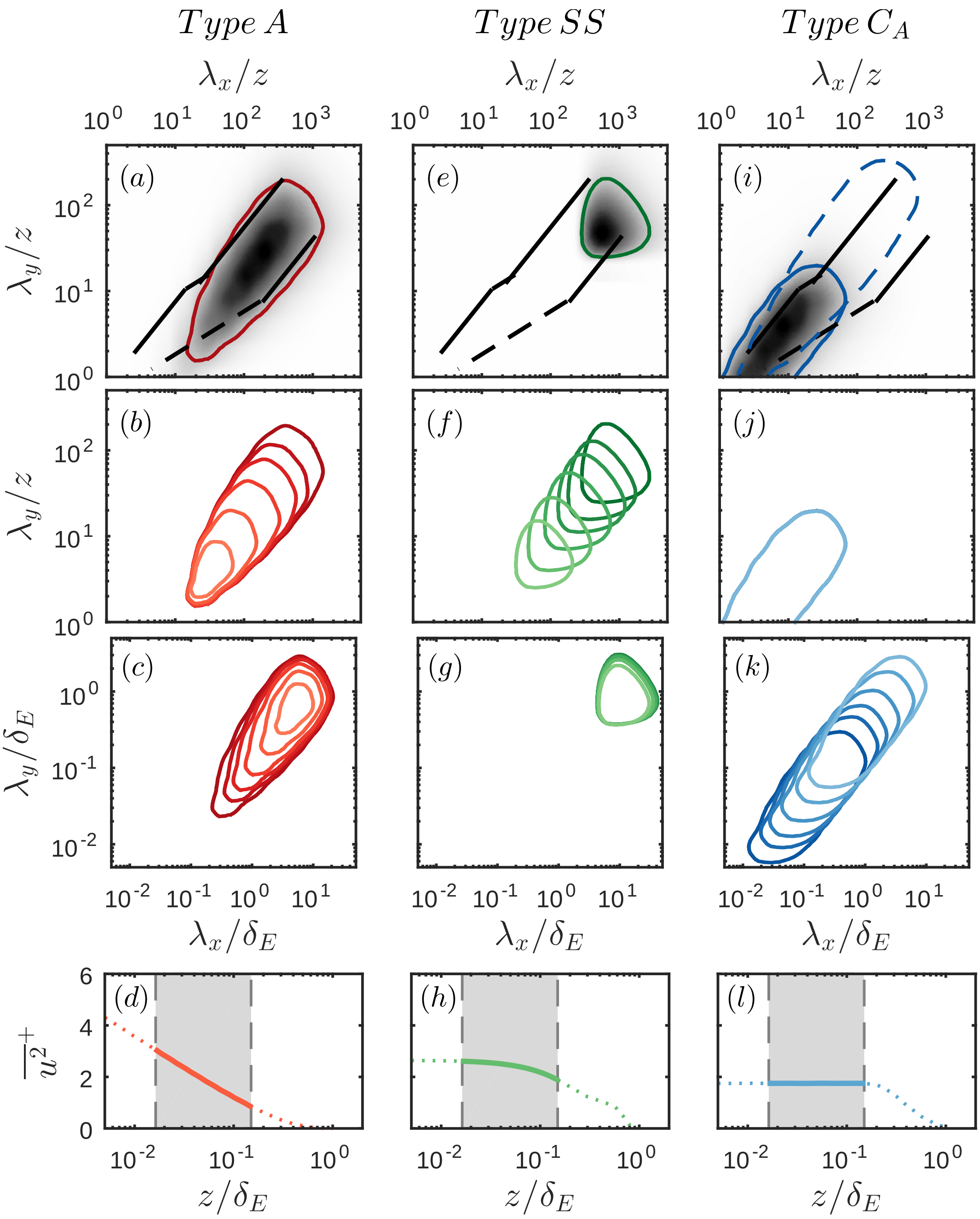

FIGURE 6.8: (a,e,i) 2-D spectra of u, (b,f,j) inner-flow scaling, (c,g,k) outer-flow scaling and (d,h,l) profile of turbulence intensity of *Type A*, *Type SS* and *Type* C_A representative eddies respectively. Line contours represent a constant energy of $\max(k_x k_y \phi_{uu}/U_\tau^2)/3$. Dark shade to light shade is $z/\delta = 2.6Re_\tau^{-1/2}$ to 0.15. The blue dashed and solid line contours in (i) are from $h_o/\mathcal{H} = 0$ (attached) case and $h_o/\mathcal{H} = 0.15$ case respectively. The black solid and dashed lines in (a,e,i) denote the $\lambda_y/z \sim \lambda_x/z$ and $\lambda_y/z \sim (\lambda_x/z)^{1/2}$ relationships respectively.

Figure 6.8(a) shows the 2-D spectrum of *Type A* eddies at $z^+ = 2.6Re_\tau^{1/2}$ for $Re_\tau = 26000$ (similar to figure 6.4(b)). The solid and dashed black lines represent $\lambda_y/z \sim \lambda_x/z$ and $\lambda_y/z \sim (\lambda_x/z)^{1/2}$ relationships respectively as observed in experiments. As discussed in §6.2.1, *Type A* eddies model the large scales reasonably well. Figures 6.8(b) and (c) show the inner-flow and outer-flow scaling, respectively, of contours of constant energy ($= \max(k_x k_y \phi_{uu}/U_\tau^2)/3$) within the logarithmic region, i.e. $2.6Re_\tau^{-1/2} \leq z/\delta \leq 0.15$. Representative of Townsend's attached eddies, *Type A* eddies follow both inner-flow and outer-flow scalings. Since the geometry of *Type A* eddies is selected based on experimental data, the *Type A* spectra have energy at $\lambda_x/z > 14$ and with decreasing wall-height, the spectra grows along $\lambda_x/\lambda_y \approx 7$. Now, considering the outer-scaling (when scaled in δ_E), the large scales collapse at $\lambda_x \approx 7\delta_E$ and $\lambda_y \approx \delta_E$, as in experiments. Figure 6.8(d) shows the wall normal profile of turbulence intensity ($\overline{u^2}^+$), which is obtained by integrating the 2-D spectrum along both the streamwise and spanwise length scales, i.e,

$$\overline{u^2}^+ = \int_0^\infty \int_0^\infty \frac{k_x k_y \phi_{uu}}{U_\tau^2} \, \mathrm{d}(\ln \lambda_x)\mathrm{d}(\ln \lambda_y). \tag{6.7}$$

Following from the attached eddy hypothesis, the turbulence intensity of *Type A* motions decay logarithmically with increasing wall-height.

6.2.3.2 *Type SS*

Type SS eddy is representative of the wall-coherent superstructures (Hutchins & Marusic, 2007*a*), also referred to as very large scale motions (Kim & Adrian, 1999) or the 'global' mode (del Álamo & Jiménez, 2003) that extends deep in the wall-normal direction. Following the notion of packets aligning in the streamwise direction to form longer structures (Kim & Adrian, 1999), the *Type SS* representative eddy is constructed by aligning two packets as shown in figure 6.7(a). The length ($\mathcal{L}$) of the eddy is the total length of the two smaller packets put together. The growth angle of each packet and the spacing of hairpins within the packet are consistent with the other representative eddies. Unlike the hierarchical structure of *Type A* and *Type* C_A eddies, as shown in figure 6.7, the *Type SS* eddy is organised as a single hierarchy with the height of the eddy $\mathcal{H} \sim \delta_E$, thereby making its contribution 'global' and non-self-similar with wall-height. $\mathcal{L}$ and $\mathcal{W}$ are chosen such that the energy contributed by *Type SS* motions is restricted only to the very large length scales (figure 6.8e). Following the discussion in §6.2.2.1, figure 6.8(g) shows that the energy contributed by the *Type SS* eddy is concentrated at the fixed outer-flow scaled wavelengths of $\lambda_x/\delta_E \approx 10$ and $\lambda_y/\delta_E \approx 1$, throughout the log region. Since no self-similar hierarchies are present, the constant energy contours obtained at different wall-locations within the log region do not show any scaling with z (figure 6.8f). A good collapse of the constant energy contours with outer-scaling followed by an almost flat profile of $\overline{u^2}^+$ as plotted in figure 6.8(h) (not perfectly flat due to the shape of the packet), implies a roughly constant energy contribution of *Type SS* structures within the logarithmic region.

6.2.3.3 *Type* C_A

In §6.2.2.1, we discussed that the wall-incoherent motions (*Type* C; Marusic & Monty, 2019) comprise of Kolmogorov-type fine scale turbulence and other wall-detached motions, some of which scale self-similarly with z. In the present study, we only model a subset of *Type* C motions, namely *Type* C_A, which represent structures that are physically detached from the wall but obey a distance from the wall scaling. The organization of *Type* C_A eddies in the boundary layer is illustrated in figure 6.7(c) with a discrete model, showing four different hierarchies. The sizes of the largest and the smallest eddies in the schematic are $\delta_E (\sim \mathcal{O}(\delta))$ and $\delta_E/2^3$ respectively, and are proportional to the distance from the wall. The separation from the wall of the largest eddy of size δ_E is h_o, and the separation of the smallest eddy of size $\delta_E/2^3$ is $h_o/2^3$, where, h_o is a fraction of $\mathcal{H}$. Since $\mathcal{H}$ scales with z, and $h_o/\mathcal{H}$ is a constant, h_o should also scale with z, i.e, the separations of the detached eddies from the wall also scales with z. Even though the legs of the hairpins of these eddies do not extend all the way to the wall, *Type* C_A eddies could be regarded as 'attached' in the sense of Townsend's attached eddy hypothesis, since their length scales relate to the distance from the wall (Marusic &

Monty, 2019). A similar organization was adopted for the *Type B* eddies of Perry & Marusic (1995) and Marusic & Perry (1995), in order to model the 'wake-structure' in the outer layer. The authors described the *Type B* eddies as 'attached-detached' structures due to their relation with the height above the wall.

For simplicity, a packet eddy with similar growth angle and hairpin-spacing as *Type A* and *Type SS* is considered for *Type* C_A as well. The dimension of the packet eddy ($\mathcal{L}$ and $\mathcal{W}$) and the separation from the wall (h_o), as shown in figure 6.7(a), are chosen such that the energy contribution from *Type* C_A eddies are concentrated at the smaller scales that followed the $\lambda_y \sim \lambda_x$ relationship as observed in experiments (§6.2.2.1). To illustrate the effect of offsetting eddies from the wall on the 2-D energy spectrum, we first consider a case with zero separation from the wall ($h_o/\mathcal{H} = 0$ typical of *Type A* organization). This is represented in figure 6.8(i) with the blue dashed line contour, which corresponds to a constant energy of $\max(k_x k_y \phi_{uu}/U_\tau^2)/3$. For $h_o/\mathcal{H} = 0$, at each wall-height z, the eddies of sizes $z \leq \mathcal{H} \leq \delta_E$ contributes to the turbulent kinetic energy. Hence the contour is observed to span a broad range of streamwise and spanwise length scales. Now if we consider a finite separation from the wall for the eddies, the 2-D spectrum shrinks to smaller values of λ_x/z and λ_y/z. The filled contour in figure 6.8(i) corresponds to a separation of $h_o/\mathcal{H} = 0.15$ and the solid blue contour correspond to a constant energy of $\max(k_x k_y \phi_{uu}/U_\tau^2)/3$. It is observed that in comparison to the no offset case, an offset of $h_o/\mathcal{H} = 0.15$ restricts the energy bounds to smaller scales that were expected to follow $\lambda_y/z \sim \lambda_x/z$ relationship as observed in experiments. Due to the separation, at each wall-height z, the energy has contributions from eddies with heights $\mathcal{H} \geq z$ and separations $h_o \leq z$. Such an organization would imply that at all wall-heights below the separation of the largest eddy, i.e, at all $z < 0.15\delta_E$, the energy contribution is always from a fixed number of hierarchies. Additionally, this would imply that when the length scales are normalized by the distance from the wall, z, the constant energy contours would collapse across all wall-heights within the logarithmic region (see figure 6.8(j)). Such constant energy contribution is also reflected in the wall-normal profile of $\overline{u^2}^+$ (shown in figure 6.8l) which is flat for $z < 0.15\delta_E$, i.e, for wall-heights smaller than the wall-normal

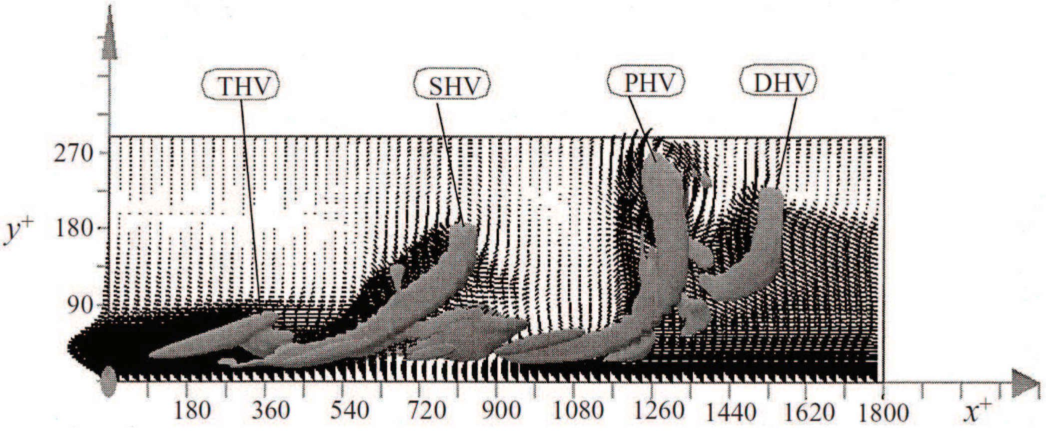

FIGURE 6.9: Figure 10(b) of Zhou *et al.* (1999) demonstrating the evolution of packet of hairpins.

separation of the largest eddy having $\mathcal{H} = \delta_E$. It is observed from figure 6.8(k) that the energy of the $Type\, C_A$ eddies do not scale in outer units and shifts to larger length scales while moving away from the wall.

Generation of $Type\, C_A$ motions

While the above arguments on the existence of wall-detached motions whose sizes scale with wall-height have been put-forth purely on the basis of mean two-point statistics, the dynamics that lead to the generation of such structures is unclear. Since AEM is purely kinematic, probing the generation of such structures is beyond the scope of this study. However, we would like to mention some previous studies which discuss mechanisms that could possibly lead to the formation of wall-scaled detached motions.

Marusic & Monty (2019) reports the possibility that such structures are the detached remnants of formerly attached eddies. Based on time-resolved PIV studies on evolving boundary layers, Lee (2017) discuss a shear driven mechanism that lead to the lift-up of attached eddies. The author observed that the faster convecting high-speed region interacts with the slower low-speed region, thereby forming a shear layer along their interface. The local instability induced along the interface was observed to cause the shear layer to roll-up and subsequently lift the low-speed region away from the wall (§8.4 in Lee, 2017).

While discussing the evolution of packets of hairpins in a turbulent field, Zhou *et al.* (1999) reports the formation of 'detached' hairpin vortices (DHV, as shown in figure 6.9), downstream of the primary hairpin vortex (PHV). They were observed to be generated as near-horizontal vortical 'tongues', sticking out of the primary vortices, which with time, rolled-up to form hairpin vortices. Similar downstream vortical 'tongues' were also observed by Jodai & Elsinga (2016), and they were reported to be the remnants of quasi-streamwise vortices, that are lifted up from the wall. Hence, with the notion of downstream detached hairpins 'sticking' to a packet of hairpins, we could expect self-similar hierarchies of 'detached' hairpin vortices to exist in boundary layers along with hierarchies of packet vortices. Such an organization could result in the wall-scaling of hairpins, even when they are physically detached from the wall.

6.2.3.4 Composite model

In the previous sections, three major spectral sub-components were identified based on the scaling of experimental 2-D spectra and they were associated with the three representative structures in the extended AEM: $Type\,A$, $Type\,SS$ and $Type\,C_A$. The geometry and the organization of these representative structures were selected based on arguments of scaling. Now, we calculate the composite 2-D spectra from the extended model as,

$$k_x k_y \phi^+_{uu,COMP} = \frac{(k_x k_y \phi_{uu,A} + W_{SS} \times k_x k_y \phi_{uu,SS} + W_{CA} \times k_x k_y \phi_{uu,CA})}{U^2_{\tau,COMP}} \qquad (6.8)$$

where,

$$U^2_{\tau,COMP} = \max(-\overline{uw}_{COMP}) \qquad (6.9)$$

and

$$\overline{uw}_{COMP} = \int\int_{-\infty}^{\infty} \Big((k_x k_y \phi_{uw,A} + W_{SS} \times k_x k_y \phi_{uw,SS} + W_{CA} \times k_x k_y \phi_{uw,CA}) \Big) \mathrm{d}(\ln \lambda_x)\mathrm{d}(\ln \lambda_y). \tag{6.10}$$

Here, $k_x k_y \phi_{uu,A}$, $k_x k_y \phi_{uu,SS}$, and $k_x k_y \phi_{uu,C_A}$ represent the 2-D spectrum of u from *Type* A, *Type* SS and *Type* C_A eddies respectively. W_{SS} and W_{CA} are the relative weightings for the energy contributions from *Type* SS and *Type* C_A eddies respectively, in relation to the energy contribution from *Type* A eddies (whose weighting is unity). Changing the values of W_{SS} and W_{CA} will change the shape of the composite 2-D spectrum and their values are chosen arbitrarily to match the composite 2-D spectrum with experiments (discussed in §6.2.4.1). It is to be noted that the objective of these weightings is not to match the magnitude of $k_x k_y \phi_{uu}/U_\tau^2$ with experimental values, but to get the distribution of energy among the right length scales, i.e, to get the correct shape of the 2-D spectrum. The composite friction velocity, $U_{\tau,COMP}$ is computed by forcing the inner-normalized peak Reynolds shear stress in the logarithmic region to be unity (Buschmann *et al.*, 2009), i.e, peak $-\overline{uw}^{+}_{COMP} = \max(-\overline{uw}_{COMP}/U^2_{\tau,COMP}) = 1$. As represented in equation 6.10, $\overline{uw}_{COMP}$ is computed by integrating the composite 2-D $uw-$spectrum across λ_x and λ_y. The same weightings (W_{SS} and W_{CA}) for the *Type* SS and *Type* C_A contributions, as in equation 6.8, are used in equation 6.10.

6.2.4 Results from the extended AEM

6.2.4.1 Spectra of u

Figure 6.10(a) and (b) show the 2-D spectra of u at $Re_\tau \approx 26000$ and $z^+ = 2.6Re_\tau^{1/2}$ from the experiments and the extended model respectively. The line contour represents $max(k_x k_y \phi^+_{uu}/4)$ and in figure 6.10(b), the contributions of *Type* A, *Type* SS and *Type* C_A eddies to the composite spectra is highlighted with red, green and blue coloured contours respectively. The values of W_{SS} and W_{CA} are

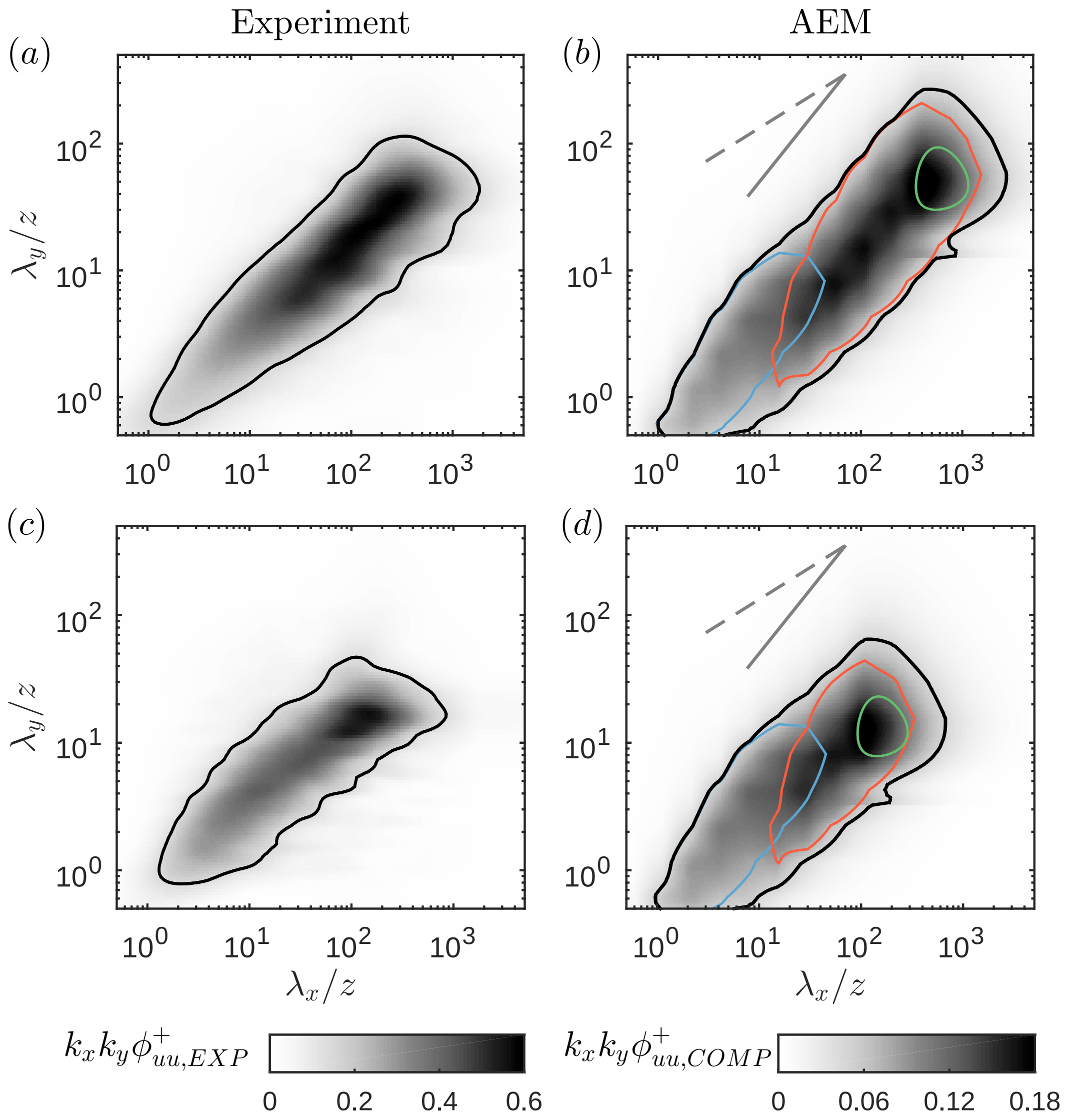

FIGURE 6.10: Comparison of 2-D spectra of u from the extended AEM with experiments at $z^+ = 2.6Re_\tau^{1/2}$ for (a,b) $Re_\tau \approx 26000$ and (c,d) $Re_\tau \approx 2400$. The line contour represents $\max(k_x k_y \phi^+_{uu})/4$. In (b,d) black, red, green and blue contours represent composite, *Type A*, *Type SS* and *Type* C_A spectra respectively and the grey solid and dashed lines are the references for $\lambda_y/z \sim \lambda_x/z$ and $\lambda_y/z \sim (\lambda_x/z)^{1/2}$ relationships respectively.

chosen to be 0.4 and 14 respectively, in order to match the shape of the composite 2-D spectrum with experiments. It is to be noted that these values for W_{SS} and W_{CA} are fixed for the representative structures considered in the present study and do not vary with respect to Reynolds numbers, wall-locations or the components of velocity. However, these values are specific for the current representative eddy (figure 6.7(a)) and would change with the shape of the hairpin, spacing between hairpins in a packet (Δx_p), strength of the vortex rods etc.

It is observed from figures 6.10(a) and (b) that the composite spectra obtained with the extended AEM is able to capture the major trends observed in the high-*Re* experimental 2-D spectra. While the conventional AEM (red contour in figure 6.10b), that comprises purely *Type A* eddies, represents only the large eddy region of the spectra, the extended model predicts a broader range of length scales. The $\lambda_y/z \sim \lambda_x/z$ behaviour observed at the smaller length scales in experimental spectra, is now captured using *Type* C_A eddies. The shape of the 2-D spectra at very large length scales is also made comparable with experiments by incorporating *Type SS* eddies. Interestingly, the length scales, where *Type* C_A and *Type A* spectra overlap, is observed to follow a near-square-root ($\lambda_y/z \sim (\lambda_x/z)^{1/2}$) behaviour. This agrees with experiments where the square-root relationship was observed to bridge the two $\lambda_y \sim \lambda_x$ relationships observed at smaller ($\lambda_x, \lambda_y \sim \mathcal{O}(z)$) and larger ($\lambda_x, \lambda_y > \mathcal{O}(10z)$) length scales, as discussed in §6.2.2.1.

We know that, contrary to high-*Re* spectra, the square-root relationship is predominant at low-*Re*, even at larger scales. Hence, the conventional AEM with *Type A* eddies alone does not predict the large-scales at low-*Re* (red line contour in figure 6.10d). Interestingly, since the extended AEM incorporates the low-*Re* characteristics with *Type* C_A contributions, a better prediction is observed even at low Reynolds numbers, as shown in figure 6.10(d). It is observed that at low Reynolds number ($Re_\tau \approx 2400$), the range of length scales for *Type A* is narrow compared to $Re_\tau \approx 26000$ and hence the scale separation between *Type* C_A and *Type SS* is less. Hence the *Type A*, *Type* C_A and *Type SS* energy spectra, all of which while individually follow a $\lambda_y/z \sim \lambda_x/z$ relationship, overlap at the larger length scales, resulting in a near-square-root ($\lambda_y/z \sim (\lambda_x/z)^{1/2}$) relationship as observed in experimental low-Reynolds number spectrum (figures 6.10c and d). The weaker *Type A* contribution at low-Reynolds numbers prohibits a transition of this square-root relationship to a $\lambda_y/z \sim \lambda_x/z$ trend, that was observed at high Reynolds numbers. The addition of *Type* C_A and *Type SS* contributions to the conventional AEM has enhanced its prediction capabilities while also making it a prospective candidate to model the log-region at low Reynolds numbers.

6.2.4.2 Inner-flow scaling of 2-D spectra of u

The inner-flow scaling of the composite 2-D spectra of u, obtained from the extended AEM, at $Re_\tau \approx 26000$ and computed at different wall-heights is shown in figure 6.11(b). The results are compared against the experimental spectra (figure 6.11a) at matched Reynolds number and wall-heights.

A good agreement is observed between figures 6.11(a) and (b) with the 2-D spectra showing a good collapse at the smaller streamwise and spanwise wavelengths ($\mathcal{O}(z)$ to $\mathcal{O}(10z)$), for the wall-heights considered. Figures 6.11(c) and (d) show that this collapse of the composite spectra can be attributed to the perfect inner-flow scaling of the $Type\, C_A$ spectra and the small-scale end of $Type\, A$ spectra. The Reynolds number invariance and hence the low-Re trend at the small scales is effected by $Type\, C_A$ contribution, which follows a $\lambda_y/z \sim \lambda_x/z$ relationship. Within the region of collapse, this linear growth is observed to transition towards a near-square-root $\lambda_y \sim \lambda_x^{1/2}$ behaviour when there is an overlap between $Type\, C_A$ and $Type\, A$ energies. Now, at wavelengths larger than $(\lambda_x, \lambda_y) \sim \mathcal{O}(10z)$ in the *large eddy region*, the spectra deviates from a pure z-scaling trend and moves towards the $\lambda_y/z \sim (\lambda_x/z)$ relationship, as observed in experiments. This transition towards a linear relationship in the *large eddy region* is dictated by $Type\, A$ energy (figure 6.11d) and therefore the $\lambda_y/z \sim (\lambda_x/z)$ scaling gets pronounced, due to the increasing contribution of $Type\, A$ to the energy, as we move closer to the wall (or increasing Re_τ as $z >> \nu/U_\tau$). It is to be noted that a peel-off from the perfect inner-scaling at the very small scales, due to the high-frequency Kolmogorov-type motions, is not observed in the model, since these scales are not included in the model.

Since 1-D streamwise spectra has been the popular tool to observe self-similarity, the composite 1-D streamwise spectra highlighting the contributions from $Type\, C_A$, $Type\, A$ and $Type\, SS$ eddies is shown as figures 6.11f-h respectively. Figures 6.11(f)-(h) are obtained by integrating figures 6.11(c)-(e) respectively, across the

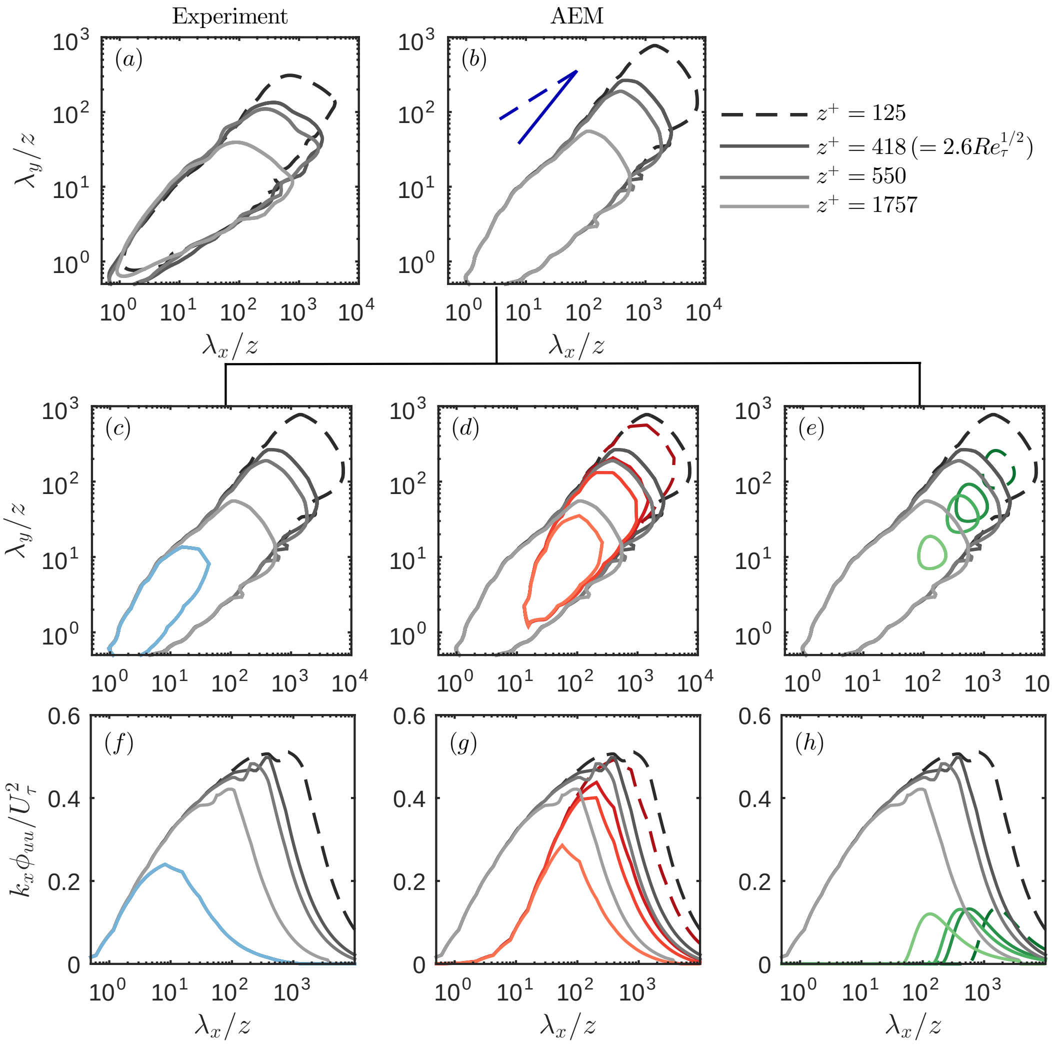

FIGURE 6.11: Inner-flow scaling of 2-D spectra of u: (a) Experiments at $Re_\tau \approx 26000$, (b) Composite spectra from the extended AEM at $Re_\tau \approx 26000$, (c,d,e) highlighting *Type* C_A (blue), *Type A* (red) and *Type SS* (green) contributions to the composite 2-D spectra (grey) and (f,g,h) highlighting *Type* C_A, *Type A* and *Type SS* contributions to the composite 1-D streamwise spectra. The line contours represent a constant energy of $\max(k_x k_y \phi^+_{uu}|_{z^+=125})/4$. The blue solid and dashed lines in (b) are the references for $\lambda_y/z \sim \lambda_x/z$ and $\lambda_y/z \sim (\lambda_x/z)^{1/2}$ relationships respectively.

whole range of spanwise length scales λ_y as:

$$k_x\phi^+_{uu}(k_x) = \int_0^\infty k_x k_y \phi^+_{uu}(k_x, k_y)\,\mathrm{d}(\ln\lambda_y). \tag{6.11}$$

Figures 6.11(f,g,h) are comparable with the triple-decomposed spectra of Baars & Marusic (2018*a*) (figure 15 (f,d,b) respectively) where the decomposition technique used empirically obtained coherence based filters. As observed by Baars &

Marusic (2018*a*), the maxima of the wall-incoherent small-scale (*Type* C_A) energy is located at $\lambda_x \sim \mathcal{O}(10z)$. Additionally, beyond $\lambda_x \sim \mathcal{O}(10z)$, the *Type* A spectra is observed to ramp-up with its amplitude increasing with decreasing wall-height. The ramp-up of the *Type* A spectra at its small-scale end appears to scale perfectly with z, which is in agreement with the empirical observation of Baars & Marusic (2018*a*). As indicated in figures 6.11(e) and (h), *Type* SS motions do not contribute to the wall-scaling of the composite spectra.

6.2.4.3 Outer-flow scaling of 2-D spectra of u

The outer-flow scaling of the composite 2-D spectra of u, obtained from the extended AEM, at $Re_\tau \approx 26000$ and computed at different wall-heights is shown in figure 6.12(b) and are compared against experiments (figure 6.12a).

As discussed in 5.6.2 and as observed in experiments, the composite 2-D spectra shows a good collapse at scales larger than $\lambda_x \approx 7\delta_E$ and $\lambda_y \approx \delta_E$ for all the wall-heights considered. At these large length scales, the collapse of the 2-D spectra in figures 6.12(d) and (e) is due to the perfect outer-scaled contributions from the *Type* SS and the large-scale end of *Type* A energy. The *Type* SS motions seem to capture the 'superstructure'-like characteristic of energy at very large streamwise wavelengths at an experimentally observed width of $\lambda_y \approx \delta$. However, the current model does not account for the reduction in very large scale energy below $z^+ = 2.6Re_\tau^{1/2}$ (as discussed in 5.6.2). Therefore, contrary to experimental observation, the constant energy contour from the AEM shows a perfect outer-flow scaling even at $z^+ = 125$. On the other hand, since the energetic ridges show a perfect collapse in outer-flow scaling even for $z^+ \approx 150$ in experiments, any conclusions from the model that are based on the energetic ridges (such as the slope of the 2-D spectra m) is expected to be unaffected for $100 \lesssim z^+ < 2.6Re_\tau^{1/2}$. Now, as observed in experiments, for $\lambda_x < 7\delta_E$ in the *large eddy region*, the constant energy contour deviates from a perfect outer-flow scaling while following the relationship of $\lambda_y/\delta \sim (\lambda_x/\delta)^m$. The value of m is observed to approach unity as we move closer to the wall (analogous to increasing Re_τ). From figures 6.12(c) and (d),

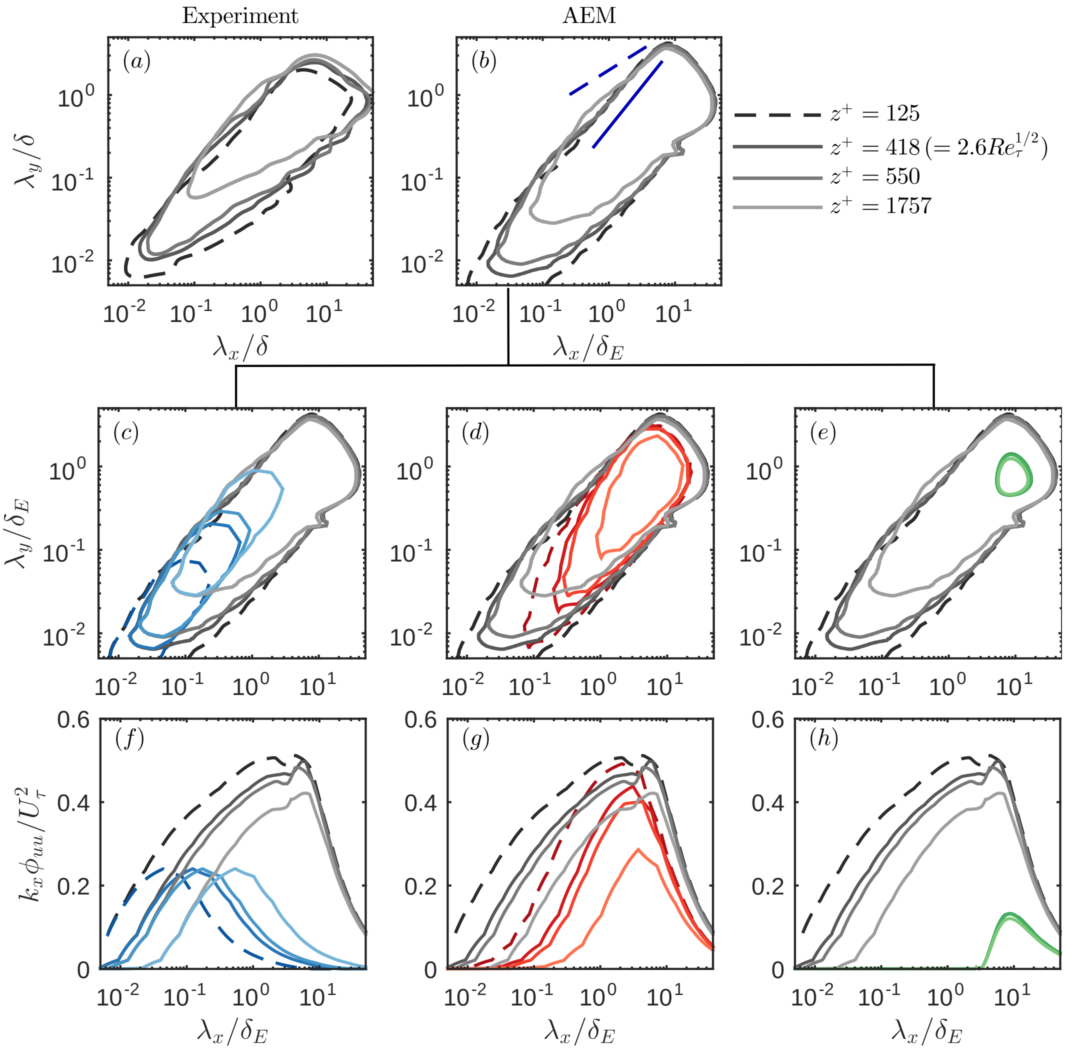

FIGURE 6.12: Outer-flow scaling of 2-D spectra of u when the wavelengths are normalized by the boundary layer thickness δ (in experiments) or the height of the largest eddy δ_E (in AEM). Details of the plots are the same as in figure 6.11.

we see that the trend towards $m = 1$ with decreasing z is due to the increased $Type\,A$ contribution and thus the increased scale separation between $Type\,SS$ and $Type\,C_A$ energies. An increased overlap between $Type\,A$ and $Type\,C_A$ energies results in the square-root relationship even when the individual spectra follows $\lambda_y \sim \lambda_x$.

The outer-flow scaled composite 1-D streamwise spectra highlighting the contributions from $Type\,C_A$, $Type\,A$ and $Type\,SS$ eddies is shown as figures 6.12f-h respectively. Figures 6.11(f,g,h) are comparable with the triple-decomposed spectra of Baars & Marusic (2018*a*) (figure 15 (e,c,a) respectively). As observed by Baars

& Marusic (2018*a*), the maxima of the wall-coherent very large scale (*Type SS*) energy is located at $\lambda_x \sim \mathcal{O}(10\delta_E)$. The roll-off at the large-scale end of *Type A* spectra is observed to follow a perfect outer-flow scaling in agreement to the empirical observation of Baars & Marusic (2018*a*) for $2.6Re_\tau^{1/2} \leq z^+ \leq 0.15\delta^+$. However, Baars & Marusic (2018*a*) show that the roll-off deviates from a perfect outer-flow scaling for $z^+ < 2.6Re_\tau^{1/2}$ in experiments due to the reduced energy contribution by the very large scale motions at such wall-heights. As indicated in figures 6.12(c) and (f), *Type* C_A motions do not contribute to the outer-flow scaling of the composite spectra.

6.2.5 Spectra of v and w

In the present study, the extension to the AEM was driven by the scaling of the 2-D spectra of the streamwise velocity u alone. Therefore, it is interesting to note that the extended model also gives good predictions for the spectra of the spanwise (v) and the wall-normal (w) velocity components as well, as shown in figure 6.13. Similar to the computation of the spectra of u using equation 6.8, the computation of the composite 2-D spectra of v and w can also be carried out. The values of W_{CA} and W_{SS} is taken to be the same as before. The results from the model are compared with the DNS of Lee & Moser (2015) at $Re_\tau = 5200$ (highest Re dataset available for 2-D spectra of v and w) in figure 6.13. It is seen from the DNS data that the peak energy in both v and w spectra, at this Reynolds number, are distributed across streamwise and spanwise length scales $\mathcal{O}(z)$. These energetic scales are resolved in the composite 2-D spectra of v and w and it is evident that *Type* C_A contribution dominates at these length scales. As observed by Baidya *et al.* (2017), the results from *Type A* eddies alone would represent dominant modes at much larger length scales, which would be valid only at very high Reynolds numbers.

At low Reynolds number ($Re_\tau = 2000$), Jiménez & Hoyas (2008) reported from their DNS of a channel flow that the energetic ridge of the 2-D spectra of v and w follow a $\lambda_y/z = \lambda_x/z$ relationship in the log region. However, from the data at

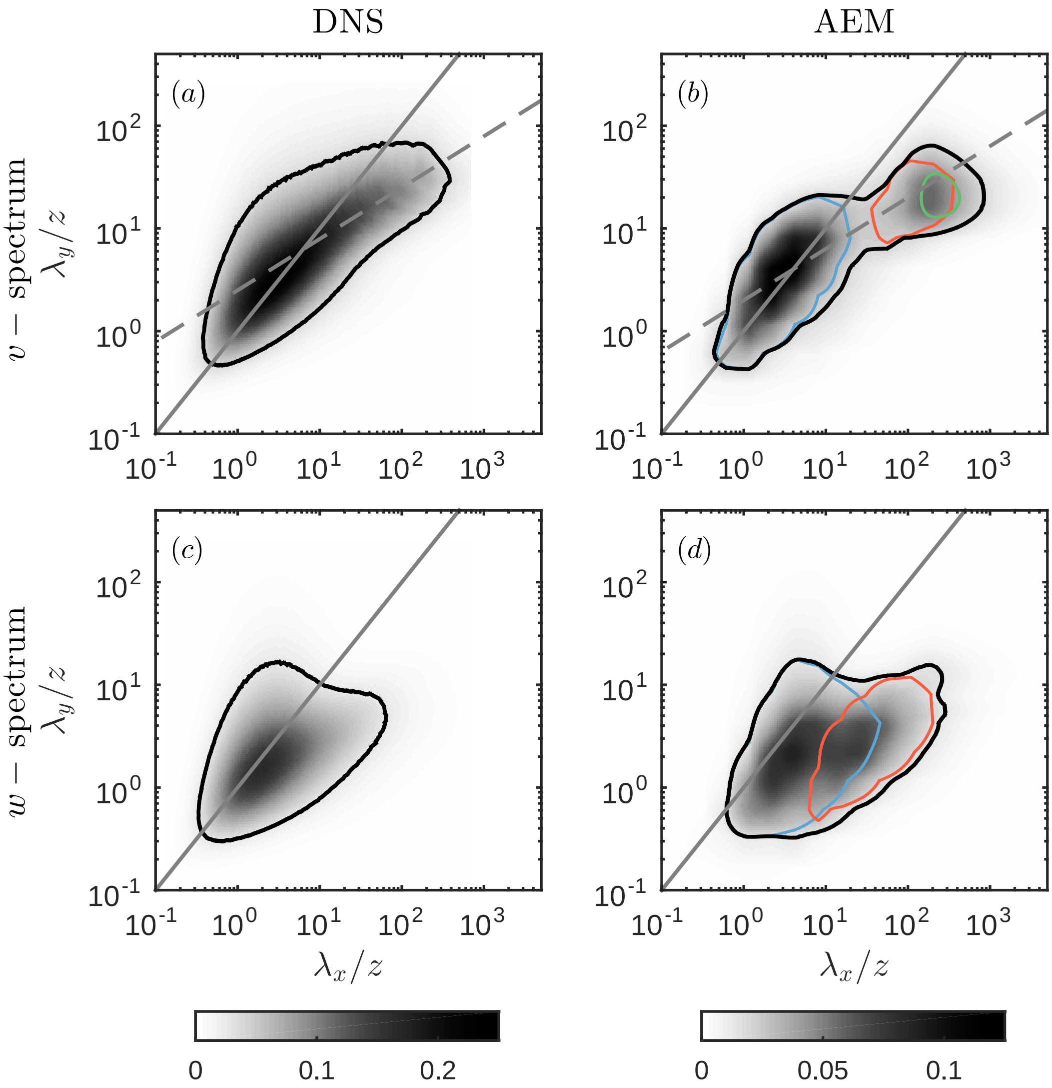

FIGURE 6.13: Comparison of the extended AEM with DNS of Lee & Moser (2015) at $z^+ = 2.6Re_\tau^{1/2}$. (a,b) Spectra of spanwise velocity (v) and (c,d) spectra of wall-normal velocity (w). The colour-coded line contours represent a constant energy of $\max(k_x k_y \phi^+)/6$. The grey solid and dashed lines denote $\lambda_y/z = \lambda_x/z$ and $\lambda_y/z \sim (\lambda_x/z)^{1/2}$ respectively.

higher Reynolds numbers ($Re_\tau = 5200$, DNS), we see that in the $v-$ spectra, above streamwise and spanwise scales $\mathcal{O}(10z)$, the $\lambda_y/z = \lambda_x/z$ relationship transitions to a square-root relationship of $\lambda_y/z \sim (\lambda_x/z)^{1/2}$, similar to the trend observed in the 2-D spectra of u. This trend is expected as $u-$ and $v-$ spectra follow similar scaling laws (Perry *et al.*, 1986). To understand this better, the inner-flow and outer-flow scaling of the composite 2-D spectra of v is plotted in figure 6.15 highlighting the contributions of *Type* C_A, *Type* A and *Type* SS eddies. The predominant low-Re trend of $\lambda_y/z = \lambda_x/z$ is due to the *Type* C_A contribution which scales perfectly

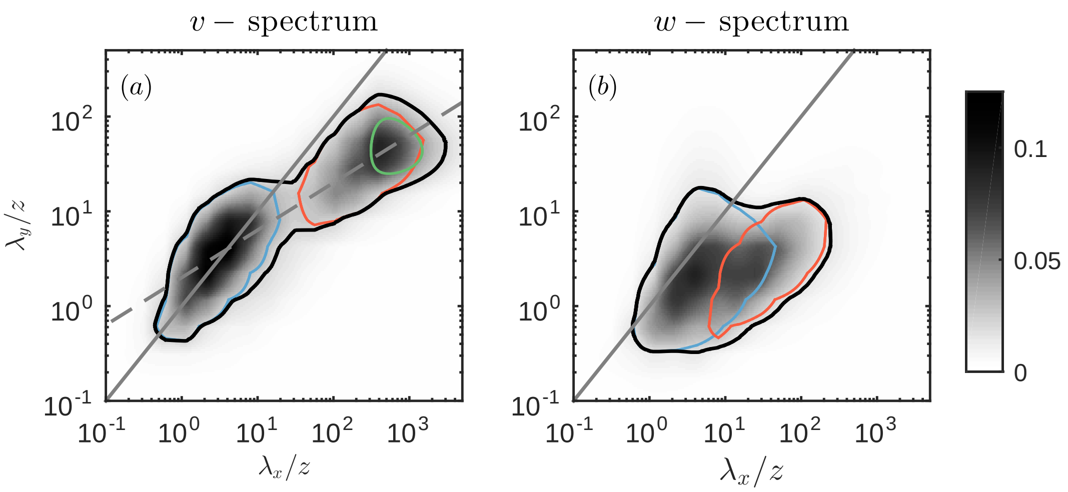

FIGURE 6.14: Predictions of (a) $v-$spectrum and (b) $w-$ spectrum from the extended AEM at $Re_\tau \approx 26000$ and $z^+ = 2.6Re_\tau^{1/2}$. The colour-coded line contours represent a constant energy of $\max(k_x k_y \phi^+)/6$. The grey solid and dashed lines denote $\lambda_y/z = \lambda_x/z$ and $\lambda_y/z \sim (\lambda_x/z)^{1/2}$ respectively.

with z. As observed for the $u-$spectra, the transition to a square-root relation appears to be at scales ($\mathcal{O}(10z)$) where the *Type* C_A and the *Type A* energies overlap. At even larger scales, the shape of the 2-D spectra is dictated by *Type A* energy which seem to gradually transition towards a $\lambda_y/z \sim \lambda_x/z$ relationship. However, the current Reynolds number is not high enough for the linear trend to be conspicuous and the observation of this trend requires the measurement of the 2-D $v-$ spectra at high Reynolds numbers (refer to figure 6.14 for the predictions of $v-$ and $w-$spectra from the extended AEM at $Re_\tau \approx 26000$).

Unlike the u and v components, only the heads of hairpins contribute to the w motions and therefore as we move towards the wall (and away from the hairpin head), the contributions to w approaches zero and motions get restricted to the wall-parallel plane. Therefore, at a particular wall-height z, only those eddies with heights $\mathcal{H} \sim z$ contribute to $w-$ spectra. Hence, as shown in figure 6.16, the $w-$ spectra follows a perfect inner-flow scaling (Baidya *et al.*, 2017, Perry *et al.*, 1986). This would also result in the outer-flow scaled 2-D $w-$ spectra to 'travel' along the $\lambda_y = \lambda_x$ line to larger streamwise and spanwise wavelengths with increasing wall-height (Jiménez & Hoyas, 2008), as shown in figures 6.16(e-h). Since *Type SS* eddies have heights $\mathcal{H} \sim \delta$, they do not contribute to the $w-$ spectra in the log region (figures 6.16d and h).

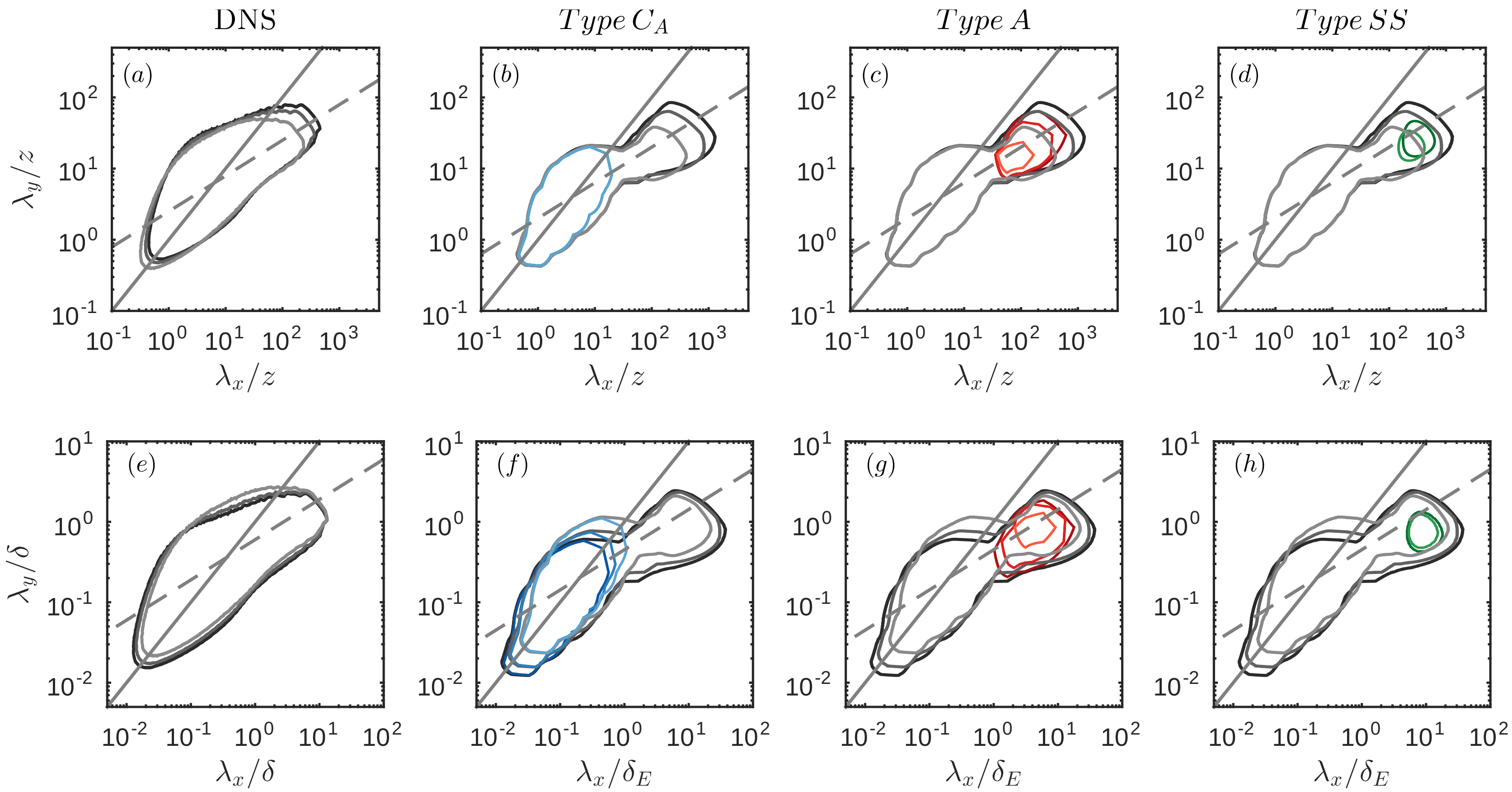

FIGURE 6.15: Inner-flow scaling (a-d) and outer-flow scaling (e-h) of 2-D spectra of v from DNS of Lee & Moser (2015) and AEM at $z^+ = 150$, $2.6Re_\tau^{1/2}$ and $3.9Re_\tau^{1/2}$ (dark to light shade respectively). The colour-coded line contours represent a constant energy of $\max(k_x k_y \phi^+_{vv}|_{z^+=150})/6$. The grey solid and dashed lines denote $\lambda_y = \lambda_x$ and $\lambda_y \sim (\lambda_x)^{1/2}$ respectively.

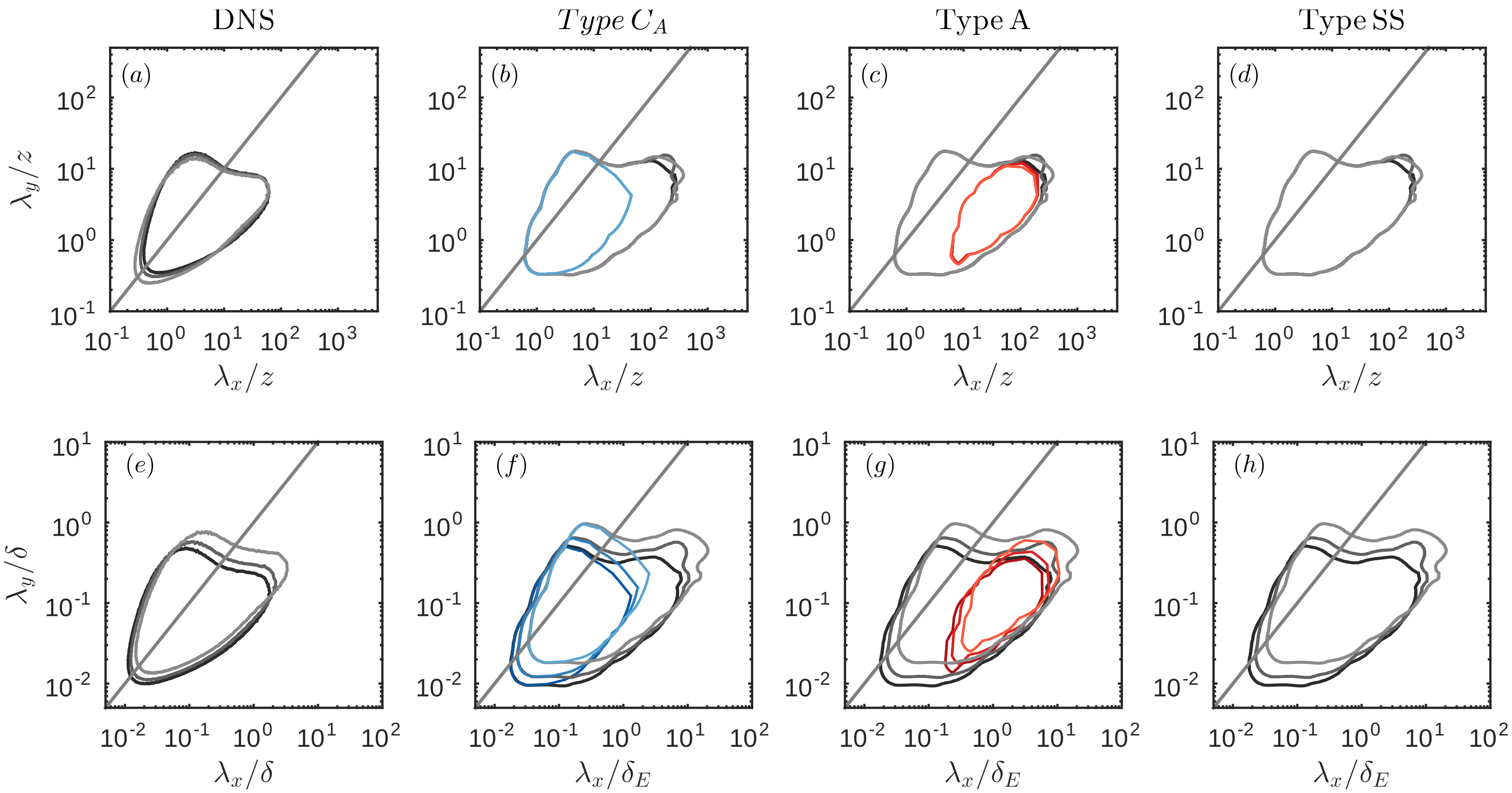

FIGURE 6.16: Inner-flow scaling (a-d) and outer-flow scaling (e-h) of 2-D spectra of w from DNS of Lee & Moser (2015) and AEM at $z^+ = 150$, $2.6Re_\tau^{1/2}$ and $3.9Re_\tau^{1/2}$ (dark to light shade respectively). The colour-coded line contours represent a constant energy of $\max(k_x k_y \phi^+_{vv}|_{z^+=150})/6$. The grey solid and dashed lines denote $\lambda_y = \lambda_x$ and $\lambda_y \sim (\lambda_x)^{1/2}$ respectively.

While the current model, which is developed based on the scaling of the $u-$ spectra, captures the key scaling arguments of the $v-$ and the $w-$ spectra, we note that further modifications are required to better model the 2-D spectra of all components of velocity. For example, tuning the shape of the hairpins could possibly resolve the bimodal nature of the $v-$ spectra. However, such refinements would require 2-D spectra of v and w at high Reynolds numbers.

6.2.6 Discussion on spectral self-similarity based on the extended AEM

In chapter 5, we observed that the slope (m) of the 2-D Spectra of u, which is also equal to the ratio of the plateau in the 1-D streamwise spectra of u to the plateau in the 1-D spanwise spectra of u, is a good indicator of self-similarity. The value of m was found to monotonically increase with Reynolds number, and it is important to understand the key mechanism that drives this trend of m. To this end, a kinematic perspective on the trend of m with Re_τ, or in general, the trend towards self-similarity with increasing Reynolds numbers is discussed in this section using the extended AEM.

Figure 6.17(a) shows the plot of $m = A_{1x}/A_{1y}$ vs Re_τ at $z^+ \approx 150$ from both experiments and the extended AEM. The results from the model follow the empirically observed Reynolds number trend reasonably well. We note that the values are slightly over predicted at low Reynolds numbers while matching well with experiments for $Re_\tau \gtrsim 10^4$. Agreeing with the empirical fit, the value of m obtained from the model is observed to approach unity at $Re_\tau \approx 60000$. In order to understand this Reynolds number trend, we analyze the 2-D spectrum with the associated 1-D streamwise and spanwise spectra at $Re_\tau = 2400$ ($m \approx 0.5$) and $Re_\tau = 60000$ ($m = 1$), obtained from the extended model, shown in figures 6.17(b) and (c), respectively. The contributions of $Type\,A$, $Type\,C_A$ and $Type\,SS$ eddies are highlighted and colour-coded in the figure. The plateaus in the streamwise and spanwise spectra, A_{1x} and A_{1y}, are also highlighted.

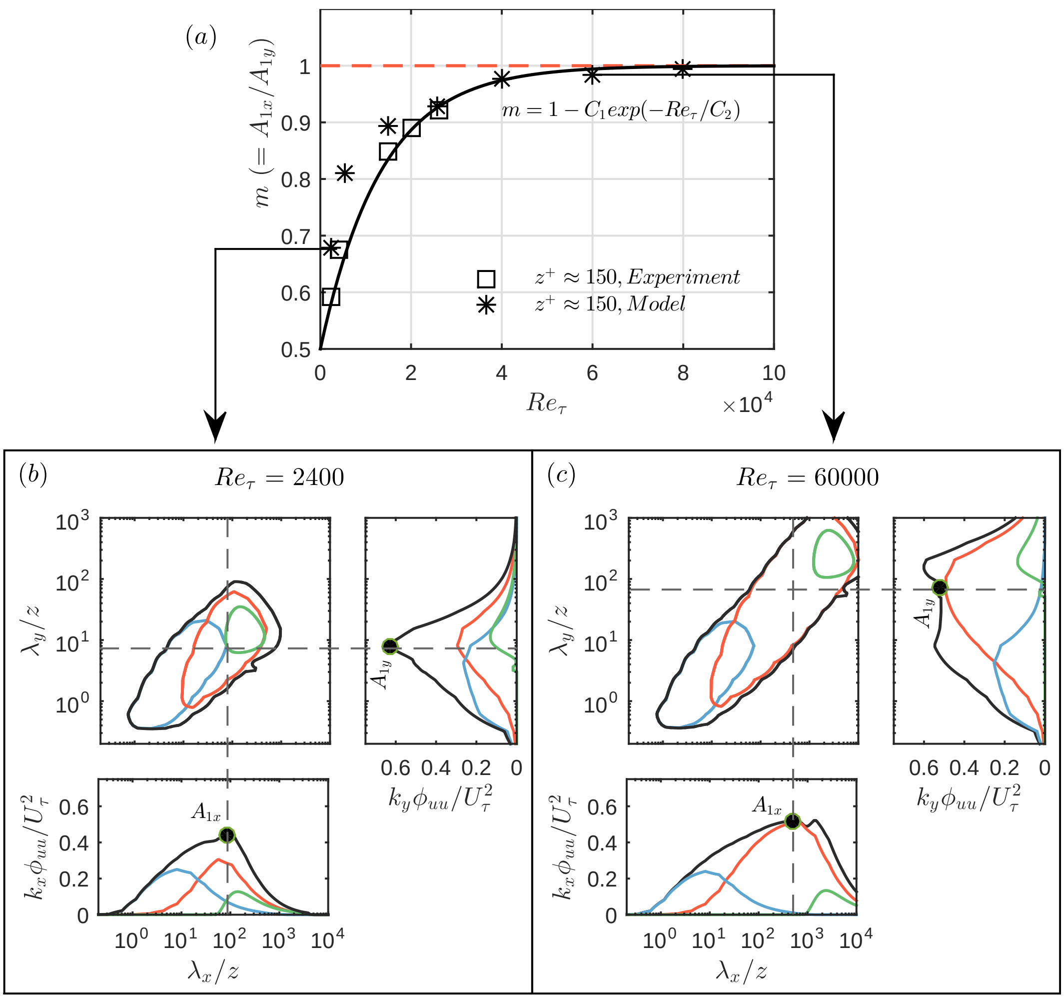

FIGURE 6.17: (a) Variation of m versus Re_τ at $z^+ \approx 150$ from experiments and extended AEM, (b) and (c) 2-D spectrum and the associated 1-D spectra at $Re_\tau = 2400$ and $Re_\tau = 60000$, respectively, from the model. The energy contribution of $Type\,C_A$ (blue), $Type\,A$ (red) and $Type\,SS$ (green) motions are plotted in (b) and (c).

At $Re_\tau = 2400$ (figure 6.17b), there is less scale separation between the largest ($Type\,SS$) and the smallest ($Type\,C_A$) energetic motions which result in an overlap of the energy contributions from $Type\,C_A$, $Type\,A$ and $Type\,SS$ eddies for $\lambda_x > \mathcal{O}(10z)$ and $\lambda_y > \mathcal{O}(z)$. As discussed in 6.2.4.1, the $\lambda_y/z \sim (\lambda_x/z)^{1/2}$ relationship ($m = 0.5$) at such length scales is observed to be an artefact of the overlap of sub-component energies. The 1-D streamwsie and spanwise spectra are obtained by integrating the 2-D spectrum as given in equation 4.3. Therefore, the plateaus in the 1-D streamwise and spanwise spectra, A_{1x} and A_{1y} respectively, are obtained by integrating the 2-D spectrum along the vertical and the horizontal dashed lines shown in figure 6.17(b). We note that, at $Re_\tau = 2400$, A_{1x} and A_{1y}

have contributions from all three spectral subcomponents: $Type\,C_A$, $Type\,A$ and $Type\,SS$. Since $Type\,C_A$ energy diminishes beyond $[\lambda_x/z, \lambda_y/z] \sim 10$, its contribution to A_{1x} at $\lambda_x/z \sim 100$ is from its roll-off, and therefore is relatively low. However, for the plateau in the spanwise spectra A_{1y}, which is at $\lambda_y/z \sim 10$, the contribution of $Type\,C_A$ is high and in proportion to that of $Type\,A$. Since $Type\,A$ and $Type\,SS$ contribute similarly to A_{1x} and A_{1y}, the increased contribution from $Type\,C_A$ to A_{1y} results in $A_{1y} > A_{1x}$ and therefore, $m < 1$.

The scale separation between the largest and the smallest scales increases with Reynolds number. Referring back to figure 6.8, $Type\,C_A$ and the small-scale end of $Type\,A$ follow perfect inner-flow scaling while $Type\,SS$ and the large-scale end of $Type\,A$ follow outer-scaling. Therefore, with increasing Reynolds number (or decreasing z/δ), $Type\,SS$ spectra and the large-scale end of $Type\,A$ spectra shift to larger λ_x/z and λ_y/z. As seen from figure 6.17(c), at $Re_\tau = 60000$, $Type\,C_A$ and $Type\,SS$ spectra are completely separated from each other at the wavelengths corresponding to the location of A_{1x} and A_{1y} ($\lambda_x/z \approx 500$ and $\lambda_y/z \approx 70$ respectively). As a result, at this Reynolds number, only the wall-coherent self-similar $Type\,A$ motions (spectra in red) contribute to the plateaus in the streamwise and the spanwise spectra. In other words, A_{1x} and A_{1y} would also correspond to the plateaus in the 1-D $Type\,A$ spectra. (For clarity, refer to figure 6.18 which shows the variation of A_{1x} versus Re_τ. As observed in figures 6.11 and 6.12, the peak of $Type\,A$ energy spectra increases with Re_τ and would mature to a plateau only after $Re_\tau \approx 60000$.) Hence, from figure 6.17(c), $\lambda_x/z \approx 500$ and $\lambda_y/z \approx 70$ would represent the length scales at which a true k^{-1} scaling would commence in a 1-D streamwise and 1-D spanwise spectra respectively. Even though a true k^{-1} scaling kicks in at $Re_\tau \approx 60000$, a decade of k^{-1} scaling may be revealed only at ultra high Reynolds numbers.

The predictions from the model at asymptotic high Re_τ ($\mathcal{O}(10^6)$) is shown in figure 6.19. A decade of k^{-1} scaling is evident in both streamwise and spanwise spectra. The small-scale bound of the k^{-1} region corresponds to the scales where the 'large-scale roll-off' from $Type\,C_A$ energy ends. Since the roll-off scales perfectly with z, the k^{-1} region begins at fixed inner-scaled wavelengths, G_{1x} and

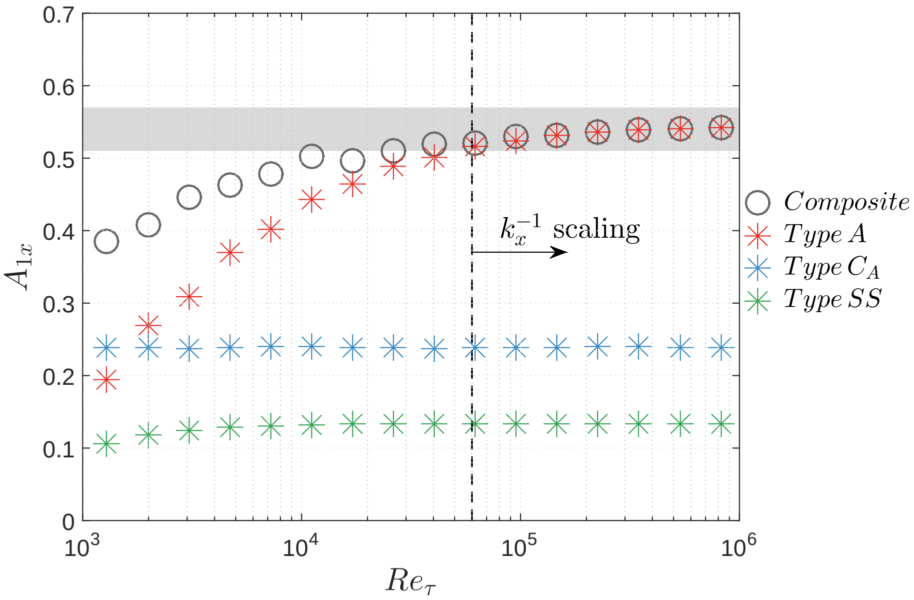

FIGURE 6.18: Variation of A_{1x} versus Re_τ at $z^+ \approx 150$ from the extended AEM. A_{1x} is computed from the composite, *Type A*, *Type* C_A and *Type SS* 1-D streamwise spectra. The grey patch represents $A_{1x}|_{Re_\tau \sim 10^6} \pm 5\%$.

G_{1y} respectively in the 1-D streamwise and spanwise spectra. Based on the results from the extended AEM, these bounds are estimated to be $\lambda_x/z = G_{1x} \approx 500$ and $\lambda_y/z = G_{1y} \approx 70$ respectively. The limit in the streamwise spectra agrees with Baars & Marusic (2018*a*), who estimated $G_{1x} \approx 385$. Similarly, the large-scale bound of the k^{-1} region corresponds to the scales where the 'small-scale roll-off' from *Type SS* energy ends. Since the roll-off scales with δ_E, the k^{-1} region at the large-scales would be bounded by fixed outer-scaled wavelengths, G_{2x} and G_{2y} respectively in the 1-D streamwise and spanwise spectra. From figure 6.19, these bounds are estimated to be $\lambda_x/\delta_E = G_{2x} \approx 2$ and $\lambda_y/\delta_E = G_{2y} \approx 0.3$ respectively. Therefore, a decade of k_x^{-1} scaling would require $G_{2x}(z/\delta_E)^{-1}/G_{1x} \sim 10$, and a decade of k_y^{-1} scaling would require $G_{2y}(z/\delta_E)^{-1}/G_{1y} \sim 10$, or in both cases, $z/\delta_E \sim 10^{-4}$ (figure 6.19).

We note that the conclusions from the current model are based on a perfect outer-flow scaling of *Type SS* energy. The work of Baars & Marusic (2018*a*) reports very large scale energy contribution to have a subtle trend with Reynolds number. The authors, however, report the trend to be weaker than the previous raw spectra based observations (Hutchins & Marusic, 2007*a*, Vallikivi *et al.*, 2015*a*,*b*). Even

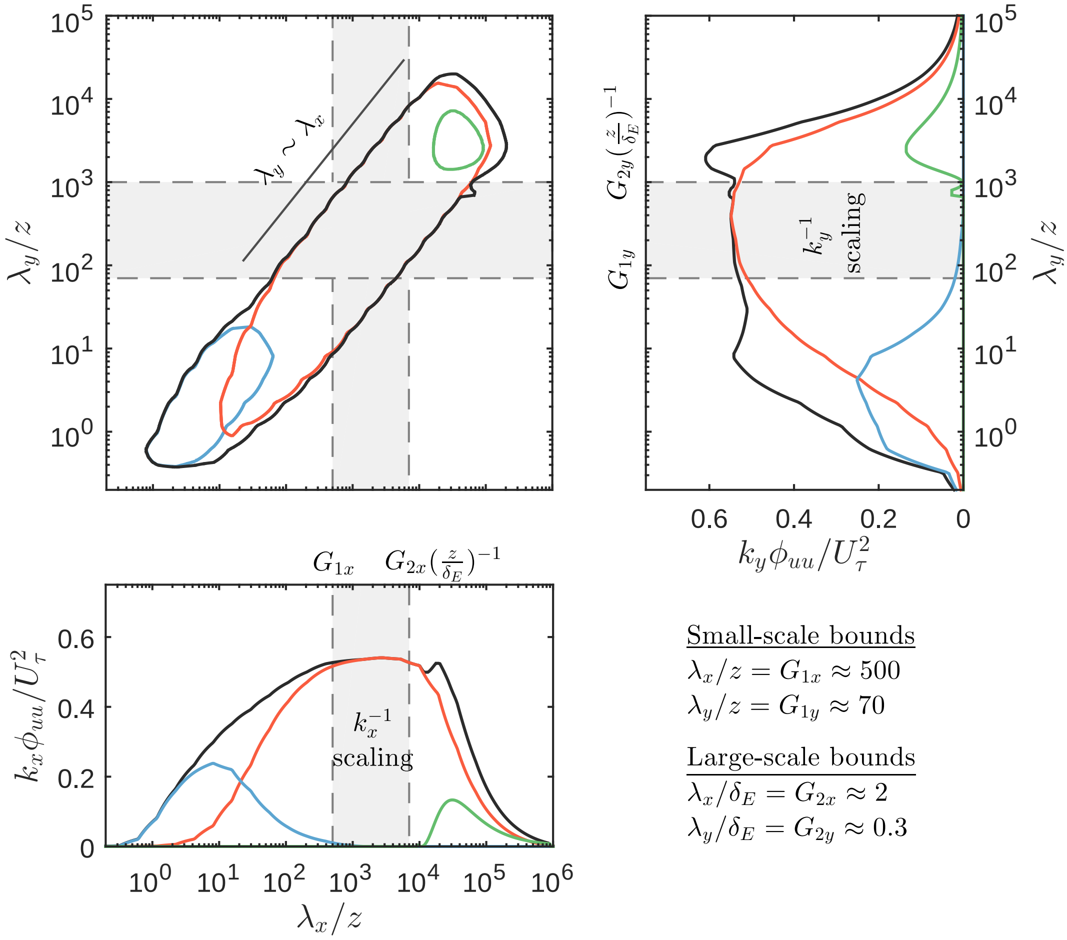

FIGURE 6.19: Spectra of u at asymptotic high Reynolds number ($\mathcal{O}(10^6)$, $z/\delta_E \sim 10^{-4}$) highlighting a decade of k^{-1} plateau in both streamwise and spanwise spectra. The small-scale and large-scale bounds of the k^{-1} region is indicated in the plots. The energy contribution of *Type* C_A (blue), *Type A* (red) and *Type SS* (green) motions are highlighted

though the trend appears to be less significant within the log region $2.6Re_\tau^{1/2} \leq z^+ \leq 0.15Re_\tau$, the asymptotic predictions would require clarity on the outer-flow scaling arguments of very large scale motions. This would further require high Reynolds number measurements resolving the largest scales, along with a reliable tool capable of isolating the very large scale motions from the rest of the spectra.

6.3 Chapter summary

The 2-D energy spectra obtained from the AEM is presented in this chapter. In §6.1, the details of the model along with the 2-D spectra obtained purely from wall-attached self-similar eddies ($Type\,A$) is discussed. At high Reynolds numbers, $Type\,A$ eddies with an aspect ratio of $\mathcal{L}/\mathcal{W} \sim \lambda_x/\lambda_y \approx 7$ is observed to represent the *large eddy region* of the experimental spectra reasonably well. However, the energy left unresolved by these $Type\,A$ eddies is found to be significant enough to dictate the trends of the 2-D spectra at low to moderately high Reynolds numbers.

In §6.2, the AEM is extended by identifying, and incorporating into the model, two types of structures that are major contributors to the turbulent kinetic energy in the log region: wall-incoherent structures that scale with z ($Type\,C_A$) and wall-coherent very large scale motions ($Type\,SS$). The geometry and the organization of these representative structures within the boundary layer are chosen based on the scaling arguments of $u-$spectra that are derived from experiments. In comparison to the conventional AEM, the spectra of all three velocity components obtained from the extended AEM are found to follow the empirically observed scaling laws, across a greater range of length scales ($\mathcal{O}(z)$ to $\mathcal{O}(10\delta)$). The model captures the empirically observed shift of the large scale behaviour, from a $\lambda_y \sim \lambda_x^{1/2}$ relationship towards a $\lambda_y \sim \lambda_x$ relationship, with increasing Reynolds number. Based on the extended model, a true k^{-1} scaling can be expected in the 1-D streamwise and spanwise spectra only at $Re_\tau \gtrsim 60000$, when a complete scale-separation exists between the δ-scaled $Type\,SS$ and the z-scaled $Type\,C_A$ energies.

Chapter 7

Conclusions

7.1 Summary and conclusions

In this thesis, we presented the two-dimensional spectra of streamwise velocity in the logarithmic region of turbulent boundary layers. The acquired dataset is unique for the Reynolds number range ($2400 \leq Re_\tau \leq 26000$) considered. A 2-D dissemination of energy across the broad range of streamwise and spanwise length scales (λ_x and λ_y) enabled identifying the key scale-specific Reynolds number trends, including the trend towards self-similarity of a Reynolds number dependent subrange of scales. The 2-D spectrum isolated the self-similar scales from the broadband turbulence, even while any evidence on self-similarity remained inconclusive in the associated 1-D spectra. Further, the scaling trends discerned from the 2-D spectra facilitated an extension of Perry and Chong's (1982) attached eddy model. The key findings of the present study are consolidated here.

7.1.1 Measurement of 2-D spectra

A novel experimental technique is presented to measure the 2-D energy spectra of the streamwise velocity in turbulent boundary layers. The technique is designed envisaging high Reynolds number measurements. It employs multiple hot-wire sensors that are sampled simultaneously for different spanwise spacings. Taylor's frozen turbulence hypothesis is used to convert temporal-spanwise information into a 2-D correlation, as a function of streamwise and spanwise distances, and subsequently the 2-D energy spectra, as a function of streamwise and spanwise wavelengths. Results were validated against the statistics computed from the DNS database of Sillero *et al.* (2014), at $Re_\tau \approx 2000$. This comparison revealed the importance of the initial spacing between the hot-wires and its detrimental impact on resolving the small scale region of the 2-D energy spectra. To account for this, a correction scheme based on the available DNS database is outlined. Collectively, the proposed experimental technique and the correction scheme, laid the foundation for measurements of the 2-D energy spectra of the streamwise velocity at higher Reynolds numbers.

7.1.2 Evidence of self-similarity from the 2-D spectra

Two-dimensional (2-D) spectra are measured in the logarithmic region across a decade of Reynolds numbers ($Re_\tau \approx 2400 - 26000$) and presented in chapter 5. While the small-scale contributions are found to be universal when scaled in viscous units, the large-scale contributions show a clear Reynolds number trend. Specifically, the contours of the 2-D spectra for large streamwise and spanwise wavelengths (referred to as the *large eddy region*) are observed to tend towards a $\lambda_y \sim \lambda_x$ relationship with increasing Reynolds number, starting from a $\lambda_y/z \sim (\lambda_x/z)^{1/2}$ behaviour observed at the lowest Reynolds number measured. It should be noted that the $\lambda_y \sim \lambda_x$ relation indicates self-similarity (i.e. the range of scales with an equal energetic contribution to the streamwise velocity maintain a constant aspect ratio λ_x/λ_y), while the lower Reynolds number $\lambda_y/z \sim (\lambda_x/z)^{1/2}$ behaviour is indicative of structures growing faster in the x direction compared to y. The average aspect ratio of the range of self-similar scales in the *large eddy region* is observed to be $\lambda_x/\lambda_y \approx 7$.

A simple model that describes the 2-D spectral contributions from the large-scales as a region of constant energy bounded by $\lambda_y/z \sim (\lambda_x/z)^m$ is presented in chapter

5. Here the power law coefficient 'm' corresponds to the slope of the constant energy bounds of the 2-D spectra at large scales, or equivalently, the ratio between the constant energy plateaus in 1-D pre-multiplied spectra in the streamwise and spanwise directions. The power law coefficient is proposed to be an effective indicator of self-similarity, and empirical evidence for m monotonically approaching unity with an increase in Reynolds number is presented. A true k^{-1} scaling in the 1-D spectra requires perfect inner-flow and outer-flow scalings of the 2-D spectra in the *large eddy region*, which further requires the value of m to be unity.

7.1.3 Model of the logarithmic region

The 2-D spectra obtained from the attached eddy model (AEM) of Perry & Chong (1982) and Perry *et al.* (1986) are compared against the experimental spectra in chapter 6. At high Reynolds numbers, with a careful selection of wall-attached self-similar eddies ($Type\,A$) with an aspect ratio of $\mathcal{L}/\mathcal{W} \sim \lambda_x/\lambda_y \approx 7$, the AEM represented the *large eddy region* of the experimental spectra reasonably well. However, the energy left unresolved by these $Type\,A$ eddies is found to be significant enough to dictate the trends of the 2-D spectra at low to moderately high Reynolds numbers.

Therefore, the conventional AEM is extended by identifying, and incorporating into the model, two types of structures that are major contributors to the turbulent kinetic energy in the log region: wall-incoherent structures that scale with z ($Type\,C_A$) and wall-coherent very-large-scale (superstructure) motions ($Type\,SS$). The geometry and the organization of these representative structures within the boundary layer are chosen based on the scaling arguments, of the 2-D spectra of u, that are derived from experiments. In comparison to the conventional AEM, the spectra of all three velocity components obtained from the extended AEM are found to follow the empirically observed scaling laws, across a greater range of length scales ($\mathcal{O}(z)$ to $\mathcal{O}(10\delta)$). The model captures the empirically observed shift of the large scale behaviour, from a $\lambda_y \sim \lambda_x^{1/2}$ relationship towards a $\lambda_y \sim \lambda_x$ relationship, with increasing Reynolds number. Based on the extended model, a true k^{-1} scaling can be expected in the 1-D streamwise and spanwise spectra only at $Re_\tau \gtrsim 60000$, when a complete scale-separation exists between the δ-scaled $Type\,SS$ and the z-scaled $Type\,C_A$ motions.

7.2 Suggestions for future work

A few suggestions for possible extensions to the current work include the following.

(*i*) **Experiments at higher Re_τ.** Th current results indicate that $Re_\tau \gtrsim 60000$ is required to observe true k^{-1} scaling. Experiments at such Reynolds numbers would be required to validate this prediction.

(*ii*) **2-D spectra of v and w.** In the current study, the 2-D spectra of the streamwise velocity component alone is measured. There is no available data for the 2-D spectra of the spanwise and the wall-normal velocity components at high Reynolds numbers ($\mathcal{O}(10^4)$). Such data can be obtained with the current experimental technique by replacing single-wire probes with miniature ×-probes (Baidya, 2015). The results from the attached eddy model and the DNS of Lee & Moser (2015) suggest that the large-scales in the 2-D spectra of v show a trend towards $\lambda_y \sim \lambda_x$ relationship, and this trend is expected to become conspicuous at higher Reynolds numbers. Hence, the proposed measurement can provide further insights on the self-similarity arguments that are consistent with the attached eddy hypothesis of Townsend (1976).

(*iii*) **2-D spectra in a rough-wall turbulent boundary layer.** An extensive study of rough-wall turbulent boundary layers by Squire *et al.* (2016) showed Townsend's (1976) hypothesis to be valid for a vast range of friction Reynolds numbers when the flow is 'fully-rough'. The 2-D spectra measured under similar roughness conditions could potentially reveal discernible trends of self-similarity for the Reynolds number range considered in the present study.

(*iv*) **2-D linear coherence spectrum at high *Re*.** As discussed in §6.2.2.1, the exact boundaries of the wall-coherent scales in a 2-D spectrum at high Reynolds numbers can only be identified by measuring a 2-D LCS (linear coherence spectrum), as a function of both λ_x and λ_y (similar to figure 6.6). 2-D LCS, as function of wall-heights z and z_R, equals the 2-D cross-spectrum magnitude-squared, normalized by the 2-D spectra of $u(z)$ and $u(z_R)$. The current experimental technique could measure the cross-spectrum and the respective energy spectra individually, towards computing the 2-D LCS at high Reynolds numbers. The measurements would extend the work of Baars *et al.* (2017) and the results could provide information on the three-dimensional structure of wall-coherent motions (in terms of streamwise/wall-normal and spanwise/wall-normal aspect ratios). Additionally, following the work of Baars & Marusic (2018*a*,*b*), the measurement of 2-D LCS with (i) the reference probe at the wall and (ii) the reference probe in the outer layer, would enable a triple decomposition of the 2-D energy spectra. The 2-D spectral sub-components, similar to $\phi_{\mathcal{WL}}$, $\phi^i_{\mathcal{W}}$ and $\phi^c_{\mathcal{L}}$ of Baars & Marusic (2018*a*), could be compared to the 2-D spectra of *Type* A, *Type* C_A and *Type* SS eddies respectively, from the AEM discussed in chapter 6.

(*v*) **Choice of representative eddy.** In the present AEM, the objective was to capture the empirically observed scaling trends in the 2-D energy spectra. Therefore, the emphasis was laid on the geometry of the representative packets and their organization within the boundary layer. No particular emphasis was laid on choosing the appropriate shape of the individual hairpins within the representative packets. However, the current results suggest that a systematic tuning of the shape of the individual hairpins could be necessary to capture the accurate shape of the 2-D spectra of all three components of velocity. This would be a significant improvement to the model. However, to serve this objective, the measurement of 2-D spectra of v and w at high Reynolds numbers ($\mathcal{O}(10^4)$) would be necessary.

(*vi*) **Attached eddy simulation of pipe flows.** Chung *et al.* (2015) suggests that the elusive k_x^{-1} scaling in pipe flows, even at high Reynolds numbers, could be the result of the ‘crowding’ of eddies near the centre of the pipe, due to the geometrical restriction imposed by the curved wall. A simple method to obtain clarity on the ‘crowding’ effect would be to probe the 2-D energy spectra obtained with a population of purely self-similar eddies in a pipe. Therefore, implementing the current AEM in a pipe geometry would be significant. However, the impermeability condition at the curved pipe boundary cannot be achieved by merely supplementing an eddy with its image, as is normally done for flat boundaries. Therefore alternative techniques, such as 3-D panel methods, have to be attempted to achieve impermeability at the curved boundaries.

Appendix A

Steps to filter 2-D spectra

Figure A.1(a) shows the raw experimental 2-D spectrum obtained by taking 2-D Fourier transformation of the 2-D correlation at $Re_\tau \approx 2400$ and $z^+ = 116$. It could be observed that the 2-D spectrum is quite noisy in its raw form which makes it difficult to interpret any trend. Moreover, unfiltered 2-D spectrum also corrupts the associated 1-D streamwise and spanwise spectra that are obtained by integration. As shown in figures A.1(c) and (d) respectively, the 1-D streamwise and spanwise spectra (shown in red) obtained by integrating the unfiltered 2-D spectrum do not agree with the 1-D spectra that are directly computed from the 1-D correlation (shown in blue). The error due to the noise in the 2-D spectrum looks significant and it could be noted that the disagreement is high for $\lambda_x^+ \geq 500$ and $\lambda_y^+ \leq 100$. Therefore, it is important to apply required filters to make the 2-D spectra comprehensive and reliable. To this end, on all the measured low- and high-Reynolds number data, we perform the following steps:

1. **Forcing R_{uu} to be zero at very large Δx**
   Fourier transformation of very low but non-zero correlations at very large Δx, that which are undulations generated due to the measurement noise, are misinterpreted as energy at the corresponding Fourier modes. To avoid this, the 2-D correlation, R_{uu}, at very large streamwise spacings ($\Delta x > \pm 20\delta$) that are much larger than the longest structures observed in turbulent boundary

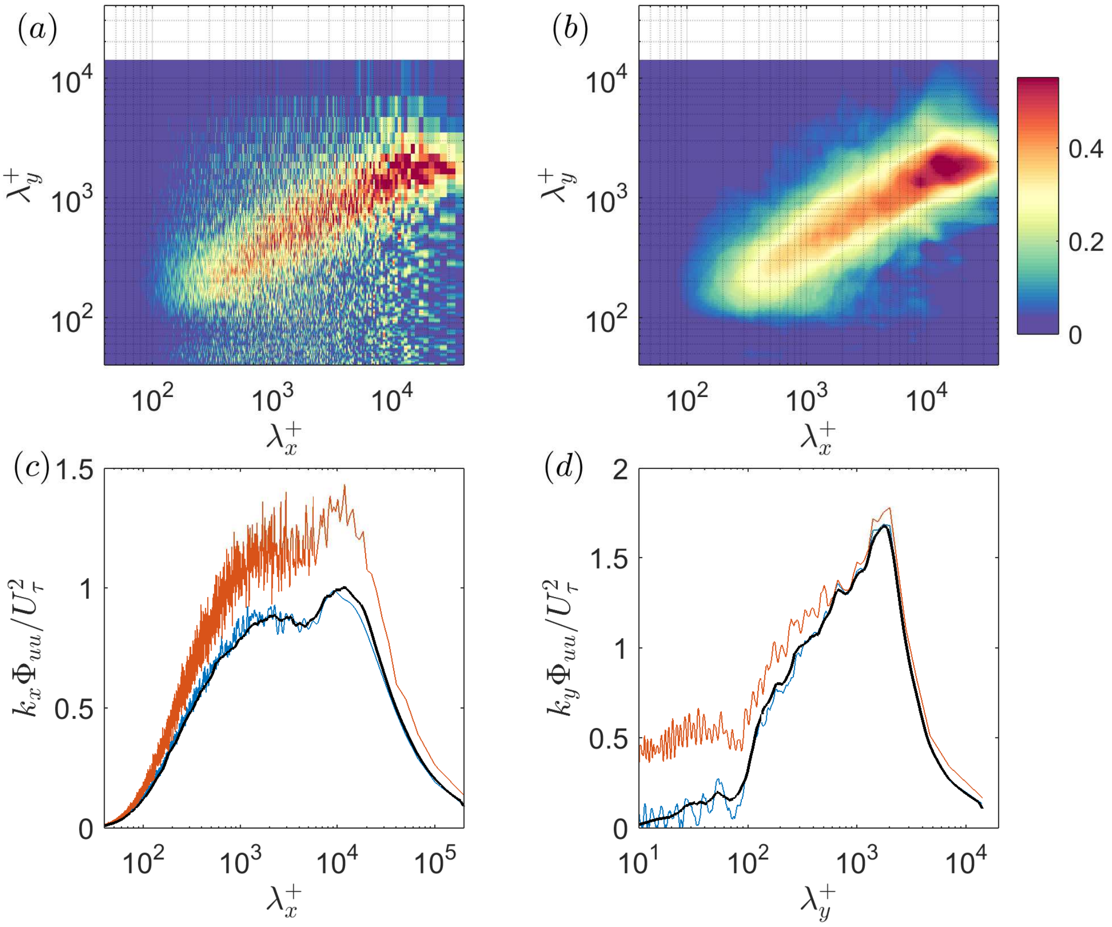

FIGURE A.1: (a) Raw 2-D spectrum, (b) filtered 2-D spectrum obtained following steps 1-4, (c) 1-D streamwise spectra as function of λ_x and (d) 1-D spanwise spectra as function of λ_y. The lines represent: —— 1-D spectra computed directly from 1-D correlation, —— 1-D spectra obtained by integrating the raw 2-D spectrum and —— 1-D spectra obtained by integrating the filtered 2-D spectrum.

layers (Hutchins & Marusic, 2007*a*, Sillero *et al.*, 2014), is forced to be equal to zero.

2. **Correcting R_{uu} at small Δy**

Since we use multiple hot-wires in our measurements, even though all the hot-wires are positioned at the same wall-normal location, the variances ($\overline{u^2}$) of the velocity time series acquired with different hot-wire probes at different times are observed to differ at most by 5%. Due to this difference, we perform a normalization of R_{uu} where the variance of the velocity time series acquired using the free-stream calibrated hot-wire, at the start of the measurement, is taken as the reference. As an example, for the low-*Re* case, the 2-D correlation for each spanwise spacing Δy_i is normalized as:

$$R_{u_1u_2}(\Delta x, \Delta y_i) = R_{u_1u_2}(\Delta x, \Delta y_i) * \frac{\overline{u_1^2}(\Delta y_1)}{\sqrt{\overline{u_1^2}(\Delta y_i) * \overline{u_2^2}(\Delta y_i)}} \tag{A.1}$$

where, i varies from one to the total number of measurement locations in the spanwise direction. Such a normalization would force the peak in R_{uu} to be equal to the reference variance. However, even with this normalization, the values of R_{uu} at smaller Δy and especially larger Δx were observed to be quite noisy, resulting in energetic spikes in the 2-D energy spectrum at small λ_y and large λ_x. Now, in order to smooth the 2-D correlation at such small Δy, we use a reference correlation (function of Δx), instead of a reference variance, as given by,

$$R_{u_1u_2}(\Delta x, \Delta y_i) = R_{u_1u_2}(\Delta x, \Delta y_i) * \frac{R_{u_1u_1}(\Delta x, \Delta y_1)}{\sqrt{R_{u_1u_1}(\Delta x, \Delta y_i) * R_{u_2u_2}(\Delta x, \Delta y_i)}} \tag{A.2}$$

While equation A.1 forces the peak of $R_{uu}(\Delta x = 0, \Delta y = 0)$ to be equal to the reference variance, equation A.2 forces $R_{uu}(\Delta x, \Delta y = 0)$ to be equal to the reference streamwise correlation. Equation A.2 is applied to the 2-D correlation for $\Delta y < 0.1\delta$.

3. **Interpolating to a logarithmically spaced grid**

   The 2-D spectra is interpolated to a 200 × 200 logarithmically spaced grid, which enabled the grid to be finer at smaller streamwise and spanwise wavelengths and coarser towards large wavelengths. It was observed that this interpolation removed the fine disturbances that were present at larger wavelengths and thereby enabling us to interpret the trends better.

4. **Median and Savitzky-Golay filters**

   After interpolating to the logarithmically spaced grid, two filters are applied on to the 2-D spectra. Firstly, a two-dimensional median filter of size $[3, 3]$ is applied. Logarithmically spaced grid enables the median filter to be equally effective at smaller and larger length scales. Secondly, a Savitzky-Golay filter is used to further improve the signal-to-noise ratio. The order and framelength of the filter are chosen to be 3 and 41.

The filtered 2-D spectrum obtained by performing the above steps is shown in figure A.1(b). It could be observed that the energy distribution among streamwise and spanwise length scales is clear in the filtered spectrum and the regions of constant energy are easily distinguishable. The 1-D streamwise and spanwise spectra obtained by integrating the filtered 2-D spectrum is shown in figures A.1(c) and (d) respectively (with black lines), and they agree well with the 1-D spectra computed directly from the 1-D correlations.

Bibliography

Abe, H., Kawamura, H. & Choi, H. 2004 Very large-scale structures and their effects on the wall shear-stress fluctuations in a turbulent channel flow up to $re_\tau = 640$. *J. Fluids Eng.* **126** (5), 835–843.

Acarlar, M. S. & Smith, C. R. 1987*a* A study of hairpin vortices in a laminar boundary layer. part 1. hairpin vortices generated by a hemisphere protuberance. *J. Fluid Mech.* **175**, 1–41.

Acarlar, M. S. & Smith, C. R. 1987*b* A study of hairpin vortices in a laminar boundary layer. part 2. hairpin vortices generated by fluid injection. *J. Fluid Mech.* **175**, 43–83.

Adrian, R. J. 2007 Hairpin vortex organization in wall turbulence. *Phys. Fluids* **19** (4), 041301.

Adrian, R. J., Meinhart, C. D. & Tomkins, C. D. 2000 Vortex organization in the outer region of the turbulent boundary layer. *J. Fluid Mech.* **422**, 1–54.

del Álamo, J. C. & Jiménez, J. 2003 Spectra of the very large anisotropic scales in turbulent channels. *Phys. Fluids* **15** (6), L41–L44.

del Álamo, J. C. & Jiménez, J. 2009 Estimation of turbulent convection velocities and corrections to taylor's approximation. *J. Fluid Mech.* **640**, 5–26.

del Álamo, J. C., Jiménez, J., Zandonade, P. & Moser, R. D. 2004 Scaling of the energy spectra of turbulent channels. *J. Fluid Mech.* **500**, 135–144.

Baars, W. J., Hutchins, N. & Marusic, I. 2016 Spectral stochastic estimation of high-reynolds-number wall-bounded turbulence for a refined inner-outer interaction model. *Phys. Rev. Fluids* **1** (5), 054406.

Baars, W. J., Hutchins, N. & Marusic, I. 2017 Self-similarity of wall-attached turbulence in boundary layers. *J. Fluid Mech.* **823**, R2.

Baars, W. J. & Marusic, I. 2018*a* Data-driven decomposition of the streamwise turbulent kinetic energy in boundary layers. part 1: Energy spectra. *J. Fluid Mech.* .

Baars, W. J. & Marusic, I. 2018*b* Data-driven decomposition of the streamwise turbulent kinetic energy in boundary layers. part 2: Integrated energy and a_1. *J. Fluid Mech.* .

Baidya, Rio 2015 Multi-component velocity measurements in turbulent boundary layers. PhD thesis, The University of Melbourne.

Baidya, R., Philip, J., Hutchins, N., Monty, J. P. & Marusic, I. 2017 Distance-from-the-wall scaling of turbulent motions in wall-bounded flows. *Phys. Fluids* **29** (2), 020712.

Balakumar, B. J. & Adrian, R. J. 2007 Large- and very-large-scale motions in channel and boundary-layer flows. *Phil. Trans. R. Soc. Lond.* **365** (1852), 665–681.

Breuer, K. S 1995 Stochastic calibration of sensors in turbulent flow fields. *Exp. Fluids* **19** (2), 138–141.

Brown, G. L. & Thomas, A. S. W. 1977 Large structure in a turbulent boundary layer. *Phys. Fluids* **20** (10), S243–S252.

Bruun, H. H. 1995 Hot-wire anemometry: principles and signal analysis.

Buschmann, M. H., Indinger, T. & Gad-el Hak, M. 2009 Near-wall behavior of turbulent wall-bounded flows. *Int. J. Heat Fluid Flow* **30** (5), 993–1006.

Calaf, M., Hultmark, M., Oldroyd, H. J., Simeonov, V. & Parlange, M. B. 2013 Coherent structures and the k- 1 spectral behaviour. *Phys. Fluids* **25** (12), 125107.

Campbell, N. 1909 The study of discontinuous phenomena. In *Proc. Camb. Phil. Soc.*, , vol. 15, pp. 117–136.

Chandran, D., Baidya, R., Monty, J. P. & Marusic, I. 2017 Two-dimensional energy spectra in high reynolds number turbulent boundary layers. *J. Fluid Mech.* **826**, R1.

Chauhan, K. A., Monkewitz, P. A. & Nagib, H. M. 2009 Criteria for assessing experiments in zero pressure gradient boundary layers. *Fluid Dyn. Res.* **41**, 021404.

Chung, D., Marusic, I., Monty, J. P., Vallikivi, M. & Smits, A. J. 2015 On the universality of inertial energy in the log layer of turbulent boundary layer and pipe flows. *Exp. Fluids* **56**, 1–10.

Davidson, P. 2015 *Turbulence: an introduction for scientists and engineers*. Oxford University Press.

Davidson, P. A., Nickels, T. B. & Krogstad, P. Å. 2006 The logarithmic structure function law in wall-layer turbulence. *J. Fluid Mech.* **550**, 51–60.

Dennis, D. J. C. & Nickels, T. B. 2008 On the limitations of taylor's hypothesis in constructing long structures in a turbulent boundary layer. *J. Fluid Mech.* **614**, 197–206.

Dennis, D. J. C. & Nickels, T. B. 2011 Experimental measurement of large-scale three-dimensional structures in a turbulent boundary layer. part 1. vortex packets. *J. Fluid Mech.* **673**, 180–217.

Fife, P., Wei, T., Klewicki, J. & McMurtry, P. 2005 Stress gradient balance layers and scale hierarchies in wall-bounded turbulent flows. *J. Fluid Mech.* **532**, 165–189.

Ganapathisubramani, B., Hutchins, N., Hambleton, W. T., Longmire, E. K. & Marusic, I. 2005 Investigation of large-scale coherence in a turbulent boundary layer using two-point correlations. *J. Fluid Mech.* **524**, 57–80.

Ganapathisubramani, B., Longmire, E. K. & Marusic, I. 2003 Characteristics of vortex packets in turbulent boundary layers. *J. Fluid Mech.* **478**, 35–46.

Guala, M., Hommema, S. E. & Adrian, R. J. 2006 Large-scale and very-large-scale motions in turbulent pipe flow. *J. Fluid Mech.* **554**, 521–542.

Guala, M., Metzger, M. & McKeon, B. J. 2011 Interactions within the turbulent boundary layer at high Reynolds number. *J. Fluid Mech.* **666**, 573–604.

Head, M. R. & Bandyopadhyay, P. 1981 New aspects of turbulent boundary-layer structure. *J. Fluid Mech.* **107**, 297–338.

Högström, U., Hunt, J. C. R. & Smedman, A.-S 2002 Theory and measurements for turbulence spectra and variances in the atmospheric neutral surface layer. *Boundary-layer Meteorol.* **103** (1), 101–124.

Hoyas, S. & Jiménez, J. 2006 Scaling of the velocity fluctuations in turbulent channels up to $Re_\tau = 2003$. *Phys. Fluids* **18** (1), 011702.

Hultmark, M., Vallikivi, M., Bailey, S. C. C. & Smits, A. J. 2012 Turbulent pipe flow at extreme reynolds numbers. *Phys. Rev. Lett.* **108** (9), 094501.

Hunt, J. C. R. & Morrison, J. F. 2000 Eddy structure in turbulent boundary layers. *Eur. J. Mech. B-Fluid* **19**, 673–694.

Hutchins, N., Hambleton, W. T. & Marusic, I. 2005 Inclined cross-stream stereo particle image velocimetry measurements in turbulent boundary layers. *J. Fluid Mech.* **541**, 21–54.

Hutchins, N. & Marusic, I. 2007*a* Evidence of very long meandering features in the logarithmic region of turbulent boundary layers. *J. Fluid Mech.* **579**, 1–28.

Hutchins, N. & Marusic, I. 2007*b* Large-scale influences in near-wall turbulence. *Phil. Trans. R. Soc. Lond.* **365** (1852), 647–664.

Hutchins, N., Nickels, T. B., Marusic, I. & Chong, M. S. 2009 Hot-wire spatial resolution issues in wall-bounded turbulence. *J. Fluid Mech.* **635**, 103–136.

Jiménez, J. 2012 Cascades in wall-bounded turbulence. *Annu. Rev. Fluid Mech.* **44**, 27–45.

Jiménez, Javier 2013 Near-wall turbulence. *Phys. Fluids* **25** (10), 101302.

Jiménez, Javier 2018 Coherent structures in wall-bounded turbulence. *J. Fluid Mech.* **842**.

Jiménez, J. & Hoyas, S. 2008 Turbulent fluctuations above the buffer layer of wall-bounded flows. *J. Fluid Mech.* **611**, 215–236.

Jodai, Y. & Elsinga, G. E. 2016 Experimental observation of hairpin auto-generation events in a turbulent boundary layer. *J. Fluid Mech.* **795**, 611–633.

von Kármán, T 1930 Mechanische ähnlichkeit und turbulenz. *Nachr. Ges. Wiss Gottingen* **611**, 58–76.

Katul, G. & Chu, C.-R 1998 A theoretical and experimental investigation of energy-containing scales in the dynamic sublayer of boundary-layer flows. *Boundary-layer Meteorol.* **86** (2), 279–312.

Kevin, K., Monty, J. & Hutchins, N. 2019 The meandering behaviour of large-scale structures in turbulent boundary layers. *J. Fluid Mech.* **865**.

Kim, K. C. & Adrian, R. J. 1999 Very large-scale motion in the outer layer. *Phys. Fluids* **11** (2), 417–422.

KLEWICKI, J., FIFE, P. & WEI, T. 2009 On the logarithmic mean profile. *J. Fluid Mech.* **638**, 73–93.

KLEWICKI, J. C. 2010 Reynolds number dependence, scaling, and dynamics of turbulent boundary layers. *J. Fluids. Engng.* **132** (9), 094001.

KLINE, S. J., REYNOLDS, W. C., SCHRAUB, F. A. & RUNSTADLER, P. W. 1967 The structure of turbulent boundary layers. *J. Fluid Mech.* **30** (04), 741–773.

KOLMOGOROV, ANDREY NIKOLAEVICH 1941 The local structure of turbulence in incompressible viscous fluid for very large reynolds numbers. In *Dokl. Akad. Nauk SSSR*, , vol. 30, pp. 299–303.

KRAHEBERGER, S., HOYAS, S. & OBERLACK, M. 2018 Dns of a turbulent couette flow at constant wall transpiration up to $Re_\tau = 1000$. *J. Fluid Mech.* **835**, 421–443.

KULANDAIVELU, V. 2012 Evolution of zero pressure gradient turbulent boundary layers from different initial conditions. PhD thesis, The University of Melbourne.

KUNKEL, G. J. & MARUSIC, I. 2006 Study of the near-wall-turbulent region of the high-Reynolds-number boundary layer using an atmospheric flow. *J. Fluid Mech.* **548**, 375–402.

LEE, J. H. 2017 Evolution of canonical turbulent boundary layers. PhD thesis, The University of Melbourne.

LEE, M. & MOSER, R. D. 2015 Direct numerical simulation of turbulent channel flow up to $Re_\tau = 5200$. *J. Fluid Mech.* **774**, 395–415.

LIU, H., WANG, G. & ZHENG, X. 2019 Amplitude modulation between multi-scale turbulent motions in high-Reynolds-number atmospheric surface layers. *J. Fluid Mech.* **861**, 585–607.

MARUSIC, I. 2001 On the role of large-scale structures in wall turbulence. *Phys. Fluids* **13** (3), 735–743.

Marusic, I., Chauhan, K. A., Kulandaivelu, V. & Hutchins, N. 2015 Evolution of zero-pressure-gradient boundary layers from different tripping conditions. *J. Fluid Mech.* **783**, 379–411.

Marusic, I., Mathis, R. & Hutchins, N. 2010*a* High reynolds number effects in wall turbulence. *Int. J. Heat Fluid Flow* **31** (3), 418–428.

Marusic, I., Mathis, R. & Hutchins, N. 2010*b* Predictive model for wall-bounded turbulent flow. *Science* **329** (5988), 193–196.

Marusic, I., McKeon, B. J., Monkewitz, P. A., Nagib, H. M., Smits, A. J. & Sreenivasan, K. R. 2010*c* Wall-bounded turbulent flows at high reynolds numbers: recent advances and key issues. *Phys. Fluids* **22** (6), 065103.

Marusic, I. & Monty, J. P. 2019 Attached eddy model of wall turbulence. *Annu. Rev. Fluid Mech.* (0).

Marusic, I., Monty, J. P., Hultmark, M. & Smits, A. J. 2013 On the logarithmic region in wall turbulence. *J. Fluid Mech.* **716**, R3.

Marusic, I & Perry, A. E 1995 A wall-wake model for the turbulence structure of boundary layers. part 2. further experimental support. *J. Fluid Mech.* **298**, 389–407.

Mathis, R., Hutchins, N. & Marusic, I. 2009 Large-scale amplitude modulation of the small-scale structures in turbulent boundary layers. *J. Fluid Mech.* **628**, 311–337.

Millikan, Clark B 1938 A critical discussion of turbulent flows in channels and circular tubes. In *Proc. 5th Int. Cong. Appl. Mech*, pp. 386–392. Wiley/Chapman and Hall, New York-London.

Monty, J. P. & Chong, M. S. 2009 Turbulent channel flow: comparison of streamwise velocity data from experiments and direct numerical simulation. *J. Fluid Mech.* **633**, 461–474.

Monty, J. P., Stewart, J. A., Williams, R. C. & Chong, M. S. 2007 Large-scale features in turbulent pipe and channel flows. *J. Fluid Mech.* **589**, 147–156.

Morrison, W. R. B. & Kronauer, R. E. 1969 Structural similarity for fully developed turbulence in smooth tubes. *J. Fluid Mech.* **39**, 117–141.

Nickels, T. B., Marusic, I., Hafez, S. & Chong, M. S. 2005 Evidence of the k_1^{-1} law in a high-Reynolds-number turbulent boundary layer. *Phys. Rev. Lett.* **95**, 074501.

Nickels, T. B, Marusic, I., Hafez, S., Hutchins, N. & Chong, M. S. 2007 Some predictions of the attached eddy model for a high reynolds number boundary layer. *Philos. Trans. R. Soc. Lond., A* **365** (1852), 807–822.

Nugroho, Bagus 2015 Highly ordered surface roughness effects on turbulent boundary layers. PhD thesis, The University of Melbourne.

Oberlack, M. 2001 A unified approach for symmetries in plane parallel turbulent shear flows. *J. Fluid Mech.* **427**, 299–328.

Örlü, R., Fransson, J. H. M. & Alfredsson, P. H. 2010 On near wall measurements of wall bounded flows—the necessity of an accurate determination of the wall position. *Prog. Aerosp. Sci.* **46** (8), 353–387.

Perry, AE & Abell, CJ 1977 Asymptotic similarity of turbulence structures in smooth-and rough-walled pipes. *J. Fluid Mech.* **79** (4), 785–799.

Perry, A. E. 1982 Hot-wire anemometry. *Tech. Rep.*.

Perry, A. E. & Chong, M. S. 1982 On the mechanism of wall turbulence. *J. Fluid Mech.* **119**, 173–217.

Perry, A. E., Henbest, S. & Chong, M. S. 1986 A theoretical and experimental study of wall turbulence. *J. Fluid Mech.* **165**, 163–199.

Perry, A. E & Marusic, I 1995 A wall-wake model for the turbulence structure of boundary layers. part 1. extension of the attached eddy hypothesis. *J. Fluid Mech.* **298**, 361–388.

Pirozzoli, Sergio & Bernardini, Matteo 2013 Probing high-Reynolds-number effects in numerical boundary layers. *Phys. Fluids* **25**, 021704.

Pope, S. B. 2000 *Turbulent flows*. Cambridge university press.

Prandtl, L. 1904 Uber flussigkeits bewegung bei sehr kleiner reibung. *Verhaldlg III Int. Math. Kong* pp. 484–491.

Prandtl, L. 1925 Bericht uber untersuchungen zur ausgebildeten turbulenz. *Zs. angew. Math. Mech.* **5**, 136–139.

Renard, N. & Deck, S. 2015 On the scale-dependent turbulent convection velocity in a spatially developing flat plate turbulent boundary layer at Reynolds number $Re_\theta = 13000$. *J. Fluid Mech.* **775**, 105–148.

Robinson, S. K. 1991 Coherent motions in the turbulent boundary layer. *Annu. Rev. Fluid Mech.* **23** (1), 601–639.

Rosenberg, B. J., Hultmark, M., Vallikivi, M., Bailey, S. C. C. & Smits, A. J. 2013 Turbulence spectra in smooth-and rough-wall pipe flow at extreme Reynolds numbers. *J. Fluid Mech.* **731**, 46–63.

Saddoughi, S. G. & Veeravalli, S. V. 1994 Local isotropy in turbulent boundary layers at high reynolds number. *J. Fluid Mech.* **268**, 333–372.

Samie, M. 2017 Sub-miniature hot-wire anemometry for high reynolds number turbulent flows. PhD thesis, The University of Melbourne.

Samie, M., Marusic, I., Hutchins, N., Fu, M. K., Fan, Y., Hultmark, M. & Smits, A. J. 2018 Fully resolved measurements of turbulent boundary layer flows up to $Re_\tau = 20000$. *J. Fluid Mech.* **851**, 391–415.

Schlatter, P., Li, Q., Örlü, R., Hussain, F.azle & Henningson, D. S. 2014 On the near-wall vortical structures at moderate Reynolds numbers. *Eur. J. Mech. B-Fluid* **48**, 75–93.

Sillero, Juan A, Jiménez, Javier & Moser, Robert D 2013 One-point statistics for turbulent wall-bounded flows at Reynolds numbers up to $\delta+ \approx$ 2000. *Phys. Fluids* **25** (10), 105102.

Sillero, J. A., Jiménez, J. & Moser, R. D. 2014 Two-point statistics for turbulent boundary layers and channels at Reynolds numbers up to $\delta+ \approx$ 2000. *Phys. Fluids* **26**, 105109.

de Silva, C. M., Squire, D. T., Hutchins, N. & Marusic, I. 2015 Towards capturing large scale coherent structures in boundary layers using particle image velocimetry. In *Proceedings of the 7th Australian Conference on Laser Diagnostics in Fluid Mechanics and Combustion*. Melbourne, Australia.

de Silva, C. M., Woodcock, J. D., Hutchins, N. & Marusic, I. 2016 Influence of spatial exclusion on the statistical behavior of attached eddies. *Phys. Rev. Fluid* **1** (2), 022401.

Smits, A. J., McKeon, B. J. & Marusic, I. 2011 High-Reynolds number wall turbulence. *Annu. Rev. Fluid Mech.* **43**, 353–375.

Squire, D. T., Morrill-Winter, C., Hutchins, N., Schultz, M. P., Klewicki, J. C. & Marusic, I. 2016 Comparison of turbulent boundary layers over smooth and rough surfaces up to high reynolds numbers. *J. Fluid Mech.* **795**, 210–240.

Sreenivasan, K. R. 1995 On the universality of the kolmogorov constant. *Phys. Fluids* **7** (11), 2778–2784.

Talluru, K. M., Baidya, R., Hutchins, N. & Marusic, I. 2014*a* Amplitude modulation of all three velocity components in turbulent boundary layers. *J. Fluid Mech.* **746**.

Talluru, K. M., Kulandaivelu, V., Hutchins, N. & Marusic, I. 2014*b* A calibration technique to correct sensor drift issues in hot-wire anemometry. *Meas. Sci. Technol.* **25** (10), 105304.

Tennekes, H. & Lumley, J. L. 1972 *A first course in turbulence.* MIT press.

Theodorsen, T. 1952 Mechanisms of turbulence. In *Proceedings of the* 2^{nd} *Midwestern Conference on Fluid Mechanics.*

Tinney, C. E., Coiffet, F., Delville, J., Hall, A. M., Jordan, P. & Glauser, M. N. 2006 On spectral linear stochastic estimation. *Exp. Fluids* **41** (5), 763–775.

Tomkins, C. D. & Adrian, R. J. 2005 Energetic spanwise modes in the logarithmic layer of a turbulent boundary layer. *J. Fluid Mech.* **545**, 141–162.

Townsend, A. A. 1961 Equilibrium layers and wall turbulence. *J. Fluid Mech.* **11** (1), 97–120.

Townsend, A. A. 1976 *The structure of turbulent shear flow*, 2nd edn. Cambridge university press.

Vallikivi, M., Ganapathisubramani, B. & Smits, A. J. 2015*a* Spectral scaling in boundary layers and pipes at very high reynolds numbers. *J. Fluid Mech.* **771**, 303–326.

Vallikivi, M., Hultmark, M. & Smits, A. J. 2015*b* Turbulent boundary layer statistics at very high reynolds number. *J. Fluid Mech.* **779**, 371–389.

Wang, G. & Zheng, X. 2016 Very large scale motions in the atmospheric surface layer: a field investigation. *J. Fluid Mech.* **802**, 464–489.

Woodcock, J. D. & Marusic, I. 2015 The statistical behaviour of attached eddies. *Phys. Fluids* **27** (1), 015104.

Wu, X. & Moin, P. 2009 Direct numerical simulation of turbulence in a nominally zero-pressure-gradient flat-plate boundary layer. *J. Fluid Mech.* **630**, 5–41.

Yang, X. I. A., Baidya, R., Johnson, P., Marusic, I. & Meneveau, C. 2017 Structure function tensor scaling in the logarithmic region derived from the attached eddy model of wall-bounded turbulent flows. *Phys. Rev. Fluids* **2** (6), 064602.

Zagarola, M. V. & Smits, A. J. 1998 Mean-flow scaling of turbulent pipe flow. *J. Fluid Mech.* **373**, 33–79.

Zhou, J., Adrian, R. J. & Balachandar, S 1996 Autogeneration of near-wall vortical structures in channel flow. *Phys. Fluids* **8** (1), 288–290.

Zhou, J., Adrian, R. J., Balachandar, S. & Kendall, T. M. 1999 Mechanisms for generating coherent packets of hairpin vortices in channel flow. *J. Fluid Mech.* **387**, 353–396.

Author/s:
Padinjare Muttikkal, Dileep Chandran

Title:
Characteristics of energetic motions in turbulent boundary layers

Date:
2019

Persistent Link:
http://hdl.handle.net/11343/223010

File Description:
Characteristics of energetic motions in turbulent boundary layers